Exploring the therapeutic potential of plasmonic hybrid multiwalled carbon nanotubes in cancer treatment and beyond

Fatma Oudjedi

Department of Electrical & Computer Engineering
McGill University
Montréal, Canada

February 2024

A thesis submitted to the McGill University
in partial fulfillment of the requirements for the degree of
Doctor of Philosophy

© 2024 Fatma Oudjedi

"Indeed, with hardship comes ease." (Quran 94:6)

To my parents,

In every line written, in every milestone achieved, and in every lesson learned, your influence is woven deeply into the fabric of this work. It is with profound gratitude and deepest love that I dedicate this thesis to you, my pillars of strength, the epitome of selflessness and steadfastness.

Abstract

Prostate cancer is a significant public health concern in the United States and globally, causing a substantial number of male deaths each year, ranking second in terms of cancer−related mortality. Focal therapy, an emerging approach in prostate cancer treatment, aims to ablate malignant tissues while precisely preserving the neighboring healthy tissues. Photothermal therapy holds promise as a focal treatment option for prostate cancer, overcoming the limitations of conventional therapies through nanoparticle−based approaches. Despite recent advancements in the development of diverse photothermal agents, further progress is urgently required in photothermal therapy. These photothermal transducers should possess the ability to absorb near−infrared (NIR) light and convert it into heat, enabling localized hyperthermia and the subsequent destruction of cancer cells. It is crucial for these transducers to absorb light within the NIR region, which corresponds to the biological window, and to enhance heat generation, specifically at the cellular level. Multiwalled carbon nanotubes (MWCNTs) have attracted significant attention in photothermal therapy owing to their exceptional optical and surface properties. However, their limited absorption within the biologically relevant 800 nm window requires exploration of methods to enhance their absorption and improve the light−to−heat conversion. Here, we propose covalently attaching plasmonic gold nanorods (GNRs) to the surface of MWCNTs, which exhibit localized surface plasmon resonance within the therapeutic window. This thesis delves into exploring the potential therapeutic applications of MWCNTs−GNRs within the first near-infrared window ($750 - 950$ nm).

Our investigation encompasses the optical and thermal characterization of our plasmonic hybrid nanostructure, analyzing their light−to−conversion efficiency, temperature profiles, and potential use as temperature probes using Raman spectroscopy. Through numerical and

experimental analyses of the optical and thermal properties of the decorated carbon nanotubes, we present our findings from near-infrared photothermal measurements and quantitative analysis of the hybrid carbon nanostructure using a laser wavelength of 808 nm. Furthermore, we evaluated the *in vitro* performance of MWCNTs−GNRs as photothermal agents, which resulted in the efficient thermal ablation of cancer cells, surpassing the capabilities of current plasmonic nanostructures. Using prostate cancer cell lines, we demonstrated the effective use of MWCNTs−GNRs as nanoprobe thermometers for photothermal therapy by measuring its anti−Stokes and Stokes signals at different laser powers. Our results revealed that gold−decorated MWCNTs effectively heated cancer cells and enabled non-invasive temperature monitoring. The proposed hybrid nanoparticle addresses the current constraints of *in vitro* photothermal therapy and serves as a stepping stone for developing a new generation of photothermal therapy agents.

Résumé

Le cancer de la prostate est un problème de santé publique important aux États-Unis. Il présente un taux d'incidence élevé chez les hommes et occupe la deuxième place en termes de mortalité globale associée au cancer. La thérapie focale émergente vise à ablater précisément les tissus malins tout en préservant les tissus sains avoisinants. La thérapie photothermique focalisée est prometteuse contre le cancer de la prostate, en utilisant des nanoparticules pour surpasser les limites des thérapies conventionnelles. Malgré les récentes avancées dans le développement de divers agents photothermiques, il est urgent de progresser dans le domaine de la thérapie photothermique. Ces transducteurs photothermiques absorbent la lumière infrarouge proche (PIR) et la convertissent en chaleur, ce qui permet une hyperthermie localisée et la destruction des cellules cancéreuses. Il est crucial que ces transducteurs absorbent la lumière dans la fenêtre biologique et améliorent la production de chaleur, en particulier au niveau cellulaire, pour qu'ils soient efficaces. Les nanotubes de carbone multiparois (MWCNTs) ont suscité une grande attention dans le domaine de la thérapie photothermique en raison de leurs propriétés optiques et de surface exceptionnelles. Cependant, leur absorption limitée dans la fenêtre biologiquement pertinente de 800 nm nécessite l'exploration de méthodes pour augmenter leur absorption et améliorer la conversion de la lumière en chaleur. Ici, nous proposons de lier de manière covalente des nanobâtonnets d'or plasmoniques (GNRs) à la surface des MWCNTs, qui présentent une résonance plasmonique de surface localisée dans la fenêtre thérapeutique.

Cette thèse explore les applications thérapeutiques potentielles de MWCNTs−GNRs dans la première fenêtre du PIR ($750 - 950$ nm). Notre recherce comprend la caractérisation optique et thermique de nos nanostructures hybrides plasmoniques, en analysant leur efficacité

de conversion de la lumière, leurs profils de température et leur utilisation potentielle en tant que sondes de température à l'aide de la spectroscopie Raman. Grâce à des analyses numériques et expérimentales des propriétés optiques et thermiques de MWCNTs−GNRs, nous présentons nos résultats de mesures photothermiques dans le PIR et d'analyse quantitative de la nanostructure hybride de carbone à l'aide d'un laser d'une longueur d'onde de 808 nm. En outre, nous avons évalué la performance *in vitro* des MWCNTs−GNRs en tant qu'agents photothermiques, ce qui a entraîné une ablation thermique efficace des cellules cancéreuses, surpassant les capacités des nanostructures plasmoniques actuelles. Nous avons utilisé des cellules cancéreuses de la prostate pour démontrer l'efficacité des MWCNTs−GNRs comme thermomètres nanosondes pour la thérapie photothermique en mesurant des signaux anti−Stokes et Stokes à différentes puissances de laser. Nos résultats ont révélé que les MWCNTs−GNRs chauffaient efficacement les cellules cancéreuses et permettaient un contrôle non invasif de la température. La nanoparticule hybride permet de répondre aux contraintes actuelles de la thérapie photothermique *in vitro* et de développer une nouvelle génération d'agents thérapeutiques.

Acknowledgements

Al-Hakeem (The Wise) has led me to the closure of certain doors while opening new opportunities, profoundly shaping my academic journey in unexpected ways.

First and foremost, I would like to express my sincere gratitude to Prof. Andrew G. Kirk for giving me the unique opportunity to join his lab and introducing me to multidisciplinary research, where I could collaborate with experts from various fields. His invaluable guidance and unwavering support throughout this research endeavor have been instrumental to my academic achievements. I am profoundly grateful for the privilege of working under his supervision, and I deeply appreciate the wealth of knowledge, dedication, and experiences he has imparted to me.

I am thankful to Dr. Mark Trifiro and Prof. Sebastian Wachsmann-Hogiu, members of my Ph.D. committee, for their support and contributions to my research journey. Their provision of access to their respective laboratory facilities has been instrumental in facilitating my experiments and analyses. Furthermore, I am thankful for the generous amount of time they have dedicated to engaging in insightful discussions and offering constructive feedback at various stages of my research endeavor.

I am also thankful to Dr. Miltiadis Paliouras and Mr. Seung Soo Lee for their contributions to this research endeavor. Mr. Lee's expertise in material synthesis and experimental work with cancer cell lines enriched the project's outcomes. Dr. Paliouras provided insightful discussions, which enhanced the quality of the research. As someone not specializing in cellular biology, their support allowed me to navigate the complexities of working with prostate cancer cells.

I would like to thank Prof. Adam Hendricks from the Department of Bioengineering at McGill University for his generous provision of access to cell culture facilities. The availability

of these facilities has played a vital role in conducting Raman experiments.

I would like to thank Professor Juan Hernández-Cordero for engaging in insightful discussions regarding our research on short-pulse simulation. Additionally, I am thankful for his introduction to Dr. Juan Rodrigo Velez, with whom we have an ongoing collaboration.

I thank Dr. David Liu (FEMR, McGill), Mr. Petr Fiurasek (MCCF, McGill), Mr. Mike Giovinazzo (Lady Davis Institute, JGH), and Mr. Gwénaël Chamoulaud (NanoQAM, UQAM) for their technical assistance and training in using equipment throughout my research work. Special thanks to Dr. JuanJuan Liu for her training in Raman spectroscopy. I would like to thank my friends and colleagues for their kind support during my PhD journey.

Lastly, I express my deepest appreciation to my parents and siblings for their unwavering love, encouragement, and endless support, which has fueled my determination and sustained me through the challenges and achievements of this academic endeavor.

Abbreviations

CDD charged coupled device

CNTs carbon nanotubes

CW continuous wave

FBS fetal bovine serum

GNCs gold nanocages

GNPs gold nanoparticles

GNRs gold nanorods

GNSs gold nanoshells

LITT laser interstitial thermal therapy

LSPR localized surface plasmon resonance

MRI magnetic resonance imaging

MTT methyl thiazolyl tetrazolium

MWCNTs multiwalled carbon nanotubes

MWCNTs−GNRs gold nanorods−decorated multiwalled carbon nanotubes

NIR near−infrared

OD optical density

PA photoacoustic

PBS phosphate−buffered saline

PC3 prostate cancer cell lines

PDT photodynamic therapy

PPTT plasmonic photothermal therapy

PSA prostate−specific antigen

PTT photothermal therapy

SERS surface−enhanced Raman scattering

SPR surface plasmon resonance

SWCNTs single−walled carbon nanotubes

TEM transmission electron microscopy

TGA thermal gravimetric analysis

Contents

List of Figures

List of Tables

Chapter 1

Introduction

1.1 Current Treatment for Prostate Cancer

During a man's lifetime, approximately one in every eight men is diagnosed with prostate cancer [7]. Prostate cancer is a major public health concern in the United States, leading to numerous deaths annually among men. It is one of the most common cancers in men and the second leading cause of cancer−related death worldwide. According to the American Cancer Society, approximately 288,300 new cases of prostate cancer will be diagnosed by 2023, and 34,700 men will die [7]. The use of prostate−specific antigen (PSA) for the screening of prostate cancer is controversial because it has led to increased diagnosis and treatment of low− and intermediate−risk prostate cancer [8, 9]. Patients with these conditions are typically considered for active surveillance or whole−gland therapies such as prostatectomy (radical surgery) or radiation therapy. Prostate cancer treatment has a significant impact on both the economy and society. Therefore, it is essential to consider the available treatments, their costs, and the cost−effectiveness of different clinical strategies for treating localized prostate cancer at different stages of severity [10]. Despite the progress in cancer treatment, more effective and less invasive treatment options for prostate cancer are still needed. Focal therapy, which involves the targeted destruction of cancerous tissue in the prostate while preserving healthy surrounding tissue, is an emerging option that reduces side effects such as urinary dysfunction, erectile dysfunction, and morbidity associated with whole−gland therapies [8].

Due to the multifocal nature of prostate cancer, focal therapy is an alternative treatment for patients with malignant lesions [8]. In recent decades, several focal treatment options have been developed for low− and intermediate−risk prostate cancer, including irreversible electroporation [11] radiofrequency ablation [12], focal brachytherapy [13], cryotherapy [14], photoactivated nanoparticle therapy [15, 16], and highly focused ultrasound therapy [17]. In recent years, the development of nanoparticles for cancer therapy has emerged as a promising approach for overcoming the limitations of conventional therapies. Near−infrared plasmonic photothermal therapy (PPTT) [18–20] has received considerable attention because of its ability to selectively target cancer cells using near−infrared (NIR) light and generate heat to destroy them. This therapy is based on the unique properties of plasmonic nanoparticles, which can absorb NIR light and convert it into heat, causing localized hyperthermia and inducing cancer cell death.

1.2 Limitation of Focal Ablation Therapy

PPTT is a promising method for treating cancers, including prostate cancer, owing to its high selectivity and minimally invasive nature. Compared to other focal ablation treatment modalities, PPTT has the advantage of generating accurate, predictable, and homogeneous tumor ablation while minimizing collateral damage to the surrounding tissues. Precision control of photothermal therapy (PTT) is only possible with the use of light−activated nanoparticles, which enables spatiotemporal control of treatment and achievement of therapeutic effects. The effectiveness of NIR plasmonic photothermal therapy has been demonstrated in various preclinical studies, showing selective cancer cell killing and tumor regression. In 2019, a research team conducted a pilot clinical trial utilizing gold−silica nanoshells for unifocal nanoparticle−mediated photothermal therapy in patients with prostate cancer [21]. The study identified limitations in monitoring the temperature within the tumor and surrounding tissues using magnetic resonance imaging (MRI)−guided laser interstitial thermal therapy (LITT). Gold−silica nanoshell−directed ablation addresses this limitation as it selectively targets only the tissues, ensuring that laser ablation is successful while minimizing the risk of overheating. These preliminary clinical results provide an impetus for further investigation of novel nanostructures and strategies for precise, controlled, and uniform energy delivery, as

well as for temperature measurement and distribution in tumors. Considering the unique characteristics of prostate cancer, including the location of the prostate gland and its associated risk factors, numerical and experimental investigations are essential to facilitate the development of novel nanomaterials suitable for hyperthermia plasmonic photothermal therapy.

1.3 Research Objectives

Considering this context of photothermal therapy, the objectives of this thesis are i) to investigate the potential of multiwalled carbon nanotubes (MWCNTs) decorated with plasmonic gold nanorods (GNRs) to achieve high local absorption and heat conversion in the near−infrared biological window; ii) to evaluate their efficacy in achieving ablation efficiency and heat confinement in near−infrared photothermal therapy; and iii) to assess the efficacy of Raman thermometry in determining the local temperature during photothermal therapy. This research encompasses the design and synthesis of a novel therapeutic plasmonic nanomaterial, experimental and numerical evaluation of the efficacy of the photothermal agent using continuous wave, and its potential theragnostic applications using Raman spectroscopy. An experimental approach employing prostate cancer cell lines (PC3) was used to investigate the *in vitro* applications of plasmonic nanostructures. MWCNTs decorated with plasmonic nanoparticles offer significant advantages over existing PTT agents, given their enhanced light−to−heat conversion efficiency in the NIR window, resulting in efficient and localized heat generation at the cellular level. This thesis focuses on the potential benefits of gold nanorods−decorated multiwalled carbon nanotubes (MWCNTs−GNRs) as i) NIR photothermal transducers and ii) nanoprobe thermometers in photothermal cancer therapy. In summary, this thesis delves into pivotal questions to develop a more efficient and effective approach to PTT, which has the potential to improve cancer treatment outcomes.

1. Can the NIR absorption of MWCNTs be enhanced through hybridization with plasmonic nanostructures, and if so, which plasmonic structure is the most suitable?

2. What is the most suitable numerical technique for properly modeling the electromagnetic response of MWCNTs decorated with plasmonic gold nanorods?

3. What is the most appropriate chemical process for synthesizing novel photothermal transducers that involve decorating MWCNTs with plasmonic gold nanorods?

4. Which high-resolution techniques can effectively assess the optical properties and visualize the morphology and size of MWCNTs−GNRs?

5. Which non-invasive spectroscopic techniques are viable for monitoring the temperature at the cellular level? Can MWCNTs−GNRs serve as *in situ* nanoprobes for temperature cancer cells using anti-Stokes Raman thermometry?

6. Which *in vitro* assays can be used to comprehensively evaluate the cytotoxicity of the novel hybrid photothermal transducers (i.e., MWCNTs−GNRs) for NIR photothermal therapy?

Based on these research questions and according to the proposed objectives, the following *in vitro* effects were accomplished, encompassing both computational and experimental aspects:

1. A numerical model was developed to calculate the optical and thermal properties of decorated MWCNTs and used to determine their feasibility as photothermal agents for *in vitro* and *in vivo* clinical applications. Finite element method software was utilized to study the thermal and optical spectral distributions of bare and plasmonic-decorated carbon nanotubes. This computational model has enabled a better understanding of plasmonic photothermal therapy using plasmonic hybrid carbon nanotubes as mediated heating agents and beyond.

2. Efficient thermal ablation was achieved using the novel hybrid nanostructures as plasmonic photothermal transducers. These novel nanostructures enabled the implementation of plasmonic nanoparticles exhibiting localized surface plasmons, which increased the absorbance coefficient and photothermal conversion in the near−infrared spectrum, as well as maximized tumor cell damage.

3. The combination of Raman spectroscopy and laser delivery has proven useful for direct temperature measurements at the cellular level at various power levels.

1.4 Significance of the Work

Nanoparticles in cancer therapy represent a rapidly growing field of research that holds promise for applications beyond cancer treatment, including imaging, drug delivery, and diagnostics. The development of more effective and safe therapeutic nanoparticles can extend their utility across various fields. Overcoming the limitations of conventional cancer therapies, such as chemotherapy and radiation therapy, is important for reducing damage to healthy tissues and reducing severe side effects. This could lead to better patient outcomes and quality of life.

To address these challenges, a novel NIR photothermal transducer that involves multi-walled carbon nanotubes decorated with plasmonic gold nanorods is proposed and evaluated, both numerically and experimentally. This innovative hybrid approach to designing hybrid MWCNTs aims to open the doors for theragnosis based on imaging and confined ablation of cancer cells, as well as offering a minimally invasive therapeutic strategy with *in situ* temperature measurement using decorated carbon nanotubes.

This work has significant implications for cancer therapy and biomedical research by introducing a novel approach to address the limitations of current photothermal therapy. The proposed hybrid nanoparticle addresses the current limitations of PTT and lays the groundwork for the development of a new generation of PTT agents that combine nanotechnology and laser technology with Raman spectroscopy to improve cancer treatment outcomes. The interdisciplinary nature of this study underscores the importance of collaboration between different fields to develop innovative cancer therapies. In summary, NIR plasmonic photothermal cancer therapy has the potential to transform cancer treatment by providing more targeted and minimally invasive therapies with fewer side effects. Its economic implications are also notable, as it has the potential to reduce the cost of cancer treatment.

1.5 Scope and Limitation of the Research

The scope of research on NIR plasmonic photothermal cancer therapy encompasses the development of nanoparticles with enhanced NIR light absorption. This thesis focuses on the photophysical properties of near−infrared plasmonic hybrid nanostructures under various

experimental conditions, evaluated using an *in vitro* approach to assess the cytotoxicity and potential cell viability under laser irradiation and plasmonic hybrid nanoparticles. Although non−targeted cells have been employed, functionalization of these nanoparticles with targeting moieties such as antibodies, peptides, or small molecules can improve their specificity for cancer cells. Also, the scope of this thesis does not encompass drug delivery considerations. Further research should investigate the improvement of nanoparticle delivery and tumor targeting, as well as the safety and efficacy of this treatment in preclinical and clinical studies through animal studies, histological analysis, pharmacokinetics, biodistribution, therapeutic efficacy, and toxicity to normal tissues.

1.6 Original contributions

This thesis presents an exploration of the potential of decorated MWCNTs in NIR photothermal cancer therapy, with the following original contributions:

1. Developing a computational model that facilitates a better understanding of plasmonic photothermal therapy using plasmonic hybrid carbon nanotubes as mediated heating agents and beyond. This model enables numerical evaluation of the optical and thermal properties of decorated MWCNTs for *in vitro* applications. Additionally, the study of bare and plasmonic-decorated carbon nanotubes allows for the investigation of their thermal and optical spectral distributions (see [**J2, C1**]).

2. The design, conception, and synthesis of hybrid plasmonic nanostructures involved a covalent bonding process to integrate both gold and carbon nanotube components. This innovative approach aims to engineer nanostructures with enhanced near−infrared properties that are specifically tailored for advanced photothermal cancer therapy applications (see [**J2, C1**]).

3. For the first time, the application of anti−Stokes Raman spectroscopy using decorated CNTs as a local temperature probe for direct temperature measurements at the cellular level. This technique provides a useful tool for monitoring temperature changes during photothermal therapy and for optimizing treatment parameters (see [**J3, C2**]).

1.6.1 Thesis Publications

The publications resulting from the work presented in this thesis are as follows:

1. [**J1**]**Fatma Oudjedi** and Andrew Kirk, 'Near-Infrared Nanoparticle-Mediated Photothermal Cancer Therapy: A Comprehensive Review on The Advances in Monitoring and Controlling Thermal Effects for Effective Cancer Treatment", *manuscript in preparation.*
   Contributions:
   - F.O. structured and synthesized the literature review, including figures and tables, and wrote the manuscript.
   - A.K. guided the literature review process and manuscript revision.
2. [**J2**] **Fatma Oudjedi**, Seung Soo Lee, Miltiadis Paliouras, Mark Trifiro, and Andrew Kirk, "Enhancing *in vitro* photothermal therapy using plasmonic gold nanorod decorated multiwalled carbon nanotubes," Biomed. Opt. Express 14, 6629-6643 (2023); doi.org/10.1364/BOE.504746.
   Contributions:
   - F.O. conceived and designed the experiments, performed the experimental work, collected and analyzed the data, and wrote the manuscript.
   - S.S.L. assisted in material synthesis, conducted additional experiments, and contributed to the data analysis.
   - M.P. and M.T. provided conceptual guidance, technical support, and interpretation of results and participated in manuscript revision.
   - A.K. guided experimental design, data analysis, and manuscript revision.
3. [**J3**] **Fatma Oudjedi**, Seung Soo Lee, Miltiadis Paliouras, Mark Trifiro, Sebastian Wachsmann-Hogiu, and Andrew Kirk, "*In vitro* Raman thermometry using gold nanorod-decorated carbon nanotubes", *submitted manuscript.*
   Contributions:

- F.O. conceived and designed the experiments, performed the experimental work, collected, and analyzed the data, and wrote the manuscript.
- S.S.L. assisted in the nanoparticle design, and cell culture maintenance work and participated in manuscript revision.
- M.P. and M.T. provided PC3 cell lines and culture-grade equipment and participated in manuscript revision.
- A.K. and S.W.H. guided experimental design, data analysis, and manuscript revision.

1.6.2 Other Publications

1. [**J4**] Seung Soo Lee, **Fatma Oudjedi**, Andrew Kirk, Mark Trifiro, and Miltiadis Paliouras, "Photothermal Therapy of Papillary Thyroid Cancer Tumor Xenografts with Targeted Thyroid Stimulating Hormone Receptor Antibody Functionalized Multiwalled Carbon Nanotubes", Cancer Nanotechnology, 14, 31 (2023); doi.org/10.1186/s12645-023-00184-9.

2. [**J5**] **Fatma Oudjedi**, Juan Rodrigo Velez, Juan Hernández-Cordero and Andrew Kirk, "Numerical assessment of plasmonic decorated Multiwalled Carbon Nanotubes under Pico short laser pulse", *manuscript in preparation.*

1.6.3 Conference Publications

1. [**C1**] **Fatma Oudjedi**, Seung Soo Lee, Miltiadis Paliouras, Mark Trifiro, and Andrew Kirk "Gold nanorod-decorated multiwalled carbon nanotubes for near-infrared photothermal therapy", Proc. SPIE 11978, Plasmonics in Biology and Medicine XIX, 1197809 (3 March 2022); doi.org/10.1117/12.2608307.

2. [**C2**] **Fatma Oudjedi**, Seung Soo Lee, Miltiadis Paliouras, Mark Trifiro, Sebastian Wachsmann-Hogiu, and Andrew Kirk, "Gold Nanorod-Decorated Carbon Nanotubes for Cellular Level Raman Thermometry", The 84th JSAP Autumn Meeting 2023 (Oral presentation).

1.7 Thesis Organization

The remainder of this thesis is organized as follows:

Chapter 2 provides a comprehensive overview of the fundamental principles of photothermal therapy and highlights the potential of plasmonic nanomaterial therapy as a novel approach to cancer treatment. This chapter focuses specifically on the use of GNRs and MWCNTs as photothermal agents, highlighting the unique properties that make them attractive PTT candidates. Recent advancements in PTT and theragnosis using carbon nanotubes and gold nanoparticles have also been examined and evaluated in detail. By examining the current state of the art in PTT, this chapter provides a strong foundation for subsequent discussions of the proposed use of gold−decorated MWCNTs as plasmonic photothermal transducers for cancer treatment.

Chapter 3 investigates the potential benefits of using decorated plasmonic MWCNTs in NIR photothermal therapy for nontarget PC3 cell lines. The optical and thermal properties of the MWCNTs were rigorously evaluated using numerical simulations, as well as microscopic and spectroscopic characterization of the hybrid nanomaterial. Furthermore, an *in vitro* assessment of cell viability after several irradiation treatments and cytotoxicity was meticulously examined.

Chapter 4 presents an investigation into the potential use of decorated MWCNTs as local temperature and therapeutic probes for Raman thermometry at the cellular level. This chapter describes how the Raman mode can be extracted using the Boltzmann distribution.

Chapter 5 provides a summary of the findings obtained from previous chapters and their importance in advancing cancer imaging and photothermal therapy through targeted nanoparticle delivery. Furthermore, this chapter provides an overview of the potential applications of decorated plasmonic MWCNTs in cancer therapy, including diagnosis, imaging, and targeted therapy. This chapter also discusses future directions for enhancing the effectiveness of cancer treatment through the development of more advanced nanoparticle−based delivery systems.

The integration of spectroscopic techniques, such as Raman thermometry and plasmonic nanobubbles, and the use of advanced computational models and simulations can provide a more comprehensive understanding of the behavior of decorated MWCNTs in biological systems.

Transition to Next Chapter

Chapter 2 delves into a comprehensive exploration of foundational principles underlying PTT, with a specific emphasis on the innovative application of plasmonic nanomaterials for cancer treatment. Notably, GNRs and MWCNTs emerge as focal points in the discussion, showcasing their potential as effective photothermal agents. The distinctive properties inherent in GNRs and MWCNTs render them particularly compelling candidates for PTT applications.

A critical analysis of recent advancements in the field is the central focus of this chapter. Specifically, developments in PTT and theragnosis employing carbon nanotubes and gold−based nanoparticles undergo thorough examination and evaluation. By scrutinizing the current state of PTT, this chapter establishes a foundation, laying the groundwork for subsequent discussions.

Moreover, this chapter sets the stage for a detailed exploration of the proposed application of gold−decorated MWCNTs as plasmonic photothermal transducers in the context of cancer treatment. The insights gained from this examination contribute to a nuanced understanding of the potential efficacy and challenges associated with utilizing these nanomaterials in the evolving landscape of cancer therapeutics.

Chapter 2

Literature Review

2.1 Introduction

Cancer is a major public health concern, with significant mortality rates worldwide. According to the International Agency for Research on Cancer (IARC), cancer is the second leading cause of death, accounting for one in every six deaths globally [22]. In the United States, there were estimated to be 1,958,310 new cancer cases and 609,820 cancer−related deaths during 2023 [23]. Conventional cancer treatments, such as chemotherapy, radiation therapy, and surgery, can have significant side effects including tumor recurrence, high toxicity, low efficacy, and damage to surrounding healthy tissues. Several oncological modalities including cryoablation [14], high−intensity focused ultrasound [24], radiofrequency ablation (RFA) [12, 25], microwave thermosphere ablation (MTA) [25], and laser interstitial thermal therapy (LITT) [26] have been developed for localized ablation to reduce the side effects of conventional treatments. However, these thermal−based modalities have limitations such as the need for precise special control, invasiveness, and treatment homogeneity. There is an urgent clinical need for cancer treatment that is highly selective, effective, noninvasive, cost−effective, and treats local malignant tumors without adversely affecting adjacent tissues and vessels. Photothermal therapy is an emerging approach to cancer treatment that utilizes light−absorbing nanomaterials to generate localized heat and destroy cancer cells. Unlike the current mainstream treatments, which are invasive and involve antenna and electrode

insertion, nanoparticle−mediated photothermal ablation of tumors with near−infrared light is a less invasive tool for treating cancer. This treatment is highly efficient in damaging cancerous cells by apoptosis [27] or necrosis [28] and has potential benefits in treating recurrent and resistant cancers compared to conventional cancer treatments.

This chapter investigates the use of nanoparticles in PTT, focusing on the heating properties of selected nanomaterials and their versatile functions in the theragnosis of photothermal cancer treatment. We provide an overview of the mechanism and requirements of PTT, recent developments in the use of spectroscopic techniques to diagnose, guide, and monitor treatment effectiveness, and emerging thermal simulation and modeling techniques and their potential uses in preclinical PTT planning. Finally, we highlight the recent progress in achieving clinical translation in the field.

2.2 Fundamental of Photothermal Therapy

2.2.1 Light−Tissue Interaction

Phototherapy is a therapeutic modality that has been used in the medical field for centuries, employing light as a means of treating diseases. Its origins can be traced back to [29] ancient civilizations, such as the Egyptians and Greeks, who practiced heliotherapy for various health conditions. The interaction between light and tissue is influenced by various factors, including the intensity and wavelength of the light, the type of tissue, and the presence of chromophores that absorb light, such as blood and melanin [30]. In laser−tissue interactions, the amount of light absorbed depends on the optical properties of the tissue and the wavelength of light [30, 31]. The Beer−Lambert law is a widely recognized principle for analyzing the interactions between light and matter [32]. This principle pertains to the attenuation of collimated light as it passes through a tissue layer, resulting in diminishing intensity due to absorption. The mathematical formula expressing this concept is as follows:

$$I(x) = (1 - R)I_o \exp(-\mu_a x) \tag{2.1}$$

where $I(x)$ is the intensity of the light at a specific distance x within the tissue, I_o is the initial intensity of the light, μ_a is the absorption coefficient of the material, and R is the coefficient of Fresnel reflection at the tissue surface when the light beam is perpendicular to it. It is important to note that the Beer−Lambert law is based on several assumptions, including that the light source is monochromatic, and that the tissue is homogeneous and isotropic. Additionally, this law only considers the absorption of light and does not consider other factors that may affect the transmission of light through tissues, such as scattering and fluorescence.

2.2.2 Near−Infrared Biological Window

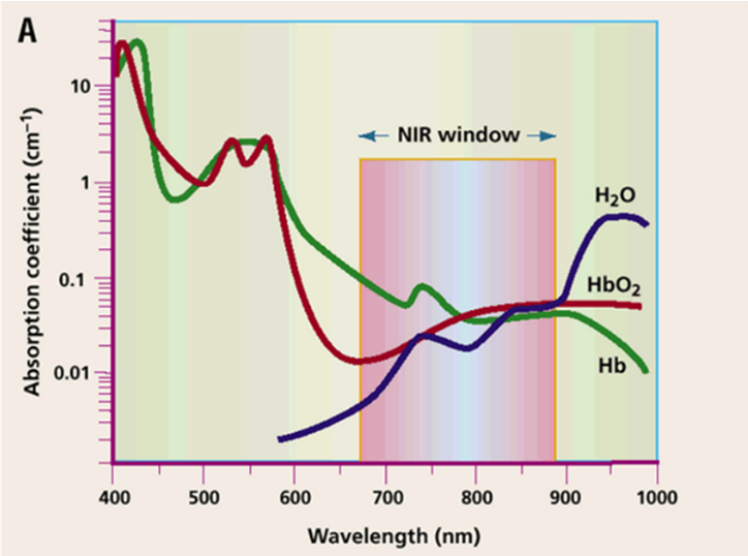

Fig. 2.1. The NIR therapeutic window is suitable for photothermal therapy because of minimal light absorption by water (H_2O), hemoglobin (Hb), and oxyhemoglobin (HbO_2), adapted with permission from Weissleder et al. [1].

In phototherapy, the near−infrared biological window is a fundamental principle that pertains to the spectral region where tissues exhibit reduced absorption and scattering, resulting in increased transparency [33]. The biological window comprises two areas: the first biological window (NIR−I), which spans from 750 to 950 nm, and the second biological

window (NIR−II), which extends from 1000 to 1400 nm [1], as shown in Fig. 2.1. The windows in question display a reduced capacity for absorption and scattering by tissue, making them well−suited for use in phototherapy. It is therefore essential to comprehend and employ these windows to attain deeper tissue penetration and prevent the negative consequences of overheating normal tissues during phototherapy.

2.2.3 Photoresponsive Therapy

Photoresponsive therapy involves agents that respond to light, activating a therapeutic response in a targeted area. It encompasses two main categories, photodynamic therapy (PDT) and photothermal therapy, each with their respective mechanisms. PDT utilizes visible−light−activated photosensitizers that generate reactive oxygen species (ROS), causing tumor cell death [34, 35]. While PDT has been demonstrated to achieve positive clinical outcomes [34–36], the limitations of PDT include low absorption cross−section, enzymatic degradation, and limited photosensitizer penetration into larger tumor sites [34, 35]. In contrast, PTT employs near−infrared laser−activated nanoparticles that generate heat to partially destroy tumor cells [37]. The photons absorbed by the photothermal agent produce excited states, which dissipate excess energy via vibrational relaxation, thereby increasing the kinetic energy and heating of the surrounding cell medium. Unlike PDT, PTT is minimally invasive and can be used passively or targeted to minimize the damage to healthy tissues. Exploring PTT as an alternative therapeutic approach for cancer therapy will be the focus of this review.

2.2.4 Enhanced Permeability and Retention Effect

Nanoparticle targeting can be achieved through either active or passive pathways. Passive targeting is achieved through the enhanced permeability and retention (EPR) effect [16], as illustrated in Fig. 2.2, which exploits the abnormal vasculature and impaired lymphatic drainage of tumors. After being introduced into the tumor microenvironment by leaking blood vessels, nanoparticles can be activated by external light to induce the thermal ablation of cancer cells. However, intravenous injection typically results in low nanoparticle concentration and approximately 0.7% delivery efficiency, which limits treatment effectiveness [38].

Therefore, efforts are being made to optimize nanoparticle design and delivery, including improving circulation time, targeting specificity, and increasing accumulation in the tumor microenvironment [39].

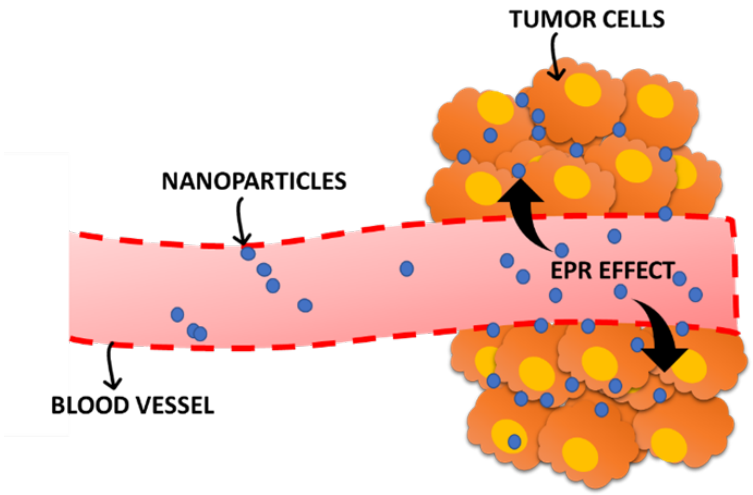

Fig. 2.2. The enhanced permeability and retention effect is a mechanism where the nanoparticles (blue color) accumulate in the tumor region (orange color) through the leaked blood vessel (red color).

2.2.5 Thermal Therapy Regimes

In thermal clinical regimes, various temperature stages characterize the treatment methods, including hyperthermia−induced apoptosis, necrosis, thermal ablation, and carbonization, each with distinct biological effects [6]. Hyperthermia involves heating tissues in the range of 41−48 °C, which has demonstrated therapeutic benefits such as partial cell destruction, increased drug delivery [40], and enhanced immune response [41]. In PTT, a mild cancer treatment, hyperthermia−induced apoptosis occurs at 41−48 °C, causing protein denaturation, oxidative stress, and cell inactivation [29]. Table 2.1 summarizes the different temperature ranges, biological effects, and photothermal mechanisms.

Table 2.1. Thermal clinical regimes involve different biological and physiological mechanisms [3–6].

Temperature (°C)	Biological Effects	Mechanisms
37	Non−thermal photobiological effect.	Normothermia
$41 < T < 48$	Enzyme inactivation, change in membrane permeabilization, and partial cell damage.	Hyperthermia−induced apoptosis
$48 < T < 50$	Irreversible cell damage, protein unfolding, and coagulation.	Hyperthermia−induced necrosis
$50 < T < 60$	Irreversible cell damage, denaturation of proteins, DNA damage, and complete cell death.	Thermal ablation
$T > 100$	Cell membrane carbonization, tissue blackening.	Carbonization

2.3 Photothermal Agents in Photothermal Therapy

Various groups have recently studied different types of nanoparticles with excellent photothermal transduction capabilities for photothermal heating therapy. To ensure maximum effectiveness, nanoparticles must meet specific criteria, including strong near−infrared absorption, localization at the tumor site, and compatibility with biological substances. Additionally, effective photothermal agents must possess high photothermal therapy efficiency, high absorption cross−section in the NIR spectrum and high photothermal conversion efficiency. Nanoparticle−mediated photothermal therapy has emerged as a promising approach for the treatment of tumors using laser−induced thermal ablation. The application of this technique is contingent upon its ability to regulate heat generation under laser illumination by tailoring the concentration, size, structure, and dispersion of nanoparticles within the tumor. It is essential to accurately evaluate the thermal and optical properties of photothermal agents to optimize the treatment parameters and predict therapeutic outcomes. Numerical simulations and modeling using tools such as the finite element method (FEM) [42], finite−difference time−domain (FTDT) [43–47], and discrete dipole approximation (DDA) [48–50] provide an

effective approach for this assessment. These computational methods provide a thorough understanding of the thermal and optical properties of photothermal agents under various conditions. They encompass the modeling of heat generation and dissipation processes as well as the electromagnetic radiation mechanism of nanomaterials, which involves plasmonic localized heating of metals or non−radiative relaxation of semiconducting materials [51] or thermal vibrations of molecules [52]. A common metric of nanoparticle performance is photothermal conversion efficiency, which measures the effectiveness of the nanoparticle in transforming incident power into heat, which can induce cell death [53–55]. The following equation defines the efficiency [54, 55]:

$$\eta = \frac{hS(T_{max} - T_{amb}) - Q_o}{I(1 - 10^{-A_\lambda})} \tag{2.2}$$

where T_{amb} is the ambient temperature, T_{max} is the equilibrium temperature, Q_o is heat dissipated as a result of the light absorbed by the aqueous solution and the sample cell in the absence of nanoparticles, h is a heat−transfer coefficient, S is the surface area for radiative heat transfer, I is the laser power, and A_λ is the optical density of the nanoparticle solution at the laser wavelength. Another important factor that determines the effectiveness of thermal treatment is the magnitude of the temperature increase and duration of the treatment, referred to as thermal dosimetry [56–58].

Numerous nanomaterials have been explored for photothermal cancer therapy, including noble metals, carbon−based nanomaterials, quantum dots [59], metal oxide nanomaterials [60], and organic polymers[61]. Among these, carbon−based nanostructures (such as carbon nanotubes [62, 63], graphene oxide [64–66], carbon dots [67], carbon nanohorns [68], and fullerenes [69]), and various morphologies of gold−based nanoparticles (including gold nanospheres[19], nanoshells [70–72], nanorods [73, 74], and nanomatryoshkas [75]) have been the most studied. Here, Table 2.2 summarizes recent studies on PTT. Sections 2.3.1 and 2.3.2 discuss the optical characteristics and contemporary progress in the use of gold− and carbon−nanotube−based nanostructures for photothermal cancer therapy.

2.3.1 Carbon Nanotubes

Carbon nanotubes have become highly attractive materials for photothermal therapy because of their unique optical and surface properties, as well as their ability to convert near−infrared radiation into heat [76]. Since their identification on the cathode of a carbon arc employed for fullerene synthesis by Iijima in 1991 [77], multiwalled carbon nanotubes have attracted considerable interest owing to their distinctive physicochemical properties, including optical, surface, thermal, and electrical characteristics [78–80]. Their anisotropic structure, which results from their high aspect ratio (length/diameter), has led to experimental and theoretical investigations of their polarized Raman spectra [80], optical absorption [79], antenna effects [81], and photoluminescence responses [82]. Carbon nanotubes consist of rolled−up graphene sheets in a cylindrical form composed of sp^2 carbon atoms arranged in a hexagonal honeycomb network. These one−dimensional carbon nanostructures can be composed of different diameters, lengths, and chiralities, which determine their structural orientation through the chiral vector (n, m). They can behave as semiconductors or metals, or even as a mixture of both, depending on chirality [83–85]. Carbon nanotubes possess a high aspect ratio and large surface area, which increase their chemical activity [86, 87]. The available surface area is dependent on the length, diameter, and degree of bundling, and chemical vapor deposition (CVD) is the preferred method for controlling the morphology. This section discusses the optical and surface functionalization properties of carbon nanotubes (CNTs) that render them suitable for photothermal therapy.

2.3.1.1 Optical Properties

MWCNTs, with a size−aspect ratio influencing remarkable electromagnetic properties, exhibit broad absorption spectra across the NIR region, which is crucial for use in therapeutic windows in biological applications. MWCNTs exhibit threefold greater optical absorbance than single−walled carbon nanotubes (SWCNTs), attributed to the increased electron density per carbon particle, resulting in enhanced absorption in NIR light [88–90]. The antenna effect of MWCNTs, referring to their efficient absorption and enhancement of the local electromagnetic field, is influenced by incident light wave polarization and antenna length [81]. In the polarization antenna effect, the response of CNTs varies with the polarization

direction of the incoming electromagnetic wave [81, 91]. Meanwhile, the length antenna effect shows an increased response when the nanotube length exceeds half of the incident wavelength [90]. Nitrogen−doped MWCNTs, especially those with lengths between 700 and 1100 nm, effectively couple optical wavelengths under 1064 nm, behaving as optical antennas with enhanced heat delivery around them [90]. Moreover, MWCNTs exhibit electromagnetic properties with anisotropic responses analogous to those of graphite [81, 91]. Unlike SWCNTs, which exhibit specific peak absorption resonances, MWCNTs behave as highly efficient dipole antennas with broad absorption spectra [83, 92]. The optical absorption spectra of the MWCNTs do not display van Hove transitions in their optical absorption spectra, except for a peak at approximately 230 nm, which is the peak resonance due to the $\pi - \pi^*$ electron transition [84]. The photophysical process enabling CNTs to convert NIR radiation into heat is linked to electron and phonon band structures [84]. The inherent ability of CNTs to produce heat in response to NIR radiation can be attributed to the decay of photoexcited electrons back to their ground state, which results in the generation of thermal energy in the surrounding environment [84]. MWCNTs exhibit a high conversion efficiency compared to other carbon−based materials [93, 94]. Finally, their heating efficiency, reported at different NIR wavelengths, is wavelength−independent and surpasses that of gold nanorods, which have a high efficiency only at 808 nm because of their surface plasmon resonance [2], as shown in Fig. 2.3.

2.3.1.2 *In Vivo* and *In Vitro* Photothermal Treatment

The Dai and Choi research groups were the first to report the application of SWCNTs in photothermal therapy [95–97]. Their findings demonstrated that SWCNTs could be utilized with a lower laser power and irradiation time than gold nanoshells [95–97]. Kam et al. reported the selective destruction of HeLa cells incubated with PEGylated SWCNTs conjugated with folic acid under NIR laser light exposure [95]. Some groups reported that MWCNTs required less energy to achieve similar results using SWCNTs and that they were 20−fold more efficient than SWCNTs [88, 94, 96]. In addition to SWCNTs, Torti et al. tested nitrogen−doped MWCNTs as heat transducers for the photoablation of kidney cancer cells, which resulted in over 90% cancer cell death under continuous NIR laser radiation at 3

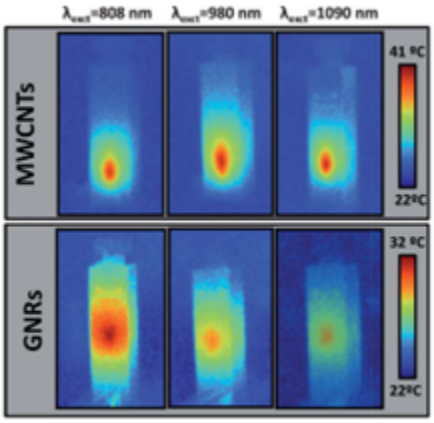

Fig. 2.3. Thermal images of MWCNTs and GNRs at three different wavelengths. MWCNTs are wavelength−independent exhibiting temperatures up to 40 °C, compared to GNRs exhibiting the highest temperature at 800 nm. Adapted with permission from Maestro et al. [2].

W/cm^2 for 4 min [90]. Kim et al. studied SWCNTs and MWCNTs as antimicrobial agents [98], whereas Biris et al. demonstrated cervical cancer HeLa cell ablation with MWCNTs as a photothermal agent [99]. Burke et al. reported MWCNTs−mediated thermal ablation of mice bearing kidney cancer cells under NIR laser exposure, resulting in long−term survival and prevention of tumor recurrence [88]. Gosh et al. carried out an *in vivo* photothermal experiment with DNA−encased MWCNTs, which led to complete tumor ablation without long−term damage to surrounding healthy tissues [94]. Under 1064 nm laser irradiation at 2.5 W/cm^2, the well−dispersed DNA−encased MWCNTs were efficient at increasing heat production by up to 3 fold compared to non−DNA−encased MWCNTs, as well as at completely ablating xenograft tumors without long−term damage to surrounding healthy tissues [94]. Fisher et al. reported MWCNT−containing PC3 (i.e., human prostate cancer) and murine renal carcinoma (RENCA) tumor sample cell ablation [89]. They evaluated the thermal deposition of CNT in the PC3−surrounded cells. They observed no PC3 and RENCA cell viability using a 0.1 mg/mL dose of MWCNTs coupled with a continuous wave 1064 nm NIR laser at 15.3 W/cm^2, with varied heating duration. The authors evaluated the laser heating of cells with and without MWCNTs inclusion and examined the lethal temperature elevation through heat shock protein expression and extracellular uptake and

distribution using transmission electron microscopy (TEM) imaging [89]. Lee et al. studied non−target and target tumor cells with PEGylated MWCNTs under laser exposure [63]. In contrast, Picou et al. evaluated the spatiotemporal temperature distribution of MWCNTs injected into the subcutaneous layer of chicken tissue under different laser parameters [100]. Moreover, MWCNTs have been used to treat resistant cancers, such as glioblastoma [62, 101], and recurrent cancers, such as breast cancer [102, 103]. Some studies have reported the incorporation of dopants into defect sites, such as boron [104] and nitrogen [90], as well as the optical properties and heat conductivity of carbon nanotubes.

2.3.1.3 Biocompatibility

Carbon nanotubes have been investigated for use in photothermal therapy in both *in vivo* and *in vitro*. Several studies have found that there are no cytotoxic effects when carbon nanotubes are incubated with tumor cells. However, pristine carbon nanotubes are neither soluble in aqueous media nor biocompatible with living organisms. The low solubility and dispersibility of carbon nanotubes in aqueous media are caused by their Van der Waals interaction and their $\pi - \pi$ interaction among nanotubes [87]. This limitation can be overcome through surface functionalization, which increases the solubility of CNTs and decreases their toxicity in biocompatible solvents [86, 105]. Covalent and non−covalent functionalization are the two major approaches for surface functionalization, depending on the biomedical applications of CNTs [94, 95, 106]. Functionalized carbon nanotubes were rapidly cleared from the blood circulation through the renal excretion route [88, 105–108]. Carbon nanotubes can also act as delivery vehicles for drugs, nucleic acids, and imaging agents owing to their ability to cross cell membranes [109]. The cytotoxicity of carbon nanotubes and their long−term effects are still under investigation [110]. Before clinical trials, the toxicological effects of multiwalled carbon must be considered in terms of pulmonary response, renal clearance, and biodistribution.

2.3.2 Gold−Based Nanostructures

Over the past decades, there has been growing interest in the use of gold nanoparticles for photothermal therapy in cancer treatment [111, 112]. Plasmonic nanoparticles, particularly gold nanoparticles (GNPs), gained significant attention in the early 2000s for their potential

application in photothermal cancer therapy. Boyer et al. [113] were the first to report work on plasmonic imaging for heating and detection. In the following year, two groups [57, 71] investigated plasmonic photothermal therapy using gold nanoparticles incubated with tumor cells to induce hyperthermia. Gold nanoparticles are the most commonly used noble metal−based nanostructures in photothermal cancer therapy because of their easy synthesis and functionalization with targeting agents such as aptamers [114] and peptides [115, 116].

2.3.2.1 Optical Properties

Gold−based nanostructures exhibit exceptional optical and thermal properties, making them ideal candidates for biomedical applications. GNPs possess optical properties that facilitate efficient photothermal conversion owing to their remarkable plasmonic−resonance effect. When light interacts with a metal nanoparticle, such as gold, the conduction electrons in the metal collectively oscillate in response to the incident electromagnetic field, giving rise to plasmons. This resonance typically occurs on the surface of a metal, known as surface plasmon resonance (SPR), because the disturbance of the incident electromagnetic wave on the metal decreases rapidly with depth [117]. When SPR occurs in nanoparticles, called localized surface plasmon resonance (LSPR), which is comparable in size to the wavelength of the incident light, two important effects are observed in GNPs: an enhancement effect of the local electromagnetic field and an increased extinction coefficient [117]. LSPR leads to the enhancement of the electromagnetic fields near the GNP surface, which can be several orders of magnitude higher, with the highest enhancement occurring in areas of the highest local curvature (hot spots). This phenomenon contributes to the amplification of spectral signals for substances in close proximity, ultimately improving the detection sensitivity surface [117].

Increasing the aspect ratio of gold nanoparticles, from spherical to rod−like, modifies the LSPR response within the NIR region. Among the various types of gold−based nanostructures, gold nanorods (GNRs) exhibit a strong longitudinal plasmon resonance peak in the NIR region, making them highly desirable for *in vivo* imaging and therapy because of the enhanced penetration depth of NIR light [118]. GNRs display considerable optical absorption in the NIR region, with greater absorption efficiency when irradiated along their long axis, which corresponds to the longitudinal plasmon in the NIR region [119]. In contrast, the transverse

plasmon peak is related to the excitation of the transverse axis of the GNRs, displaying a lower absorption magnitude in the visible region [118]. Gold nanoshells are another type of gold−based nanostructure whose absorption and scattering properties can be modulated by adjusting the ratio of the shell thickness (comprising a thin layer of gold) to the core radius (consisting of a dielectric material) [120, 121]. The plasmon resonance peak of gold nanoshells (GNSs) can be fine−tuned by altering the size of the silica core and thickness of the gold shell, making them highly attractive for *in vivo* imaging and therapy because of their strong absorption of NIR light [122]. The GNSs optical response arises from the hybridization of dipolar plasmons in core−shell nanostructures, resulting in the splitting of low and high absorption peaks [123]. Scattering and absorption are competing processes in which the scattering contribution increases as the volume ratio of the nanoshell increases [124]. Gold nanocages comprise a hollow gold shell with a porous wall, allowing straightforward functionalization with targeting agents Similar to GNRs and GNSs. The plasmon resonance peak of gold nanocages (GNCs) can also be adjusted to the NIR region, which makes them highly attractive for *in vivo* imaging and therapy [125, 126].

2.3.2.2 *In Vivo* and *In Vitro* Photothermal Treatment

The utilization of gold−based nanostructures in photothermal cancer therapy has been extensively studied and has been demonstrated to be highly effective in both *in vitro* and *in vivo*. For instance, GNPs functionalized with anti−HER2 antibodies have been utilized to selectively target HER2−positive breast cancer cells and induce cell death upon exposure to near−infrared light [127]. *In vivo* studies have demonstrated the ability of gold−based nanostructures to selectively target and destroy tumors upon exposure to NIR light. Furthermore, human clinical trials on GNP−assisted photothermal therapy have been ongoing in recent years. In recent studies, AuroLase therapy, developed by Nanospectra Bioscience Inc., is currently undergoing human clinical trials utilizing 150 nm silica−gold nanoshells coated with PEG, which are intravenously injected into the bloodstream [21]. Kharlamov et al. conducted a clinical trial evaluating the safety and feasibility of atheroprotective interventions, where patients received nano−interventions with silica−GNPs or silica−iron−bearing GNPs via stem cells [128]. At 12 months post−therapy, results were comparable to a control group with

stent implantation, showing a low incidence of thrombosis and target lesion revascularization [128]. Collectively, these clinical studies indicate the promising potential of gold−based nanostructures for cancer therapy (see Table 2.3).

2.3.2.3 Biocompatibility

Gold−based nanostructures possess a range of desirable properties that make them appealing candidates for photothermal cancer therapy. The biocompatibility, photostability, low cytotoxicity, and uniform preparation and surface functionalization of gold nanoparticles particularly make them suitable for medical applications [112]. However, some challenges must be addressed. For instance, there are concerns regarding the potential cytotoxicological effects of employing cetrimonium bromide (CTAB) for the chemical functionalization of gold nanoparticles *in vitro* [129, 130] and shape deformation of gold nanorods at high pulse intensities [131, 132]. Overall, gold−based nanostructures that offer adjustable plasmonic characteristics, effective photothermal conversion, and the capacity to absorb light in the near−infrared range are highly promising for a variety of biomedical applications such as imaging and therapy.

2.3.3 Carbon Nanotubes Decorated with Metal Nanoparticles

Carbon nanotubes decorated with metal nanoparticles have gained significant attention in recent years owing to their unique properties, including high surface area, excellent thermal conductivity, and tunable electronic properties. These hybrid materials have shown great potential in various applications, including sensing [133–135], photocatalysis [136, 137], and photothermal treatment [138–141]. Gold nanoparticles can serve as photothermal sources through non−radiative decay and act as a local antenna to enhance the optical energy absorption of CNTs at plasmon frequencies. CNTs decorated with plasmonic nanoparticles have shown significant potential in PTT applications. For example, CNTs functionalized with GNCs have been shown to effectively ablate prostate cancer cells *in vitro* using near−infrared laser irradiation [142]. Several studies have reported plasmonic metal interaction with graphene, in which metals act as local nanoantennas and enhance optical energy absorption and photocurrent enhancement [143–145]. Studies of GNP−decorated reduced graphene

oxide (rGO) have reported photothermal enhancement and higher light absorption efficiency than uncoated rGO [146]. Another study demonstrated that rGO functionalized with silver nanoparticles (AgNPs) can be used for the targeted destruction of breast cells using laser irradiation [147]. Additionally, a novel theragnosis application was reported by developing a CNT ring coated with GNPs [148]. This hybrid nanostructure exhibits strong Raman and photoacoustic signals that are ideal for surface−enhanced Raman scattering−based sensors, imaging, and photothermal cancer ablation [148]. Zhu et al. demonstrated a novel hybrid gold−carbon nanostructure that is ideal as a photothermal agent for cancer therapy [141]. The gold nanostar−decorated MWCNTs exhibited higher photothermal efficiency than the gold nanoparticles under 808 nm laser irradiation at a power density of 1 W/cm^2. Ou and Huang reported the formation of carbon nanotube−gold nanoparticle composites [149]. The gold nanoparticles are interlinked to a pyrene component, which is non−covalently attached to the sidewall of CNTs via $\pi - \pi$ stacking interaction. Using UV−vis absorption spectroscopy, they observed a redshift of the surface plasmon resonance absorption band of gold nanoparticles in an aqueous solution containing MWCNT− gold nanoparticle composites. Several methods have been developed to decorate carbon nanotubes with metal nanoparticles, either by covalent or non−covalent formation along the nanotube surface [150–154]. Recently, a study showed that enhancing the light−to−heat conversion efficiency of MWCNTs by covalently bonding on its surface gold nanorods significantly enhances their photothermal properties by 4.9 times per unit mass of CNT [155]. These studies have demonstrated remarkable progress over the last 10 years using MWCNTs as photothermal agents in photothermal therapy. However, challenges remain in thermal ablation treatment, such as well−located and well−defined heating spots [156, 157].

Table 2.2. Summary table of photothermal agents: characteristics, laser parameters, type of studies, and therapeutic applications.

Nanomaterials	**Laser parameters**	***In Vitro*/*In Vivo* studies**	**Therapeutic remarks**	**Ref.**
MWCNTs−PEG	CW, 532 nm, 2.7 W/cm^2, 30 s	*In vitro*, prostate cancer cell lines (LNCAP)	65% *in vitro* cell ablation with consistent bulk temperature in the cell−MWCNT solution post−laser exposure.	[63]
MWCNTs−DSPE-PEG	CW, 970 nm, 3 W/cm^2, 60−180 s	*In vitro*, glioblastoma multiforme (GBM) cell lines	MWCNTs do not cause heat shock response to GBM cell lines.	[62]
MWCNTs	CW, 1064 nm, 3 W/cm^2, 15−30 s	*In vitro*/*in vivo*, tumor−bearing mice with kidney cancer cells	Long−term survival, prevention of tumor recurrence, complete ablation in 80 % of mice treated with 100 μg of MWCNT.	[88]
MWCNTs	CW, 1064 nm, 15.3 W/cm^2, 1.5−5 min	*In vitro*, human prostate cancer (PC3) and murine renal carcinoma (RENCA) tumor sample cell ablation	Ablation through heat shock protein expression and extracellular uptake, distribution observed via TEM imaging.	[89]
Nitrogen−doped MWCNT	CW, 1064 nm, 3 W/cm^2, 4 min	*In vitro*, kidney cancer cell lines	Evaluation of MWCNT length correlation with photothermal effects. Longer CNTs (1100 nm) are better in cell ablation (up to 95%).	[90]
DNA−encased MWCNTs	CW, 1064 nm, 2−4 W/cm^2, 30−70 s	Tumor−bearing mice with xenografts formed from human prostate cancer (PC3) cells	Complete ablation of xenograft tumors without long−term damage to surrounding healthy tissues.	[94]

SWCNTs−PEG	CW, 808 nm, (3.8 W/cm^2, 76 W/cm^2), 3 min	*In vitro*/*in vivo*, tumor−bearing mice− with human epidermoid mouth carcinoma tumors	Destruction of tumors without harmful side effects or recurrence over 6 months.	[96]
MWCNTs	CW, 1064 nm, 1 W, 4 s	*In vitro*, cervical cancer HeLa cell lines	Laser exposure resulted in temperatures reaching 95 ^{o}C, inducing localized damage and cell necrosis.	[99]
MWCNTs bound with anti−GD2 monoclonal antibody, and rhodamine B	CW, 808 nm, 6 W/cm^2, 5 min	*In vitro*, neuroblastoma cell lines.	Selective eradication of GD2 expressing neuroblastoma cells, sparing GD2−negative PC12 cells.	[101]
MWCNTs−NH_2	CW, 1064 nm, 3 W/cm^2, 5−45 s	*In vitro*/*in vivo*, breast cancer stem cells	Lethal to both stem and bulk breast cancer cells.	[102]
MWCNTs−PEG	CW, 808 nm, 5 W/cm^2, 2 min	*In vitro*/*in vivo*, breast cancer	Significant damage to MCF−7 and MDA−231 cells*in vitro*, reduced tumor size in mice, protected bone in bone metastasis model.	[103]
MWCNTs− Gold nanostars	CW, 808 nm 1 W/cm^2, 3 min	*In vitro*, melanoma cell line (B16F10)	Cells treated with MWCNTs/gold nanostars exhibited the highest observed cell death.	[141]
SWCNTs−GNPs	CW, 808 nm, 0.25−0.5 W/cm^2, 5 min	*In vivo*/*in vitro* U87MG tumor−bearing nude mice	No scar, no tumor regrowth at 50 days after treatment.	[148]

MWCNTs−GNRs	CW, 808 nm, 2 W/cm^2, 2 min	*In vitro*, prostate cancer cell lines (PC3)	MWCNTs−GNRs exhibited notable cell ablation with abundant cell debris.	[155]
MWCNTs bound with TSHR antibody	CW, 808 nm, 4 W, 2 min	*In vivo*, Tumor−bearing mice with xenografts formed papillary thyroid cancer	predictive modeling and temperature monitoring enabled effective tumor photoablation, leading to a reduction in post−5−week tumor recurrence with TSHR−targeted MWCNTs.	[158]
CW = continuous wave				

Table 2.3. Summaries of photothermal cancer therapy in clinical trials.

Nanomaterials	**Clinical trials (Trial ID)**	**Company name/Sponsor**	**Ref.**
PEG−coated silica−gold nanoshells	Neoplasms of the prostate, 2019 (NCT01679470; NCT00848042)	Nanospectra Bioscience Inc.	[21]
Silica−gold nanoparticles	coronary atherosclerosis, 2015 (NCT01270139)	De Haar Research Foundation	[128]

2.4 Monitoring Photothermal Treatment via Theragnosis

Monitoring cancer cells during treatment is crucial for effective cancer therapy. Thermal imaging is a commonly used tool for real−time monitoring of photothermal treatment, providing visualization of changes in surface temperature during treatment, and offering information on the efficacy of nanoparticles within the tumor. However, it is important to recognize that thermal imaging is limited to surface temperature changes and may not provide information on deeper tumor changes. Photothermal therapy, which employs photoacoustics, fluorescence, Raman spectroscopy, and magnetic imaging, has emerged as a promising treatment and diagnostic tool for cancer. Theragnosis, which is a combination of therapy and diagnosis, integrates the therapeutic effects of photothermal therapy with diagnostic tools for monitoring in situ treatment. Carbon nanotubes and gold nanostructures have been widely used in theragnostic applications to combine imaging and therapy, maximize cancer treatment efficiency, and minimize heat delocalization during tumor ablation. The following section provides a concise overview of the principles of operation, advantages, disadvantages, and current clinical applications of the technologies utilized in diagnostic applications in conjunction with the aforementioned nanomaterials.

2.4.1 Magnetic Resonance Imaging

Magnetic resonance imaging is a valuable tool for theragnosis in photothermal therapy, as it provides high−resolution images of tumors and their distribution within the body. Near−infrared thermal cameras can monitor the temperature on the surface of tumor tissue; however, magnetic resonance imaging (MRI) using proton resonance frequency can simultaneously extract information on the temperature at any depth and provide an image map of the tumor targets.

Carbon nanotubes lack inherent magnetic properties, and consequently, specific contrast agents must be loaded onto their surfaces for magnetic imaging. MRI contrast agents, such as iron oxide and gadolinium complexes, provide either T_1−positive or T_2−negative contrast agents for imaging and tracking of pathological tissues. The conjugation of magnetic

nanoparticles to the carbon nanotube surface results in significant MRI contrast enhancement and the ability to monitor and detect a single cell incubated with CNTs. For example, coating CNTs with magnetic nanoparticles and iron oxide superparamagnetic nanoparticles has demonstrated significant MRI contrast enhancement, making them a potential development for theragnostic therapy.

Various studies have explored the use of MRI−based multifunctional nanomaterials for the detection, treatment, and monitoring of diseases. One such study investigated the use of iron oxide (Fe_3O_4) nanoparticles conjugated onto the surface of MWNTs [159]. Another study reported the development of polydopamine−encapsulated gadolinium−loaded multi−walled carbon nanotubes (MWCNT−Gd@PDA) for dual−modality mapping−guided PTT using the positive signal of MRI [160] in the deeper lymph nodes.

Dai group was the first to report the *in vivo* combination of synergistic NIR photothermally enhanced drug delivery and MRI with iron−cobalt/graphene oxide (FeCo/GC) nanocrystals for targeted drug delivery and imaging [161]. Efficient monitoring of the biodistribution of gadolinium−CNTs injected intravenously into mice was achieved through covalent bonding between oxidized MWCNT and gadolinium complexes. Iron−containing MWCNTs display magnetic contrast properties for magnetic resonance imaging and heating−generating properties for thermal ablation of tumor−bearing mice under 1064 nm laser exposure. Simulations have shown that a slower rate of energy deposition may result in heat diffusion, leading to ineffective treatment and detrimental damage to the surrounding tissue. To achieve simultaneous cell targeting and ablation, CNTs undergo various surface functionalization processes to detect and treat cancerous tissue. For instance, theragnostic therapy is based on the functionalization of magnet−fluorescence using MWCNTs combined with doxorubicin as a chemotherapeutic agent. CNTs have been used in combination with chemotherapy and photothermal therapy to enhance the efficiency of chemotherapeutic agents, without causing significant side effects.

Gold nanostructures such as gold nanoshells [21, 162], gold nanostars [163], and gold nanorods [164] have also been studied for their potential to combine photothermal therapy with real−time magnetic resonance temperature imaging. A recent study introduced a new class of second near−infrared nanotheragnostic agents, referred to as GSM. This agent is composed of gold nanorods coated with silica dioxide and further covered with magnesium

dioxide (MnO_2), enabling dual photoacoustic/magnetic resonance imaging in the second NIR photothermal chemodynamic therapy. The combination of the plasmonic properties of GNRs and the degradation of MnO_2 into Mn_2^+ owing to the presence of protons in the tumor microenvironment allows for a reduced background signal and deeper permeation in tissues. The *in vivo* therapeutic effects of GSM have been investigated in U87MG−tumor−bearing mice [164]. In a separate study, a straightforward and efficacious strategy for the fabrication of theragnostic nanoprobes with heightened sensitivity was introduced. This nanoprobe comprises gold nanostars deposited on the surface of MnO_2 nanosheets, which trigger apoptosis in lung cancer cells upon exposure to photothermal irradiation. Moreover, the nanoprobe possesses magnetic resonance imaging capabilities that are responsive to glutathione (GSH) levels and demonstrates remarkable effectiveness in photothermal therapy for lung cancer. The efficacy of gold nanostars in absorbing near−infrared light has been utilized in nanoprobes to demonstrate their remarkable photothermal conversion efficiency. Furthermore, the redox properties of MnO_2 nanosheets enable the nanoprobe to display magnetic resonance imaging properties that are responsive to the tumor microenvironment [163].

2.4.2 Photoacoustic Imaging

Photoacoustic imaging is a non−invasive diagnostic technique that relies on the photoacoustic (PA) effect, which involves the generation of acoustic waves through the absorption of light in biological tissue. This process entails the use of a light source to illuminate the tissue, typically in the near−infrared region, which leads to thermoelastic expansion and emission of acoustic waves that are detected by an ultrasound transducer. Photoacoustic imaging has several advantages, such as its ability to image deep tissue structures, and is a non−ionizing and non−invasive technique, as acoustic waves can penetrate deeper into the tissue than light. However, to identify pathological tissues in biological systems, photoacoustic contrast agents are necessary because they do not exhibit intrinsic photoacoustic signals. Therefore, high−resolution imaging of deeper tissues is crucial for accurate diagnosis and detection.

Carbon nanotubes are effective photoacoustic imaging agents owing to their phonon absorption properties in the near−infrared region. The photoacoustic effects in CNTs result in the conversion of light energy into acoustic pressure in the surrounding environment, and

CNTs conjugated with contrast agents for acoustic imaging offer high−resolution profiles for deeper tissues. The first decorated carbon nanotube for photothermal therapy was SWCNTs coated with gold layers, developed by the Zharov group [165]. These gold nanotubes can be used for photoacoustic imaging and photothermal therapy, exhibiting plasmon resonance at 850−900 nm and a high photoacoustic signal at a low laser fluence of approximately mJ/cm^2 [165]. Another group has reported hybrid theragnostic agents composed of fullerene nanocrystals (FNCs) and gold nanoparticles for PA imaging and PTT [166]. Coupling FNCs with GNPs for combined photoacoustic imaging and photothermal therapy resulted in a strong photoacoustic signal within colon cells under 680 nm laser excitation [166].

Gold nanostructures have garnered significant attention as potential PA imaging agents in the NIR window, owing to their finely tunable size and morphologies. A recent study investigated the efficacy of sandwich−type gold nanoparticles coated with reduced graphene oxide as a nanotheranostic platform for second NIR window PA imaging−guided photothermal therapy in ovarian cancer [167]. This study highlighted the strong plasmonic coupling between the gold nanoparticles on the reduced graphene oxide surface, which enhanced both the photothermal and photoacoustic effects. In another study, small gold nanorods were explored as theragnostic agents with the development of a macrophage−mediated delivery system to overcome blood vessel barriers and reach hypoxic regions of tumors [168]. A third study introduced a novel theragnostic agent for near−infrared image−guided thermal ablation of mouse tumors. Zhou et al. demonstrated the potential of multifunctional superparamagnetic iron oxide−containing gold nanoshells for photoacoustic−MRI resonance−guided photothermal therapy in mice bearing breast tumors [169].

Although studies on carbon nanotube photoacoustic therapy have primarily concentrated SWCNTs, which exhibit exceptional photoacoustic signals relative to other carbon−based materials, additional research is necessary to assess the efficacy and safety of this therapeutic approach. Nonetheless, photoacoustic imaging, as an imaging modality, has great potential because of its ability to provide high−contrast, high−resolution, and deep−tissue imaging capabilities.

2.4.3 Fluorescence Imaging and Thermometry

Fluorescence is a valuable tool in photothermal therapy, allowing for the visualization and tracking of nanoparticles during treatment and monitoring of changes in the tumor microenvironment. This process involves the emission of light by a material following excitation by an external energy source such as a laser. During fluorescence, a fluorophore molecule absorbs photons at a specific wavelength and emits photons at longer wavelengths, typically in the visible or near−infrared region. A fluorescence imaging system provides high−spatial−resolution imaging of biological systems. Fluorescence imaging typically involves the binding of fluorophore molecules as imaging agents, enabling high spatial resolution imaging of biological systems in the near−infrared region. Researchers have utilized dual−PEGylated phospholipid SWCNTs as photoluminescent and photothermal agents for simultaneous tumor imaging and therapy. The dual imaging and therapy modality resulted in *in vivo* tumor imaging in the 1.0−1.4 μm emission region and NIR heating at 808 nm for photothermal tumor ablation at the lowest laser irradiation power. The fluorescence emission of SWCNTs is determined by the bandgap energies correlated with the Van Hove singularities.

In this study, a multimodal strategy was employed for cancer imaging and therapy, relying on magnetic and fluorescent MWCNTs. The nanotubes were functionalized with magneto−fluorescent carbon quantum dots and doxorubicin, rendering them suitable for the targeted delivery of drugs in cancer therapy [170]. A prior study disclosed that mesoporous carbon nanospheres comprising minute gold nanoparticles laden with IR780 iodide displayed remarkable real−time fluorescence imaging and phototherapeutic capabilities. These carbon−gold hybrid nanocomposites serve as diagnostic and therapeutic probes, exhibiting favorable targeting and exceptional therapeutic effects, including photothermal therapy, photodynamic therapy, and nanoenzyme oxidative therapy for folate−overexpressing gastric cancer in tumor−bearing mice [171].

Recently, a study was conducted to design a near−infrared light−controlled biosensing strategy that employed dual Pt@Gold nanoring@DNA (PAD) probes for fluorescence imaging and targeted PTT of cancer cells. The probes are composed of a photosensitizer, which includes gold nanorings with a platinum framework (Pt@GNR), and a sensor that consists of

functionalized double−stranded DNA (dsDNA) hybrids. These probes can recognize specific cell subtypes and conduct fluorescence imaging under NIR irradiation [172].

Temperature monitoring through fluorescence is an emerging method that measures alterations in the fluorescence emission spectrum or lifespan of a fluorescent probe in response to temperature variations. A previous study used fluorescence lifetime imaging microscopy to assess the temperature distribution within cells during laser−induced hyperthermia. In this study, gold nanorods served as nanoheaters and near−infrared laser illumination generated a temperature gradient across the cells that was precisely measured using nanoscale thermometry. This study was successful in optimizing photothermal therapy parameters by adjusting the concentration of gold nanorods associated with the cells and the laser power density [173]. Finally, one study merged fluorescent nanodiamonds with nitrogen−vacancy (NV) centers and gold nanoparticles within polymer microcapsules to create a hybrid platform for delivering bioactive compounds with thermometric capabilities. The application of laser irradiation triggers the heating and rupture of gold nanoparticles in the polymer−carriers, thereby releasing cargo molecules. Additionally, the incorporation of NV centers facilitates temperature measurements during the non−invasive administration of bioactive compounds [174].

2.4.4 Raman Imaging and Thermometry

Raman spectroscopy, a versatile technique, has found numerous applications in the biomedical field, including imaging, temperature sensing, and spectral analysis. This method involves measuring the inelastic scattering of light, which provides information regarding the molecular structure and chemical composition of a sample. In particular, Raman imaging detects the scattering signals of molecules owing to their vibrations resulting from the phonon scattering process under light exposure, thus providing information on the chemical composition of molecules. For example, SWCNTs exhibit specific Raman spectra, such as the radial breathing mode (100−300 cm^{-1}), G peak at 1580 cm^{-1}, and D peak at approximately 2600 cm^{-1}. Dai and colleagues conducted extensive research on the application of Raman imaging in biological systems using functionalized single−walled carbon nanotubes. Research groups such as Iijima [175] and Fan [176] correlated the temperature change of laser−induced MWCNT with Raman

shifts. However, the majority of extensive studies on Raman image−guided photothermal therapy have utilized GNPs owing to their unique localized plasmonic properties [111].

Surface−enhanced Raman scattering is a refined form of Raman spectroscopy that employs metallic nanoparticles to augment the Raman signal, thereby facilitating the highly sensitive and specific detection of analytes. The utility of surface−enhanced Raman scattering (SERS) in cancer diagnosis and therapy has grown significantly, due in part to its exceptional sensitivity, ability to multiplex, and capacity for subcellular resolution. Through the deployment of SERS−based imaging techniques, cancer cells can be identified both *in vitro* and *in vivo*, and the biodistribution and pharmacokinetics of nanotherapeutics can be monitored continuously. Raman spectroscopy can be employed to measure temperature fluctuations by utilizing the anti−Stokes Raman thermometry method. This technique is based on the anti−Stokes process, which occurs when a molecule's initial state is in an excited vibrational state that is poorly populated, following a Boltzmann exponential distribution at room temperature [177, 178]. As the temperature increased, the population of excited states increased, which led to stronger anti−Stokes signals. During inelastic scattering events, energy is transferred from photons to virtual states, leading to either a loss of energy (Stokes) or an increase in energy (anti−Stokes) [177, 178]. By detecting anti−Stokes Raman scattering, Raman thermometry can measure and detect subtle temperature changes that occur during treatment, provided that the Raman bands do not shift during temperature changes. The intensity ratio of Stokes (I_S) and anti−Stokes (I_{aS}) for a particular Raman band is governed by a temperature−dependent equation [177, 178]that is expressed through the contribution ratio (ρ):

$$\rho = \frac{I_{aS}}{I_S} = \frac{(\omega_l + \omega_\nu)^n}{(\omega_l - \omega_\nu)^n} \exp\left(-\hbar\omega_\nu / k_B T\right) \tag{2.3}$$

where T is the temperature, the k_B is the Boltzmann constant, $\hbar$ is the reduced Planck constant, ω_l is the laser frequency, the ω_v is the frequency of the Raman mode and the exponent n is either the 3^{rd} or 4^{th} power depending on whether the spectra are acquired using a photon counting device or energy detection device [177, 178].

This rapidly growing field of spectroscopy provides a promising solution for measuring

temperatures at the cellular level [179]. Recent advances in nanoprobe Raman thermometry have allowed researchers to measure intracellular temperature [180–182], and other groups have used probe molecules on gold surfaces to measure the temperature of nanoparticles [183–185]. For instance, a group reported Raman thermometry based on the SERS spectra of fluorophenyl isocyanide (FPNC) molecules absorbed on gold nanorods on glass pipettes in cancer cell photothermal therapy.

In general, the combination of photothermal therapy with therapeutic diagnostic methods, such as Raman spectroscopy, fluorescence, photoluminescence, MRI, and thermal imaging, provides a highly effective means of monitoring treatment efficacy in real−time. These methods enable the visualization of alterations in the tumor microenvironment as well as the distribution and effectiveness of nanoparticles within the tumor. The integration of therapeutic diagnostic techniques, including Raman thermometry, is expected to become increasingly important for optimizing treatment outcomes and improving patient outcomes as photothermal therapy continues to progress. Carbon nanotubes have demonstrated significant potential for therapeutic diagnostic applications in cancer treatment. Although carbon nanotubes are still in the early stages of development in the biomedical field, they represent a promising candidate for cancer nanotechnology research. Further research is necessary to optimize these techniques for clinical translation and to fully understand their potential in cancer nanotechnology.

2.5 Planning the Outcome of Photothermal Treatment Temperature

Achieving precise control of tissue temperature presents significant challenges, and optimizing thermal heating is crucial for achieving successful outcomes. However, preclinical planning of photothermal treatment and temperature control is difficult because accurately predicting the temperature distribution within tissues during photothermal therapy is a major challenge. This requires a comprehensive understanding of the optical properties of the tissue and the involved heat transfer mechanisms. This section reviews the use of time−dependent heating protocols to enhance thermal control during PTT and preclinical planning through numerical

simulations and modeling.

2.5.1 Optimization of Heating Protocol

Optimization of the heating protocol is essential to achieve effective photothermal therapy. The choice of laser regime, whether CW or short−pulse, plays a critical role in determining the heating protocol and treatment outcome. The CW laser regime, which involves exposing the tissue to a constant beam of light, enables precise control of the heating rate and temperature. However, this can lead to excessive heating and damage healthy cells. In contrast, the short−pulse laser regime delivers heat to the tissue using short pulses of laser light, resulting in highly localized and efficient heating. Mechanisms such as rapid thermal expansion and stress confinement contribute to selective damage of cancer cells. Rapid thermal expansion induces a transient temperature increase and tissue expansion, while stress confinement confines energy deposition to a small volume. The ultra−short−pulsed lasers, with pulse durations shorter (i.e. $10^{-12} - 10^{-15}$ s) than the characteristic time scales of interacting tissues (i.e. 10^{-9} s), offer high peak intensities with a low pulse fluence [186]. In the context of photothermal effects induced by short−pulse lasers, the rapid heating and subsequent cooling of tissues happen within these characteristic time scales. The thermal relaxation time of tissues, which is the time required for the tissue to equilibrate and dissipate heat, is typically in the range of nanoseconds [187].

The utilization of ultrashort laser pulses for thermal−based eradication of cancer cells through the absorption of nanoparticles represents a promising area of research. Pioneering work in this field involves both theoretical and experimental investigation. In this regard, CNTs have been explored as near−infrared responsive clustering photothermal contrast agents for rapid and highly sensitive detection and elimination of pathogens, including at the single−bacterium level. Observable changes in bacteria viability, resulting from local thermal effects and concurrent bubble formation, were observed at laser fluences between 0.1 and 0.5 J/cm^2, culminating in complete bacteria disintegration at 2−3 J/cm^2. [98]. Additionally, gold nanoparticles have been studied for selective nanophotothermolysis and diagnostics of various targets [188]. Theoretical models have been developed to investigate the interaction of laser pulses with these nanoparticles as well as their heating kinetics and contribution to therapeutic

effects [189, 190]. Thermal models using nanoparticles have also been developed to predict temperature and cell damage in tumors during laser irradiation [191, 192]. Experimental studies have demonstrated that cell death can be more effectively induced with a single pulse of a nanosecond laser than with a continuous−wave laser [192, 193].

The field of ultrashort laser pulse thermal−based killing of abnormal cells targeted by absorbing nanoparticles is an expanding area of research. A comprehensive understanding of the interactions between ultrashort pulsed lasers and nanoparticles in biological systems is necessary for the development of effective cancer treatments. The studies discussed above offer valuable insights into the use of nanoparticles in photothermal therapy and contribute to the advancement of this field.

2.5.2 Bioheat Transfer Equation

Mathematical models and numerical methods are indispensable for the development of efficient photothermal therapy protocols. These tools facilitate the comprehension and optimization of photothermal therapy by elucidating the heat transfer processes in biological tissues and projecting the temperature distribution during treatment. The bioheat transfer equation offers a spatial and temporal representation of the temperature in biological tissues and is rooted in the principles of heat transfer and diffusion. This equation incorporates the thermal conductivity, specific heat capacity, and blood perfusion rate of the tissue as well as the heat generation rate and optical properties of the light−absorbing material. The thermal behavior of the tissue can be characterized using the mathematical bioheat transfer formula commonly referred to as Penne's bioheat transfer equation:

$$\rho C_p \frac{\partial T}{\partial t} = \nabla(k\nabla T) + \rho_b C_b \omega_b (T_b - T) + Q_{met} + Q_{laser} \tag{2.4}$$

where T is the temperature, k is the tissue thermal conductivity [W/m · K], ρ is the tissue density [kg/m^3], C_p is the tissue−specific heat [J/(kg · K)], t is the time [s], ρ_b is the blood density [kg/m^3], C_b is the blood specific heat [J/(kg · K)], ω_b is the blood perfusion rate [1/s] and T_b is the arterial blood temperatures [K]. The terms Q_{met}, Q_{laser} are the metabolic heat generation rate [W/m^3] and the external laser source [W/m^3], respectively.

Recent studies have employed this equation to model the effect of nanoparticles on the temperature distribution and to develop a numerical modeling strategy for nanoparticle−assisted photothermal therapy. Through a computationally planned therapeutic approach, a study demonstrated that the intravenous administration of polyethylene glycol−protected gold nanorods resulted in the destruction of all irradiated tumors under NIR light [194]. More recent applications of the bioheat transfer equation have focused on modeling the use of gold nanorods [195] and nanoshells [192, 196] during photothermal therapy with nanoparticles. In a study conducted by Seung et al., a mathematical model utilizing COMSOL was developed to predict the temperature distribution of antibody−MWCNTs in response to laser irradiation of tumors [158]. The model was designed to ensure that a 4.5 W laser applied for 2 min would raise the tumor temperature above 45 °C while minimizing potential harm to adjacent tissues. Soni et al. simulated different GNP concentrations and provided valuable information on the optimal concentration of nanoparticles for effective photothermal therapy [197]. Another study developed a versatile numerical model capable of accounting for various relevant parameters, considering the homogeneous distribution of nanoparticles in embedded tissues [198]. In a separate study, a numerical modeling strategy was developed for nanoparticle−assisted photothermal therapy based on computed tomography (CT) imaging. The tumor geometry generated from the CT images was exported into a finite element simulation software using COMSOL Multiphysics modeling software for bioheat transfer simulation. The model was validated by comparing numerical calculations with experimental measurements [199].

The bioheat transfer equation is a valuable tool for understanding, predicting, and optimizing the temperature distribution in biological tissues during treatment, especially in the context of photothermal therapy involving nanoparticles. Additionally, the combination of the bioheat transfer equation with a Monte Carlo simulation has provided a new way to investigate the interaction between light and tissue.

2.5.3 Monte Carlo Simulation

Monte Carlo simulation is a widely utilized computational approach in the field of photothermal therapy, serving to predict the optical and thermal responses of tissues and nanoparticles. This technique employs random sampling to model the behavior of photons and their in-

teractions with biological tissues, considering tissue heterogeneity and anisotropy as factors that influence light and heat transport [31]. The radiative transport equation governs the interaction of photons with biological tissues and describes the transfer of energy as photons traverse a tissue [31]. Researchers commonly utilize an open−source Monte Carlo model, known as Monte Carlo for multilayered media (MCML), to calculate the required light dosage for photodynamic or photothermal therapy by simulating optical energy deposition within the tissue [200].

Numerous studies have employed Monte Carlo simulations in the realm of photothermal therapy to anticipate and monitor the temperature distribution within tumor tissues and adjacent healthy tissues. Recent research has demonstrated the utility of Monte Carlo simulations in exploring the photothermal consequences of liquid metal nanoparticles (LMNPs) in biological tissues subjected to near−infrared laser exposure. Simulation investigations have revealed that LMNPs expand the absorption of NIR lasers, leading to localized temperature elevation and improved temperature distribution. Specifically, the inclusion of LMNPs in biological tissues amplifies the absorption of the NIR laser, thereby potentiating the photothermal effects of the therapy [201]. In one study, indocyanine green (ICG) was administered to the tumor, and Monte Carlo simulation was used to predict the light and energy distributions within the tumor and surrounding healthy tissue [202].

Mathematical simulations have demonstrated the feasibility of monitoring tissue temperature during photothermal therapy. A temperature field simulation model was constructed based on Penne's bioheat equation using COMSOL Multiphysics. The model was used to compare the temperature of the tumor tissue with that of the surrounding healthy tissue during the laser and ICG treatments. In another study, Monte Carlo simulations and Beer's law were used to calculate the heat generation of tissues and gold nanoparticles irradiated by a laser for GNP−enhanced photothermal therapy [203]. The generated heat was used as a source term in the bioheat transfer equation in COMSOL to study the influence of various parameters [203]. A Monte Carlo simulation algorithm was developed to simulate photon propagation in a spherical tumor to calculate the laser energy absorption in the tumor and to examine the effects of the absorption and scattering coefficients of tumors on the generated heating pattern [204]. The simulated temperature elevations were compared with experimental measurements in previous *in vivo* studies on PC3 prostatic tumors [204].

Close monitoring of photothermal therapy is of paramount importance in achieving effective treatment outcomes while minimizing potential adverse effects. Preclinical planning is indispensable for determining the most appropriate thermal heating protocol for a particular type of cancer and specific tumors. Experimental research can offer invaluable insights into the optical properties and thermal behavior of tissues and nanoparticles, whereas computational modeling can aid in predicting the temperature distribution, measurement, and optimization of treatment parameters.

2.6 Conclusion

In conclusion, photothermal therapy has emerged as a promising and minimally invasive approach for cancer treatment, with several photothermal agents demonstrating significant potential in preclinical studies. However, further clinical trials are necessary to thoroughly evaluate the safety and efficacy of PTT in humans. Currently, clinical PTT relies on invasive 3D thermal imaging techniques; however, non−invasive thermometry methods, such as Raman spectroscopy, fluorescence, photoluminescence, and thermal imaging, hold promise for enhancing monitoring and control. Achieving precise spatiotemporal observation and control requires optimizing thermal heating through time−dependent protocols supported by simulations and modeling to plan outcomes. To improve photothermal agents, efforts should be focused on increasing the cross−sectional area of absorption and enhancing the photothermal conversion efficiency. Long−term biosafety, stability, and targeting capabilities are crucial for enhanced *in vivo* efficacy. The limited penetration depth of light into tissues can be overcome using longer−wavelength light sources or light−absorbing nanoparticles. Control of tissue temperature during treatment is necessary to prevent potential overheating and damage to adjacent healthy tissues. Despite the obstacles, the field of new nanomaterials and theragnostic techniques is progressing, offering a promising trajectory for improving the safety, efficacy, and accessibility of PTT in cancer treatment. With sustained research and development efforts, PTT holds great promise as a transformative approach to cancer therapy.

Transition to Next Chapter

Chapter 3[1] is built upon insights derived from the literature review to focus on exploring the potential advantages of MWCNTs for NIR photothermal cancer therapy. To enhance the light−to−heat conversion efficiency within the near−infrared biological transmission window, we decorate MWCNTs with plasmonic GNRs. Aligned with prior research, we evaluate the optical and thermal properties of MWCNTs−GNRs.

Utilizing advanced numerical simulations, alongside microscopic and spectroscopic characterization, we systematically unveil the intricacies of the hybrid nanomaterial. The results demonstrate a significant photothermal enhancement of hybrid MWCNTs−GNRs compared to bare MWCNTs, with a 4.9 enhancement factor per unit mass. *In vitro* investigations using prostate cancer cell lines confirm the potent ablation efficiency of MWCNTs−GNRs. These findings represent significant progress in developing novel hybrid plasmonic nanostructures for *in vitro* PTT, laying the groundwork for a new generation of photothermal therapy agents.

[1]The work presented in this chapter has been published in a peer−reviewed journal: **Fatma Oudjedi**, Seung Soo Lee, Miltiadis Paliouras, Mark Trifiro, and Andrew Kirk, “Enhancing *in vitro* photothermal therapy using plasmonic gold nanorod decorated multiwalled carbon nanotubes," Biomed. Opt. Express 14, 6629-6643 (2023)

Chapter 3

In Vitro Photothermal Therapy Using MWCNTs−GNRs

3.1 Introduction

Photothermal therapy is a noninvasive treatment modality that harnesses near−infrared laser irradiation and phototransducers to selectively eradicate malignant cells while preserving the integrity of surrounding healthy tissues [15]. This innovative approach offers several distinct advantages over conventional cancer treatments, including precise spatiotemporal selectivity for tumor sites, minimal invasiveness, and reduced adverse effects in treated individuals [18]. Therefore, PTT has emerged as a promising strategy for focal cancer therapy by leveraging the photothermal effect generated by light−absorbing materials.

Over the past few decades, extensive research has been devoted to investigating nanoparticles composed of diverse materials as potential photothermal transducers for photothermal cancer therapy [20]. These transducers must possess crucial characteristics, including strong absorption in the NIR region to enable efficient light−to−heat conversion and allow tissue penetration, the ability to accumulate at tumor sites, and biocompatibility [20, 33]. Recent advancements in nanoparticle−mediated photothermal therapy offer promising prospects for addressing this challenge by controlling nanoparticle concentration, size, structure, and dispersion within tumors [16]. While significant progress has been made in the development of

photothermal agents with various compositions and shapes, there remains an urgent demand for the development of novel photothermal transducers capable of localized heat generation at the cellular level [16, 18, 20].

Among the array of light−absorbing materials, carbon nanotubes have emerged as potential candidates for photothermal therapy owing to their favorable optical and thermal properties [80, 83, 84, 86, 91, 157]. In particular, multiwalled carbon nanotubes (MWCNTs) have garnered significant attention due to their distinctive optical properties and excellent biocompatibility [62, 63, 76, 88, 90]. However, MWCNTs display relatively low optical absorption in the first near−infrared biological therapeutic window (750−950 nm) [165, 205]. This wavelength range is over which biological tissues display low absorption, allowing light penetration through the skin and upper tissue layers to reach a target region [1]. Notably, nanoparticles incorporating plasmonic and carbon nanotube components have shown promise for simultaneously activating photoacoustic imaging and enhancing the efficiency of photothermal therapy [165]. Several research groups have developed various nanohybrid carbon−based structures using gold nanostars [141], spherical gold nanoparticles [137, 206, 207], covered gold layers on single−walled carbon nanotubes [140, 165], and silver nanoparticles [138], which combine localized heat generation and conversion in the near−infrared region. These methods contribute to real−time monitoring of treatment, thereby improving the efficacy and precision of nanoparticle−assisted thermal therapy. However, although gold nanorods possess tunable resonance properties, they have not yet been investigated as hybrid carbon−based nanostructures for PTT.

In this chapter, we propose a novel approach for PTT using GNR−decorated MWCNTs (MWCNTs−GNRs) to develop an enhanced photothermal agent. The decoration of MWCNTs with GNRs offers several advantages, including enhanced light absorption in the NIR region due to the localized surface plasmon resonance (LSPR) properties of the GNRs and the high thermal conductivity exhibited by MWCNTs, which plays a critical role in efficient heat distribution into the surrounding environment. By synthesizing plasmonic MWCNTs−GNRs as photothermal transducers, we can achieve superior local absorption and heat conversion compared to bare carbon nanotubes. These hybrid nanostructures demonstrate efficient thermal ablation of cancer cells, surpassing the reported performance of some carbon metal−based photothermal agents [138, 148]. We have introduced a new

metric, the hybrid enhancement factor, to better understand the influence of GNRs on the photothermal heating of GNRs−decorated carbon nanotubes. Additionally, *in vitro* experiments were conducted to evaluate the performance of the MWCNTs−GNRs as PTT agents for cancer therapy. To the best of our knowledge, this is the first report of covalently decorating MWCNTs with GNRs for the ablation of prostate cancer cells *in vitro*.

3.2 Methods

3.2.1 Materials and Reagents

Carboxylated multiwalled carbon nanotubes (MWCNTs), with dimensions of 20−30 nm in diameter and 0.5−2 μm in length, were purchased from Cheaptubes Inc. (Cambridgeport, VT, USA). 1−ethyl−3−(3−dimethyl aminopropyl) carbodiimide (EDC), sulfo−N−hydroxysulfo−succinimide (Sulfo−NHS), 2−(N−morpholino) ethanesulfonic acid (MES) were purchased from Sigma−Aldrich (Oakville, ON, Canada). Amine−functionalized gold nanorods (GNRs−TA), with a diameter of 5 nm and length of 21 nm, were supplied by NanoChemazone (Edmonton, AB, Canada).

3.2.2 Chemical Oxidation of MWCNTs

300 mg of MWCNTs were refluxed in 16 mL of 98% sulfuric and 70% nitric acid (3:1 v/v) mixture at 65 °C for 4 h in a sand bath under stirring conditions to further introduce carboxylic groups. At the end of the reaction, the oxidized MWCNTs (MWCNTs−COOH) were washed 3 times by ultracentrifugation at 21,000 rpm and resuspended in deionized water (d_2H_2O).

3.2.3 Preparation and Characterization of MWCNTs−GNRs

GNRs were covalently conjugated onto the surface of carboxylated MWCNTs using carbodiimide chemistry. Briefly, 1 mg/mL of MWCNTs−COOH was diluted to a final concentration of 0.1 mg/mL MWCNTs in 0.1 M MES buffer, pH 6. Carboxyl groups on the surface of the MWCNTs were activated by adding dropwise 10 mg/mL of EDC and 20 mg/mL of Sulfo−NHS to the MWCNT solution and were reacted at room temperature for 30 minutes.

The unreacted EDC/NHS was washed away by centrifugation for 10 minutes at 14,000 × g three times. Subsequently, 1 mL of GNRs−TA (100 μL of 50 OD GNRs diluted in 900 μL of d_2H_2O) was added to 1 mL of the solution and allowed to react at room temperature for 1 h. The final product (MWCNTs−GNRs) was washed by centrifugation at 14,000 × g at room temperature for 10 minutes and resuspended in 1 mL of d_2H_2O. The morphologies of MWCNTs−COOH and MWCNTs−GNRs were characterized using microscopic and spectroscopic tools. transmission electron microscopy (TEM) images were obtained using a Thermo Scientific Talos F200X G2S/TEM instrument operating at 200 kV. thermal gravimetric analysis (TGA) of as−received and as−prepared MWCNTs was carried out under reactive (air) media at a scan rate of 10 °C/min in the temperature range 30–800 °C using TGA Q500 V20.13 (TA Instruments). Zeta potential measurements of each tested sample were performed using dynamic light scattering (DLS) with ZetaPlus Particle sizing software V5.29 (Brookhaven Instrument Corp.), completing 10 runs. UV−Vis spectra were acquired using a Cary5000 UV−Vis−NIR spectrometer equipped with a 10 mm quartz cuvette, with a light path length of 1 cm and a scanned region ranging from 200 nm to 1200 nm. Raman spectra were measured with a WITec Confocal Raman microscopy system (WITec Alpha300R) equipped with a 633 nm HeNe laser with a 50X objective (maximum output power of 2 mW at a sample spot size of 3 μm in diameter and NA of 0.80).

3.2.4 Photothermal Irradiation

The photothermal effect of the MWCNTs−GNRs was tested under irradiation with an 808 nm continuous wave (CW) laser (LaserGlow, USA). The temperature of the solution was monitored using an infrared pyrometer sensor (Optris GmbH, Berlin, Germany) connected to an Arduino UNO board to collect the data. The CW laser with an output power of 0.5 W was collimated by a concave lens and placed 200 mm away from a 0.2 mL tube (MicroAmp Optical 8−tube strip, Thermo Fisher Scientific), resulting in a beam spot diameter of 5 mm, as shown in Fig. A.1. The power density of the continuous wave laser was 2 W/cm^2. Each sample within the tube contained 100 μL of the tested solution. The overall optical configuration aimed to maximize light absorption efficiency by the MWCNT−GNR hybrid nanostructures, thus facilitating effective photothermal conversion.

3.2.5 Cell Lines and Cell Cultures

PC3 [(PC−3; prostate adenocarcinoma; human (Homo sapiens)) cells were obtained from ATCC distributor Cedarlane (Burlington, ON, Canada). The cells were grown in a monolayer in RPMI−1640 supplemented with 10% fetal bovine serum (FBS) and 1% penicillin/streptomycin. Cell cultures were maintained in a humidified atmosphere containing 5% CO_2 at 37 °C and were regularly sub−cultured with 0.05% trypsin−EDTA once they had reached 80% confluency.

3.2.6 Cell Viability Evaluation

PC3 cells were grown in 96−well plates at a cell density of 1×10^5 cells/well and incubated in an atmosphere of 5% CO_2 at 37°C for 24 h. A 100 μL aliquot of MWCNTs−GNRs suspended in deionized water was added to the cells at final concentrations of 0, 0.3, 0.6, 10, 20, 40, 80, and 100 μg/mL, and the cells were further incubated for 24 h, 48 h, and 72 h, respectively. Following the incubation, 100μl of 5 mg/mL methyl thiazolyl tetrazolium (MTT) was added to each well and incubated for an additional 3 h. Finally, the medium was replaced with DMSO (100 μL) to dissolve the resulting formazan crystals. The absorbance was measured at 570 nm using a microplate reader (Bio−Rad UV−Vis Spectrometer). Cell viability of each concentration was assessed in triplicate and determined relative to untreated control cells. The relative cell viability was normalized to the control group and calculated using the following formula of cell viability growth: Cell viability (%) = (mean of absorbance of treatment group)/ (mean of absorbance of control group) × 100%.

3.2.7 *In Vitro* Photothermal Heating

PC3 cells were harvested and resuspended in a cell culture medium to achieve a concentration of 10,000 cells in 10 μL (equivalent to 1 million cells per mL). Subsequently, 10 μL of the different samples, including bare MWCNTs, GNRs, and MWCNTs−GNRs at various concentrations, were added to the cells. PC3 cells were incubated with the tested solutions in a PCR tube with a total volume of 20 μL. The resulting mixture was incubated for one hour. The mixture was gently pipetted in an upward and downward motion to ensure proper

dispersion and subsequently exposed to an 808 nm laser, with a power density of 2 W/cm^2 for 2 minutes. The cell viability was determined by automated Trypan blue cell counting using a CellDrop™Automated Cell Counter (DeNovix, Wilmington, DE, USA).

3.2.8 *In Vitro* Fluorescence Imaging

PC3 cells were treated with MWCNTs−GNRs at a concentration of approximately 1 OD. After 1 hour of incubation, the cells were irradiated with an 808 nm laser at a power of 2 W/cm^2 for 2 minutes. The cells were co−incubated with and without MWCNTs−GNRs for 24 h, which were assigned as MWCNTs−GNRs and blank groups (three samples were tested for each group). Cell death was assessed using the LIVE/DEAD Cell Imaging Kit (488/570), (Invitrogen #R37601), USA), according to the manufacturer's instructions. Finally, a fluorescence microscope (20X objective, EVOS FL Cell Imaging System, Thermo Fisher Scientific) was used to record the results.

3.2.9 Statistical Methods

All data are reported as the mean ± standard deviation from at least three independent runs. Statistical analysis was performed using Microsoft Excel 2010 and OriginPro2018. A two−paired t−test was performed on the relative cell viability under different experimental conditions. For all statistical analyses, a p−value < 0.05 was regarded as statistically significant.

3.3 Results

3.3.1 Functionalization and Characterization of MWCNTs−GNRs

To enhance the hydrophilicity of carboxylated multiwalled carbon nanotubes and enable subsequent covalent conjugation protocols, an acid reflux process was utilized to increase the formation of carboxyl group surfaces and subsequently used for EDC/NHS conjugation of the GNRs (Fig. 3.1a). TGA was employed to monitor the progress of the oxidation process, revealing a substantial change in weight loss at 580 °C (Fig. A.2a. The zeta potentials of

the MWCNTs intermediates and final products were continuously monitored throughout the conjugation process, revealing a decrease in the indicated charge exchange between the activated MWCNTs−COOH and MWCNTs−GNRs final product from −70 ±3 mV to −37 ±1 mV (Fig. A.2b and Table A.1).

TEM was employed to examine the morphological structure of MWCNTs−GNRs. Figure 3.1b exhibits a TEM image depicting the interface of the binding sites and conjugation of the GNRs on the MWCNTs. Notably, the TEM image demonstrated the absence of unbound GNR particles even after multiple cycles of washing and resuspension, providing strong evidence of the covalent attachment of GNRs onto the MWCNT surface (Fig. A.3a). Furthermore, statistical TEM analysis of the 120 GNRs revealed an average diameter and length of 11 ± 2 nm and 40 ± 9 nm, respectively, with an aspect ratio of 3.7, illustrating the polydispersity of the GNRs (Figs. A.3b–A.3d).

Raman scattering analysis was also conducted to characterize both the bare and decorated MWCNTs, as shown in Fig. 3.1c. Both samples exhibited three prominent Raman peaks: the D−band at 1336 cm^{-1}, associated with defects and the degree of disorder; the G−band at 1580 cm^{-1}, corresponding to the stretching vibration of carbon atoms in the honeycomb lattice structure; and the D' band at 1610 cm^{-1}, associated with the metallicity of the carbon nanotube. The decorated MWCNTs displayed enhanced Raman signals owing to the presence of the gold nanorods.

We also assessed and normalized the absorption spectra of MWCNTs−COOH and MWCNTs−GNRs (Fig. 3.2). The bare MWCNTs exhibit a resonance peak at approximately 250 nm, attributed to the π-π^* electron transition, akin to graphite [208]. In the case of the MWCNTs−GNRs, in addition to π−resonance, contributions from the transverse and longitudinal plasmonic responses of the GNRs were observed. The significant absorption in the near−infrared region indicates electromagnetic coupling between the gold nanoparticles and carbon nanotubes (Fig. A.5), which is particularly advantageous for photothermal heating conversion (Fig. 3.2a). Figure A.4 has been included as a supplementary graph to display the GNR prior to the covalent process.

Based on TEM micrograph statistical analysis, finite element modeling was employed to validate the optical response of the MWCNTs−GNRs. The absorption spectra were theoretically calculated using the finite element method in COMSOL Multiphysics (see Ap-

pendix A.5). The MWCNTs were modeled as cylinders with dimensions of 200 nm in length and 30 nm in diameter, due to the computationally demanding nature of the simulations. Similarly, the nanorods were modeled as cylinders with hemispherical end caps, having dimensions of 11 nm in diameter and 40 nm in length, based on statistical TEM analysis (Fig. 3.2b). Numerical validation confirmed the presence of a $\pi-$resonance peak in the ultraviolet spectrum, along with longitudinal and transverse responses in the near−infrared region (Figs. 3.2c and 3.2d). The normalized electromagnetic field extracted for longitudinal resonances exhibited pronounced hotspots at the binding sites, as shown in Fig. 3.2e. Notably, an observed disparity emerged between the experimental near−infrared absorption resonance and the numerically calculated outcomes, which is likely attributed to the polydisperse nature of the gold nanorods (Fig. 3.2f). Scattering far−field simulations were conducted to ascertain the scattering or absorption behavior of the hybrid structure at near−infrared wavelengths relative to the transverse and $\pi-$resonances, unequivocally verifying the strong absorption at 808 nm (Figs. A.6a and A.6b). Considering these spectral and optical characterizations, which confirmed the successful covalent conjugation of amine−functionalized GNRs onto carboxylated MWCNTs via carbodiimide chemistry, we evaluated the photothermal performance of the hybrid structure in the near−infrared region.

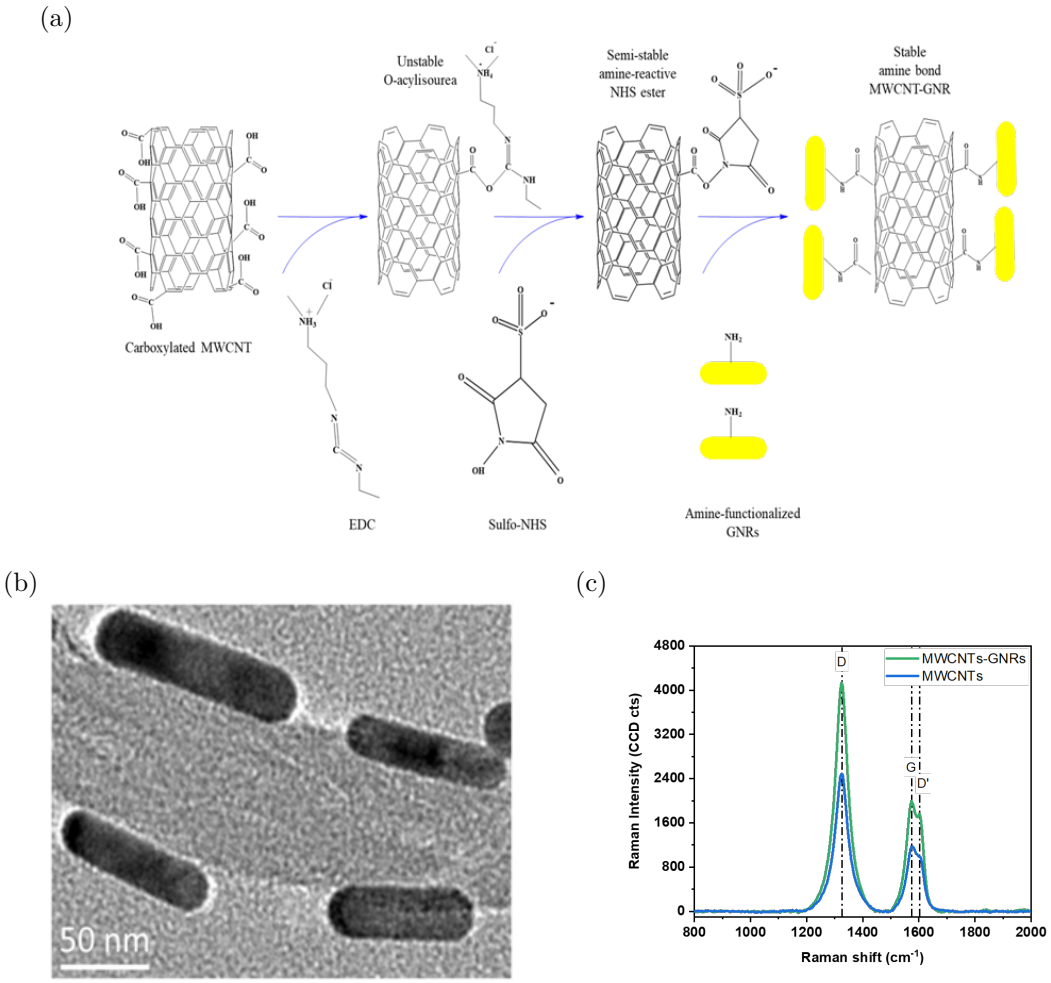

Fig. 3.1. Preparation and characterization of MWCNTs−GNRs. (a) The schematics for covalent conjugation of amine−functionalized GNRs onto carboxylated MWCNTs. (b) TEM image of MWCNTs−GNRs at a scale of 50 nm. (c) Raman spectra of carboxylated (blue curve) and decorated (green curve) MWCNTs, with the carbon peak bands comprising G−band (1580 cm^{-1}), D−band (1336 cm^{-1}), and D' (1610 cm^{-1}).

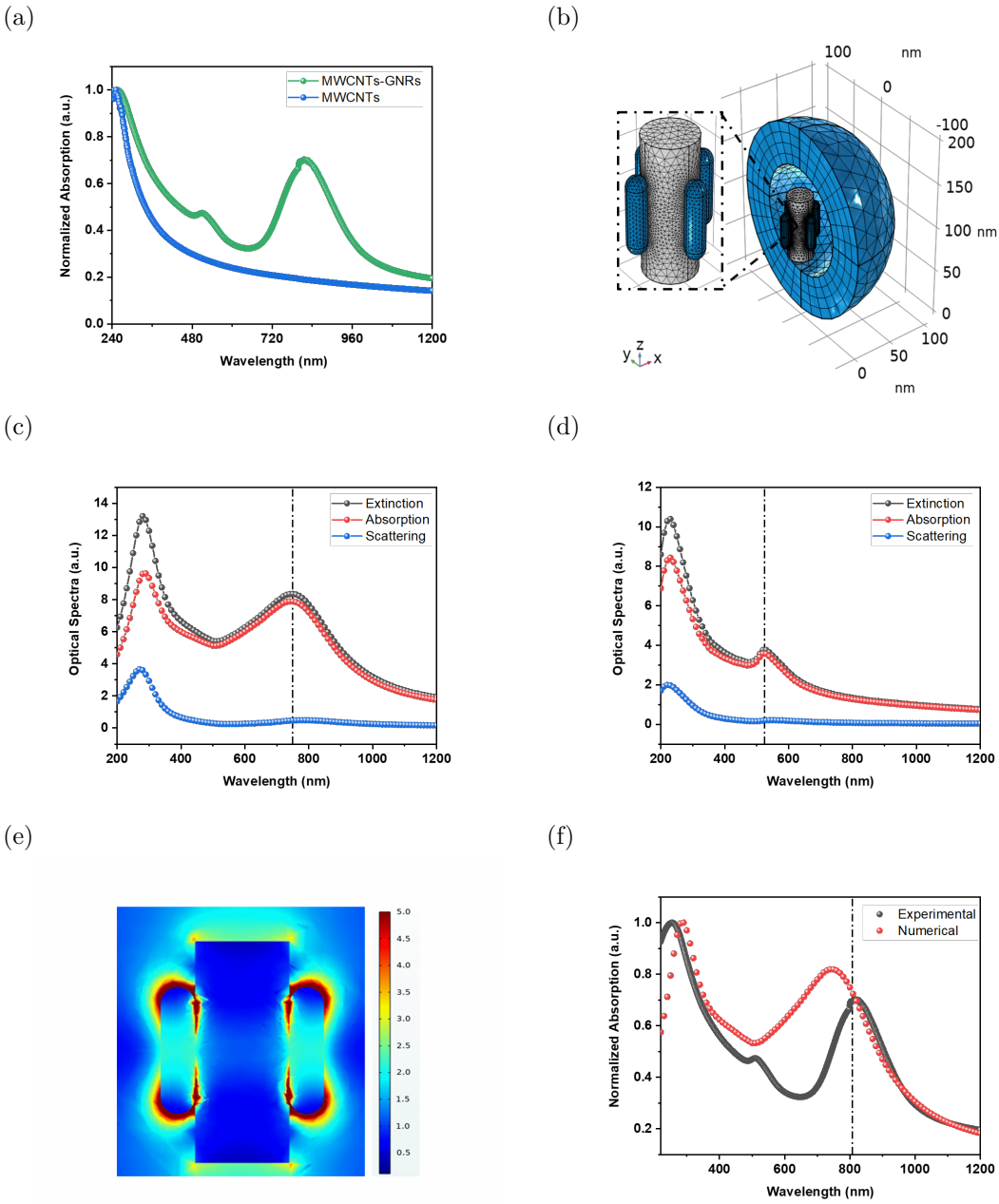

Fig. 3.2. Characterization of the absorption properties of MWCNTs−GNRs. (a) Normalized absorption spectra comparing carboxylated MWCNTs (blue curve) and MWCNTs−GNRs (green curve). (b) Three−dimensional meshing of decorated MWCNTs based on the TEM images Fig. 3.1b, inset of MWCNTs−GNRs structure. (c) Simulated optical spectra of longitudinal and (d) transverse resonance of MWCNTs−GNRs. (e) Normalized electromagnetic field of the longitudinal resonance of MWCNTs−GNRs. (f) Normalized absorption spectra of the experimental and numerical MWCNTs−GNRs.

3.3.2 Near−Infrared Photothermal Performance and Stability of MWCNTs−GNRs

We conducted a series of investigations under various conditions to comprehensively assess the photothermal performance of the MWCNTs−GNRs. Initially, we prepared a stock of MWCNTs−GNRs with an optical density of 1.8, as determined by UV−Vis measurements. We set the as−prepared MWCNTs−GNRs to an approximate concentration of 1 OD, by diluting from its initial concentration of 1.8 OD. Serial dilutions, from 1 to 1/16 of the stock MWCNTs−GNRs, were prepared with a 1:2 ratio. The diluted samples were subjected to laser exposure for 300 seconds at a power density of 2 W/cm^2 with a continuous wave 808 nm laser. As anticipated, the temperature of the diluted samples exhibited a noticeable increase ranging from 30 to 55 °C relative to the initial room temperature of 22 °C, whereas the control sample of water exhibited a temperature increase of 23 °C, as shown in Fig. 3.3a. This finding suggests that the primary mechanism responsible for generating heat is the plasmonic properties of the MWCNTs−GNRs which capture light and convert it into thermal energy. This process appears to be distinct from the direct heating of water caused by laser irradiation. The heating rate was determined at different optical densities, revealing a linear relationship among the dilutions, with a calculated temperature increase of approximately 15 °C/min (Fig. 3.3b).

To evaluate the stability of the synthesized MWCNTs−GNRs, we conducted four cycles of laser irradiation, followed by absorbance measurements after each irradiation. The first cycle served as the control, and subsequent cycles were compared to the baseline. Over repeated exposure, we did not observe any decay in the temperature, as displayed in Fig. 3.3c. The UV−Vis spectra of each irradiated sample, along with their respective cycles, also exhibited negligible changes in absorption at 808 nm, demonstrating the excellent photothermal stability of the MWCNTs−GNRs over multiple irradiations, as shown in Fig. 3.3d. Finally, the change in temperature of the MWCNTs−GNRs was evaluated at different power densities of continuous−wave laser irradiation over time, as shown in Fig. 3.3e. These results suggest that our hybrid plasmonic MWCNTs can generate heat, even at low irradiation dosages.

Furthermore, the photothermal effect of the MWCNTs−GNRs was compared to different samples, including the unmodified MWCNTs, GNRs, and d_2H_2O. First, the changes in

temperature of each sample upon laser irradiation were measured during a 300−second heating phase, followed by a 300−second cooling phase, as shown in Fig. 3.4a. The temperature decay over time was analyzed by calculating the natural logarithm of the temperature decay (see Appendix A.6) [55]. By fitting the resulting curve, the average thermal equilibration time constant associated with the radiative heat transfer was determined to be 149.14 seconds, as shown in Fig. 3.4b. Using this value and Eq. (A.3) to Eq. (A.14), the photothermal conversion efficiency of the MWCNTs−GNRs was calculated to be 69%. This calculation facilitated the assessment of the figure of merit, serving as a measure of the heating efficiency of each sample, also known as the photothermal conversion efficiency. The photothermal conversion efficiency serves as a quantitative measure of the effectiveness with which the incident power is converted into heat by nanoparticles within their surrounding medium, thereby determining the achieved heating efficiency (Table A.2). The decorated multiwalled carbon nanotubes exhibited a significant enhancement of 69% in photothermal conversion efficiency compared to the individual components of MWCNTs and GNRs alone, approximately 29% and 35%, respectively, as shown in Fig. A.7a. Moreover, the heating rates of the examined samples were derived from the 300−second heating phase (depicted in Fig. 3.4a) and are illustrated in Fig. A.7b, unequivocally establishing the superior heating rate of MWCNTs−GNRs.

The photothermal conversion efficiency per unit mass of MWCNT is another figure of merit used to evaluate the hybrid nanostructure. This measure involves dividing the photothermal conversion efficiency by the mass of MWCNT present in each sample solution. The resulting value indicates the efficiency of the photothermal conversion with respect to the mass of MWCNT employed in the near−infrared region (see Appendix A.7 for detailed calculations), as shown in Fig. 3.4c. The photothermal conversion efficiency per unit mass of MWCNTs−GNRs was approximately 4.9 times greater than that of bare MWCNTs, indicating a significant contribution of GNRs to the enhancement of MWCNTs through their electromagnetic coupling in the near−infrared region. Consequently, the MWCNTs−GNRs displayed excellent photothermal performance, indicating their potential as PTT agents.

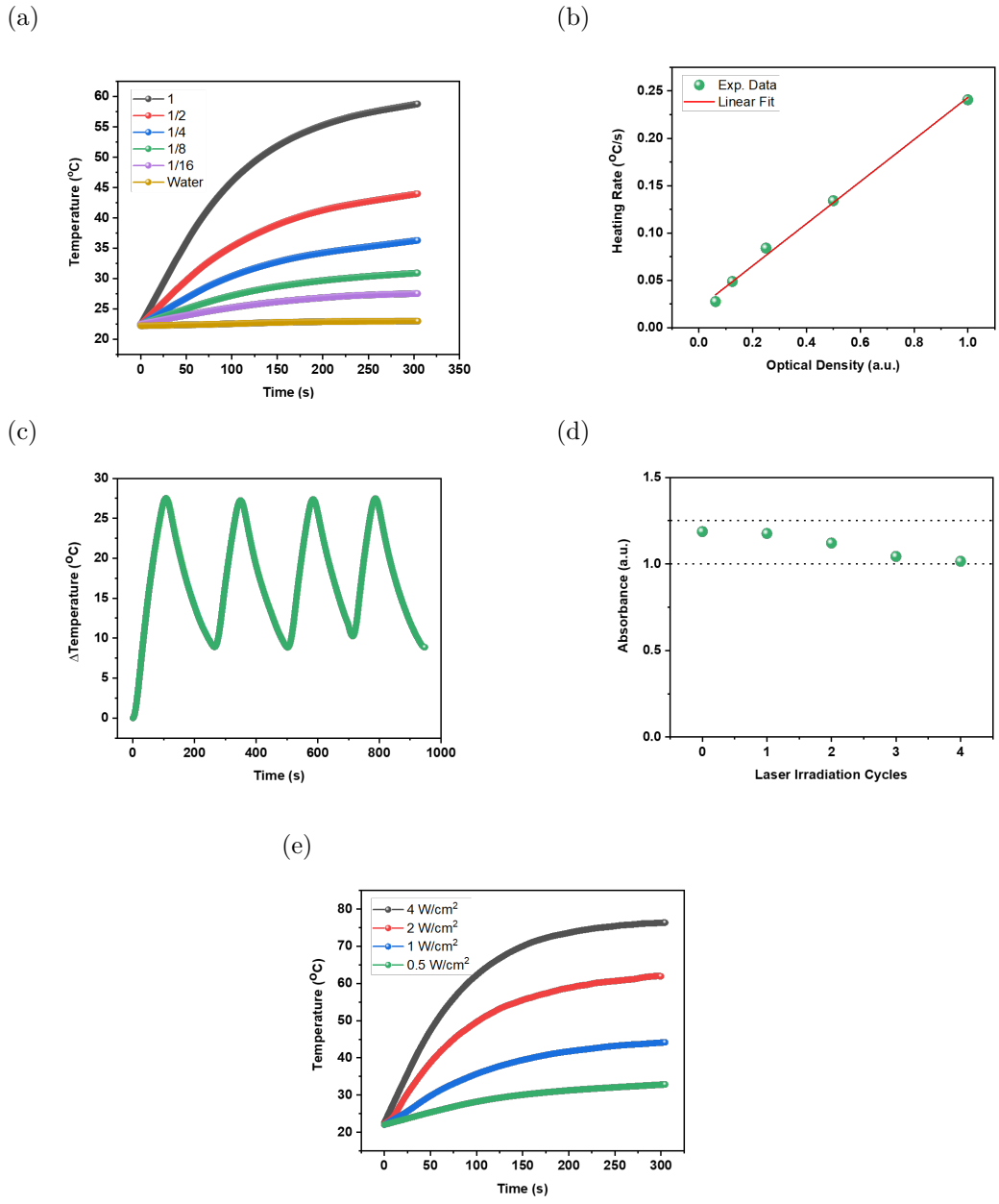

Fig. 3.3. Photothermal properties and stability of MWCNTs−GNRs. (a) Temperature profiles of MWCNTs−GNRs at various optical densities, starting from the as−prepared state with an optical density of approximately 1 at 808 nm. The samples were subjected to laser irradiation for 300 seconds at 2 W/cm^2, with subsequent half−dilutions down to 1/16 of the original concentration. (b) Increasing trend in heating rate as a function of optical density for MWCNTs−GNRs. (c) Thermal curves and changes in absorption intensity of MWCNTs−GNRs after repeated on and off cycles of 808 nm laser irradiation (n = 3) at 2 W/cm^2. (d) Absorbance at 808 nm of MWCNTs−GNRs after each repeated on−and−off laser heating cycle. (e) Temperature profiles of MWCNTs−GNRs under different laser power densities during 300 seconds of heating at 2 W/cm^2.

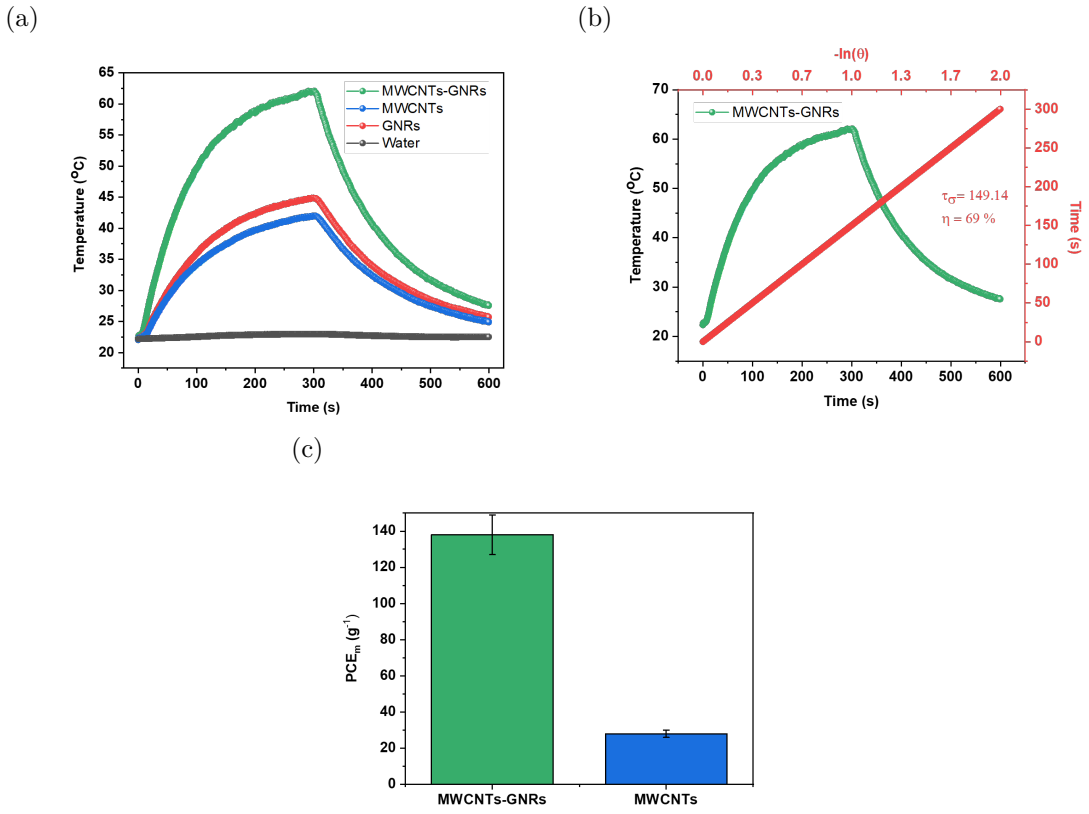

Fig. 3.4. Photothermal performance of MWCNTs−GNRs. (a) Temperature profile of deionized water (black curve), GNRs (red curve), MWCNTs (blue curve), and MWCNTs−GNRs (green curve) under 808 nm continuous wave laser irradiation for 300 seconds of heating and 300 seconds of cooling at 2 W/cm^2. (b) Photothermal effect of as−prepared MWCNTs−GNRs (optical density of approximately 1 at 808 nm) when irradiated with an 808 nm continuous wave laser at 2 W/cm^2 for 300 seconds, followed by a 300−second cooling period. The left y−axis represents the temperature during the process, while the right y−axis shows the linear correlation between cooling time and the negative natural logarithm of the cooling temperature. (c) Photothermal conversion efficiency as per mass of bare (blue bar) and decorated MWCNTs (green bar) samples investigated under 808 nm continuous wave laser irradiation at 2 W/cm^2, with 300 seconds of heating and 300 seconds of cooling.

3.3.3 *In Vitro* Cytotoxicity and Photothermal Performance MWCNTs−GNRs

Considering the thermal effects and exceptional stability of MWCNTs−GNRs, their cytotoxicity, and *in vitro* phototherapy ablation properties were investigated in PC3 human prostate cancer cells. The relative viability of PC3 cells exposed to various concentrations of MWCNTs−GNRs for 24 h, 48 h, and 72 h was determined using the MTT assay. As expected, no significant cytotoxicity was observed, as the cell viability remained high at approximately 80%, even at the highest concentration of MWCNTs−GNRs (up to 100 μg/ml), as shown in Fig. A.8a. These findings demonstrate the non−toxic nature of MWCNTs−GNRs towards PC3 cells at the tested concentrations, supporting their potential for *in vivo* photothermal therapy and warranting further exploration of their biological applications. Furthermore, the photothermal ability of MWCNTs−GNRs to induce cell death in PC3 cancer cells was investigated. PC3 cells were incubated with decorated MWCNTs for 1 h and exposed to an 808 nm laser (2 W/cm^2) for increasing durations (0, 7.5, 15, 30, 60, and 120 s). Cell viability was quantitatively assessed using Trypan blue staining, which revealed a time−dependent photothermal therapy effect (Fig. A.8b). The temperature was monitored during each exposure period, and the amount of energy delivered to the sample was calculated relative to the relative cell viability of PC3 cells, as shown in Fig. 3.5a. Increased energy delivery resulted in greater thermal ablation of PC3 cells, whereas PC3 cells without laser irradiation remained unaffected.

PC3 cells were incubated with GNRs, MWCNTs, and MWCNTs−GNRs, followed by thermal irradiation at 2 W/cm^2 for 120 s (Fig. 3.5b). The survival rate of cells incubated with MWCNTs−GNRs was only 20% compared to the controls (GNRs and MWCNTs). Fluorescence imaging of PC3 cells co−stained with Calcein AM (green fluorescence indicating live cells) and BOBO−3 Iodide (red fluorescence indicating dead cells) further supported these results. After 120 s of laser exposure at 2 W/cm^2 and an additional 24−hour incubation period, the MWCNTs−GNRs group displayed significant cell ablation and the presence of numerous cell debris floating in the cell culture medium, indicating their potent photothermal properties, as shown in Fig. 3.5c. These fluorescence staining results are consistent with those of the cell viability tests, demonstrating the ability of MWCNTs−GNRs to efficiently

absorb laser energy in the vicinity of PC3 cells and convert it into heat, leading to immediate cell death. The minimal damage observed in the control group treated with only the NIR laser confirmed the specificity of the photothermal effect. Additionally, the untreated groups incubated with PC3 cells for 24 h exhibited negligible cell damage (Fig. A.9). Based on these results, the suitability and potential of the as−prepared MWCNTs−GNRs as highly effective and efficient *in vitro* PTT agents are confirmed.

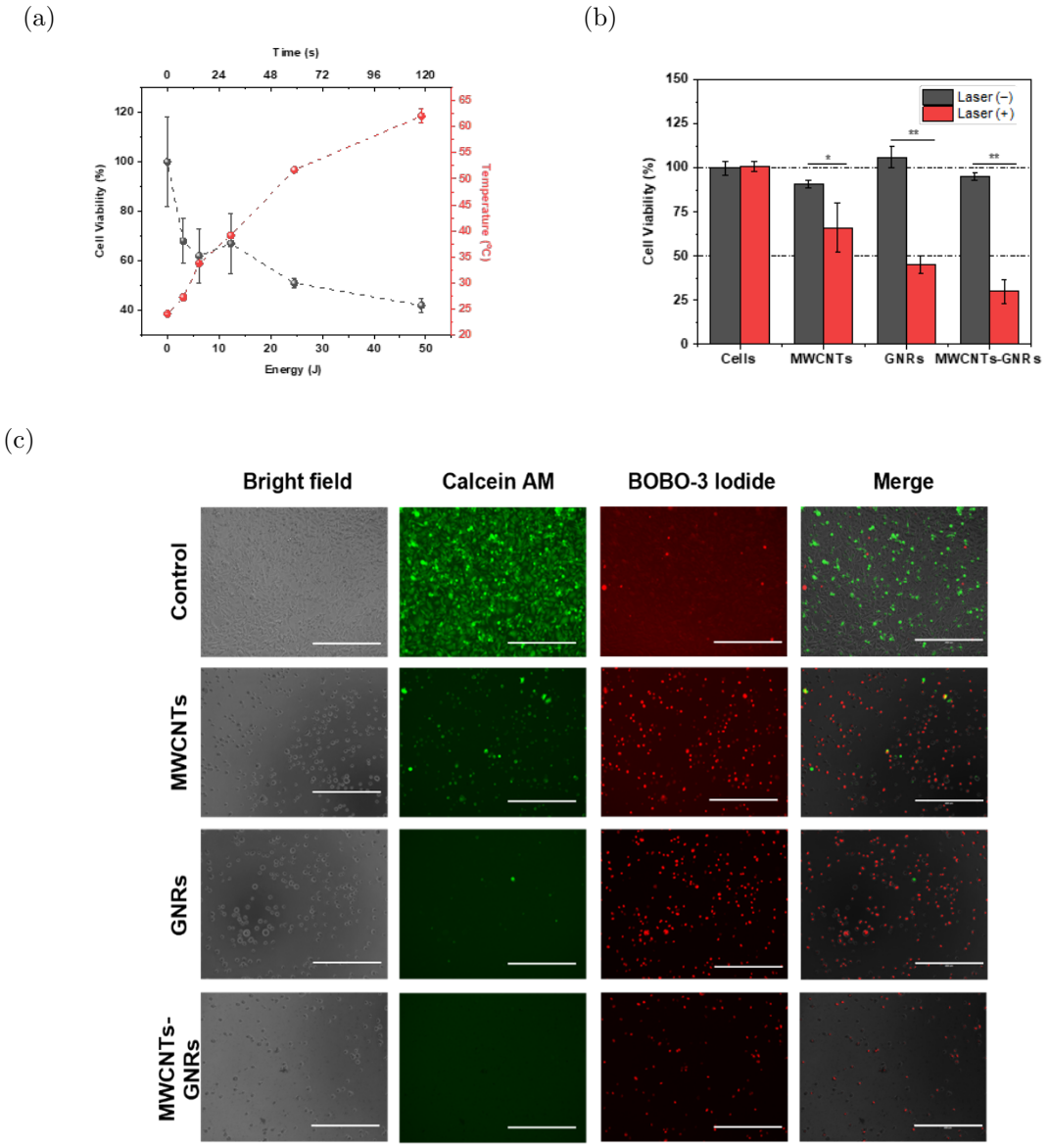

Fig. 3.5. *In vitro* Photoablative outcomes of MWCNTs−GNRs. (a) Relative viability of PC3 cells incubated with MWCNTs−GNRs and exposed to 808 nm laser irradiation at 2 W/cm^2 for varying durations of irradiation (energy). The right y−axis represents the recorded final temperature at different time points of irradiation. (b) Relative cell viability of exposed (red bar, +laser) and unexposed (black bar, −laser) PC3 cells incubated with MWCNTs, GNRs, MWCNTs−GNRs and exposed at 2 W/cm^2 for 120 s. A two−paired student t−test was used to evaluate the statistical significance; p−value for * = $p < 0.05$ and ** = $p<0.01$, respectively. (c) Fluorescence images captured after 808 nm laser irradiation 2 W/cm^2 for 120 s. The images depict the fluorescence of Calcein AM (green fluorescence indicating live cells) and BOBO−3 Iodide (red fluorescence indicating dead cells). Scale bars correspond to 400 μm.

3.4 Discussion

Noble metal nanoparticles attached to carbon nanotubes have attracted considerable interest in recent years owing to their distinct characteristics such as expansive surface area, exceptional thermal conductivity, and tunable optical properties. These composite materials exhibit remarkable promise across a range of fields including sensing [133–135], photocatalysis [136, 137], and photothermal therapy [138–141, 209]. The enhanced photothermal conversion efficiency of the resulting MWCNTs−GNRs hybrid can be attributed to several factors. Firstly, the high surface area of MWCNTs facilitates the attachment of GNRs, enhancing the absorption of NIR light and leading to a higher concentration of heat−generating agents [143–145]. Secondly, the MWCNTs served as a scaffold to prevent GNR aggregation and improve their stability in solution.

We successfully synthesized a novel and stable structure that efficiently converted light into heat, thereby enhancing the photothermal effects within the near−infrared biological window. The effectiveness of enhancing the photothermal effect of multiwalled carbon nanotubes within the NIR biological window, specifically at a wavelength of 808 nm, has been verified through the formation of a hybrid plasmonic carbon nanostructure. This structure was achieved using GNR−decorated MWCNTs, thus, validating the viability of this promising strategy. This approach capitalizes on the unique optical plasmonic properties of GNRs, which efficiently absorb near−infrared light and convert it into heat, thereby enabling thermal damage to cancer cells. In considering the low scattering properties observed in our study, it is important to note that the hybrid plasmonic carbon nanostructure, comprised of gold nanorod−decorated MWCNTs, exhibits characteristics that contribute to reduced scattering. The localized surface plasmon resonance of the GNRs, particularly in the NIR region, is known to enhance light absorption and convert it into heat efficiently. The strong absorption by the GNRs minimizes the scattering of incident light, directing more energy towards the photothermal conversion process. While low scattering may limit the distribution of heat, it ensures that a significant portion of incident energy is utilized for the intended therapeutic effect. However, further studies on the trade−off between scattering and absorption are needed to better elucidate the relationship.

Our research also demonstrates that this structure exhibits non−cytotoxic behavior over an

extended period of several days and effectively ablates cancer cells over time when irradiated with a NIR laser. Additionally, the photothermal conversion performance of our plasmonic hybrid structure was calculated to be 69%, surpassing the reported performance of some other recently published carbon−metal−based photothermal therapy agents (Table A.4). However, it is essential to acknowledge that direct comparisons with studies using lower laser power densities should be made cautiously, as the therapeutic outcomes are impacted by multiple factors. These factors include the properties of the nanomaterial, the experimental conditions, the type of cancer targeted, and the specific biological context in which the treatment is administered, whether it is conducted *in vivo* or *in vitro*.

One of the challenges encountered was accurately determining the amount of gold attached to the carbon nanotube surface (see Appendix A.11 for detailed calculations). This can be estimated using Gan's theory [210] or determined using spectroscopic tools, such as inductively coupled plasma mass spectrometry [141], energy−dispersive X−ray spectroscopy [206, 211], or mathematical modeling based on adsorption kinetics [212]. Also, polydisperse gold nanorods pose challenges in terms of their optical spectra because their size and shape variations lead to broadened absorption and scattering peaks, making it difficult to achieve precise tuning of plasmonic properties. Additionally, the functionalization of polydisperse gold nanorods with other components is challenging owing to the heterogeneity of the surface characteristics, impeding the control and uniformity of the attachment process. To address this challenge, a potential strategy is to synthesize gold nanorods with precise control over their size and shape onto the surface of carbon nanotubes [137, 206, 213]. Moreover, MWCNTs−GNRs lacked targeting moieties, such as antibodies [214], peptides [215], or aptamers [142], which poses challenges in achieving precise photothermal treatment due to the lack of selectivity towards cancer cells. Furthermore, conducting *in vitro* experiments with suspended cells exposed to a solution of nanoparticles presents a simplified model that may not fully represent the complex tumor microenvironment found *in vivo*. Validation of the selectivity and safety of MWCNTs−GNRs in a complex physiological environment necessitates *in vivo* studies, emphasizing the necessity of assessing their impact on healthy cells to ensure safety and translational viability. Addressing potential toxicity concerns, modifications to MWCNTs involve shortening length, reducing diameter, and functionalizing with carboxylic acids [21]. Previous investigations into the safety profiles of MWCNTs [216] and gold nanorods [174]

have been conducted. Additionally, future emphasis will be on utilizing PEGylation of nanoparticles to enhance biocompatibility and minimize potential toxicity, aligning with established methodologies to improve the safety profile of nanomaterials. This underscores the translational potential of plasmonic−decorated multiwalled carbon nanotubes in cancer therapy.

Building upon these findings, our forthcoming research endeavors will focus on investigating the optical properties of MWCNTs−GNRs that are functionalized with biologically targeted entities, with the specific objective of advancing targeted cancer therapy, particularly in the domain of prostate cancer treatment. Notably, this investigation aligns with an ongoing human clinical trial involving a gold−based nanostructure, further emphasizing the significance of our proposed studies in this field [21]. Additionally, our approach can be readily extended to incorporate other applications such as imaging [148, 165, 216], drug delivery [161, 171, 174, 217, 218], and Raman temperature probes [175, 179, 182], enabling dual therapeutic synergy for precise cancer therapy. Furthermore, we propose the conjugation of alternative plasmonic materials, such as titanium nitride nanoparticles [219–222], which can span both the first and second biological windows, thereby expanding the range of therapeutic applications. Overall, the hybrid plasmonic carbon nanostructure holds great promise in this field, demonstrating improved efficiency and efficacy for cancer cell ablation within the near−infrared biological window.

3.5 Conclusion

In this chapter, we successfully optimized the optical absorption properties of multiwalled carbon nanotubes for photothermal therapy by incorporating plasmonic gold nanorods. The decoration of MWCNTs with GNRs resulted in enhanced light absorption in the first near−infrared region, harnessing the localized surface plasmon resonance of the GNRs. The comparative analysis demonstrated that the hybrid MWCNT−GNR nanostructure exhibited significantly higher local absorption and heat conversion efficiency than either bare carbon nanotubes or plasmonic gold nanorods. As a result, this enhanced performance enabled efficient thermal ablation of cancer cells, achieving hyperthermia temperatures within a short period. These findings present new opportunities for developing hybrid plasmonic

photothermal transducers in cancer therapy but also hold great promise for a wide range of biomedical applications, including combined targeted therapy, drug delivery, and theragnosis.

Transition to Next Chapter

Distinguished by non−contact measurement, high spatial resolution, and rapid response times, Raman thermometry is a widely applied technique for temperature measurement through Raman spectroscopy. Its active utilization extends to various fields, including materials science, pharmaceutical research, and thermal characterization of biological systems, establishing it as an essential tool for materials and structures analysis.

Chapter 4[1] serves as a vital link between our exploration of anti−Stokes Raman thermometry and its application in targeted photothermal therapies for cancer. Our focus centered on *in situ* cellular temperature measurements, a critical determinant in the efficacy of photothermal treatments. Using gold nanorods−decorated multiwalled carbon nanotubes (MWCNTs−GNRs) as nanothermometer probes, we delved into the intricacies of Raman spectra analysis at various powers and initial temperatures. These responsive spectra changes paved the way for a reliable Raman thermometry methodology, enabling the extraction of the intrinsic photothermal heating coefficient of MWCNTs−GNRs and providing essential insights into their thermometric properties.

Our investigation extended to evaluating MWCNTs−GNRs with prostate cancer cell lines, assessing *in situ* cellular temperatures, and generating temperature maps for a selected area. This chapter not only explores the reliability of our temperature measurements through data standard error analysis but also offers a nuanced understanding of the accuracy of our results. The correlation of obtained temperatures with cell viability outcomes at varying laser powers adds depth to our findings. Importantly, our investigation spanned a temperature range from 60 to 100 °C, surpassing the critical threshold of 50 °C associated with inducing cell demise. In essence, this chapter establishes a comprehensive foundation for the subsequent exploration of MWCNTs−GNRs as potent nanothermometer probes for targeted and effective photothermal cancer therapies.

[1]The work presented in this chapter has been submitted for review in a peer−reviewed journal: **Fatma Oudjedi**, Seung Soo Lee, Miltiadis Paliouras, Mark Trifiro, Sebastian Wachsmann-Hogiu, and Andrew Kirk, "*In vitro* Raman thermometry using gold nanorod−decorated carbon nanotubes", *submitted manuscript.*

Chapter 4

In vitro Raman Thermometry Using MWCNTs−GNRs

4.1 Introduction

Nanoscale heating has emerged as a promising therapeutic process; however, precise temperature measurement at the cellular level remains a significant challenge [223]. In the realm of photothermal cancer therapy, it is essential to accurately determine the local temperatures at the cellular level. This is critical to ensure that the focal temperatures reach the therapeutic level required for effective tumor ablation, while also minimizing the risk of unintended damage to adjacent non−cancerous tissues [15]. The fundamental concept of photothermal therapy involves the utilization of near−infrared light and photothermal agents, such as plasmonic nanoparticles. These agents absorb laser energy, converting it into heat, ultimately inducing cell death [20]. The effectiveness of photothermal treatment depends on both the duration of irradiation and tissue temperature. An imbalance between the light dose and exposure duration can result in temperatures falling outside the therapeutic range [15, 20]. Despite numerous efforts by research groups, the challenges in precisely assessing cellular temperatures underscore the need for advanced and reliable nanothermometry techniques to enhance the safety and efficacy of photothermal therapies [224]. Over the past decades, researchers have proposed various approaches to address the gap in nanoscale thermometry [225]. Commonly

employed techniques include conventional infrared thermography, thermocouples, scanning thermal microscopy [226], variation in refractive index [227], magnetic resonance thermometry [228], and fluorescence thermometry [229–231]. However, these methods have drawbacks such as photobleaching, photosensitivity, and optical diffraction limits, preventing them from achieving a high spectral resolution and requiring high environmental maintenance [232].

Raman spectroscopy has emerged as a promising solution, providing detailed chemical and structural insights into biological samples [233–235]. This label−free, non−invasive, and contactless technique enables *in vitro* biological investigations [236, 237]. Anti−Stokes Raman thermometry, a rapidly growing field in spectroscopy, offers a promising solution for measuring cellular−level temperatures [179]. Recent advances in nanoprobe Raman thermometry have enabled the measurement of intracellular temperature [180–182]. Other groups have utilized probe molecules on gold surfaces to measure nanoparticle temperatures [183–185]. In accordance with Boltzmann statistics, this method involves analyzing Stokes and anti−Stokes Raman spectra to determine temperature and optimize treatment [179, 238]. Stokes Raman scattering occurs when irradiated molecules are in vibrational states, while anti−Stokes scattering occurs when the initial state is an excited vibrational state. At room temperature, anti−Stokes signals are weak due to a low population of excited states [177, 238]. As temperature increases the excited states become more populated, strengthening anti−Stokes signals. Inelastic scattering phenomena describe the transfer of energy from photons to virtual states and the resulting loss (Stokes) or gain (anti−Stokes) [177, 238]. The ratio between the strengths of Stokes and anti−Stokes signals within a specific Raman band becomes a highly reliable indicator of temperature−dependent modifications of the molecule, making Raman thermometry a necessary technique for monitoring cellular damage [238, 239].

This chapter explores the application of gold nanorods−decorated multiwalled carbon nanotubes (MWCNTs−GNRs) as innovative probe nanothermometers within the context of photothermal cancer therapy. The determination of material temperature using Raman spectroscopy relies on primary methods, specifically the ratio of Stokes to anti−Stokes signal strength within a specific Raman band. The application of our previously described MWCNTs−GNRs nanoformulation [158] provides a unique combination where simultaneously harnessing the high thermal conductivity and the symmetric G peak in the Raman spectrum of MWCNTs, as ideal candidates for precise temperature measurement [240, 241]. Moreover,

the incorporation of plasmonic gold nanorods into multiwalled carbon nanotubes enhances optical absorption for photothermal therapy [158]. This nanoformulation results in increased efficiency in the thermal ablation of cancer cells and a rapid elevation of hyperthermia temperatures [158]. Furthermore, the addition of gold nanorods not only enhances optical absorption but also amplifies Raman scattering signals, enabling *in situ* temperature measurement at the cellular level [180]. Incorporating gold nanorods transforms MWCNTs−GNRs into label−free temperature probes, thereby providing a spontaneous and self−referencing approach without needing external Raman probe molecules. Furthermore, this technique enables the identification of essential power density thresholds and temperature limits needed for ensuring cell death.

We evaluated the feasibility of MWCNTs−GNRs as nanoscale temperature probes and characterized their intrinsic photothermal heating properties. We provided a detailed analysis of the temperature distribution through Raman mapping over selected areas. Additionally, we investigated single live cells with MWCNTs−GNRs as theragnostic probes for *in vitro* temperature rise, introducing a novel method for measuring *in situ* cell temperature. By monitoring the anti−Stokes and Stokes signals of the G peak at various laser powers, we found that MWCNTs−GNRs can efficiently heat cancer cells and act as non−invasive temperature probes for *in situ* monitoring.

4.2 Methods

4.2.1 Preparation of GNRs Decorated MWCNTs

Multiwalled carbon nanotubes, acquired from Cheaptubes Inc (Cambridgeport, VT, USA), were subjected to chemical oxidation through refluxing in an acid mixture, followed by thorough washing and suspension in deionized water. Amine−functionalized gold nanorods (GNRs−NH_2), provided by Nanopartz (Loveland, CO, USA), were covalently linked to the carboxylated MWCNTs utilizing carbodiimide chemistry. Activation of carboxyl groups on the MWCNTs' surface facilitated the covalent attachment of GNRs−NH_2. The resulting compound was purified via centrifugation and subsequent suspension in deionized water, for a final concentration of 1 optical density (OD). The comprehensive preparation and

characterization procedures for the MWCNTs−GNRs outlined in this chapter, are detailed in our previously published work and can be referred to for in−depth information on the characterization techniques and methodology employed [158].

4.2.2 Cell Culture

PC3 cells [PC−3; prostate adenocarcinoma; human (Homo sapiens)] were purchased from the ATCC distributor Cedarlane (Burlington, ON, Canada). The cells were cultivated as a monolayer in RPMI−1640 medium supplemented with 10% fetal bovine serum (FBS) and 1% penicillin/streptomycin. The cell cultures were meticulously maintained in a humidified atmosphere containing 5% CO_2 at 37 °C. Regular sub−culturing was performed using 0.05% trypsin−EDTA once the cells had achieved 80% confluency.

4.2.3 Raman Experimental Setup

Raman spectra were acquired using a WITec Alpha300Rm confocal Raman microscopy system (WITec GmbH, Ulm, Germany) equipped with a 633 nm HeNe laser (HNL 150LB, Thorlabs, New Jersey, USA) and two objectives: a 50X air objective (Nikon, NA = 0.80) and a 100X oil objective (Olympus, PlanApo, NA = 1.4) with a spatial resolution of 300 nm in the focal plane. The system incorporated a UHTS400 NIR spectrometer with 300 grooves per mm grating and was calibrated using standard silicon with its 520 cm^{-1} Raman peak. Laser power was adjusted within the range of 1 mW to 2 mW for air immersion and 4 mW to 10 mW for oil immersion. Power measurements were recorded using a power meter (PM16−120−USB Power Meter, Thorlabs, New Jersey, USA) under the objective lens, slightly out of focus, in order to prevent any potential damage to the power meter sensor. For temperature−controlled measurements, a microscope temperature control stage (SG13701211, BoliOptics, California, USA) and a 50X air objective were utilized, allowing the temperature to be varied from 20 °C to 45 °C. This setup ensured controlled temperature conditions during the Raman spectroscopy measurements.

4.2.4 Raman Live−Cell Microscopic Characterization

For the air immersion experiment, 4 μL of MWCNTs−GNRs suspended in deionized water were deposited onto a cover glass slip and allowed to dry overnight. In the oil immersion experiment, PC3 cells were initially cultured on coverslips at a density of 1×10^5 cells/well and incubated in a 5% CO_2 atmosphere at 37 °C for 24 h. Following this incubation period, a 100 μL aliquot of MWCNTs−GNRs suspended in deionized water (initial concentration: 1 OD) was added to the cells, and they were further incubated for 24 h. Subsequently, the medium was replaced with phosphate−buffered saline (PBS).

To prepare for Raman live−cell imaging, small rectangular strips of double−sided tape were affixed horizontally along the top and bottom edges of a glass slide, and vacuum grease was applied to support the coverslip edges. The coverslip containing PC3 cells with MWCNTs−GNRs was gently inverted and placed, cell side down, on the tape. Following this, 10 μL of PBS was carefully added between the coverslip and the glass slide using a micropipette, ensuring complete filling of the space with saline buffer, preventing bubble formation, and maintaining cell viability. The coverslip edges were sealed with tape to preserve the integrity of the sample. This procedure ensured the controlled and optimal conditions for Raman live−cell microscopic characterization.

4.2.5 Data Acquisition

In the analysis of dry air samples, spectra were acquired at specific power settings through a repetitive process involving five runs at distinct spatial locations. To ensure statistical significance, spectra were collected from five different areas on the sample, with each area undergoing five spectra acquisitions. The acquired Raman signal was integrated over the range from anti−Stokes to Stokes regions, spanning −2400 to 2400 cm^{-1} in wavenumbers. The acquisition time for air−dried samples was set at 100 s. At each measured power, five consecutive spectra were collected, and each spectrum comprised 10 accumulations of 10 s. Similarly, five discrete cells were selected under designated power configurations for cell samples suspended in PBS media.

Spectral mapping of the surface was conducted in both air and aqueous solutions. For air−dried samples, a power setting of 2 mW (measured before the objective) was utilized with

a 50X objective, acquiring pixel data for 1 s. The scanned area had a spatial resolution of 10 μm × 10 μm, including 20 points and 20 lines. When scanning cell samples, a 6−mW power setting (measured before the objective) was employed with a 100X oil objective. Similarly, for a cell scan area of 10 μm by 10 μm (50 points per 50 lines), the data acquisition time was 1 s. This systematic approach ensured comprehensive and precise data collection for subsequent analysis.

4.2.6 Data Pre−Processing

Following the acquisition of data, a series of systematic pre−processing steps were implemented to refine and enhance the spectra. Data interpolation, background subtraction correction, and smoothing of Raman spectra were carried out using OriginPro2018 software (Northampton, USA). The built−in Multiple Peak Fit tools were employed for a more accurate determination of peak positions through deconvolution. Initially, interpolation techniques were applied to reconstruct spectra within specific spectral ranges, precisely interpolating the Stokes spectra from 1000 to 2000 cm^{-1} and the anti−Stokes spectra from −2000 to −1000 cm^{-1}. To mitigate the influence of background noise and spurious signals, a background subtraction technique was employed, effectively isolating the Raman signals from undesirable interferences. Subsequently, a smoothing procedure using the Savitzky−Golay method was implemented to reduce noise while maintaining essential spectral features. The Voigt method was applied to systematically deconvolute and extract the G Raman band from convoluted spectra. Pre−processing steps improve Raman spectra quality, ensuring accurate analysis and interpretation.

4.2.7 Cell Viability Analysis Following Laser Exposure

During laser treatment, cell viability was evaluated using the Trypan blue (Trypan blue stain, 0.4%, Gibco) exclusion assay. The prostate cancer cell lines (PC3) underwent the same preparation steps for Raman live−cell microscopic imaging, excluding the sealing of one side. Following laser exposure, Trypan Blue was introduced to assess cell viability. Confocal images of the cells were captured for subsequent analysis. The cell samples were exposed to a laser at 633 nm under a 100X objective with a time acquisition of 10 s. Given that Trypan Blue has background interference and is not suitable for Raman spectra, overall images of

the cell area before and after the laser exposure were captured using a 10X objective for a comprehensive analysis of cell viability. This approach provided a clear and comprehensive assessment of cellular response to laser treatment through the Trypan Blue exclusion assay and confocal imaging.

4.2.8 Statistical Analysis

The data presented are the mean ± standard deviation, derived from a minimum of five independent runs. Statistical analysis was carried out using Microsoft Excel 2010, OriginPro2018, and MATLAB R2023b.

4.3 Results

4.3.1 Raman Temperature Characterization of MWCNTs−GNRs

We investigated MWCNTs−GNRs as temperature probes using Raman spectroscopy. To ensure that temperature extraction relied on the intensity ratio of our material rather than being affected by laser−induced heating effects, we performed two different sets of experiments. First, we varied the levels of power application while maintaining a constant temperature. Second, the experiments were conducted at different initial temperatures, by using the heated stage system.

A confocal image depicting MWCNTs−GNRs is presented, with individual Raman spectra extracted from diverse spot areas, as illustrated in Fig. 4.1a. This characterization was vital for understanding the intrinsic properties of the material, particularly the Stokes and anti−Stokes signals. Subsequently, the characterization of MWCNTs−GNRs was carried out at room temperature, utilizing power outputs that varied from 1 to 2 mW, with a constant increase of 0.2 mW. This analysis demonstrated the evolution of the Stokes and anti−Stokes intensities of the G peak (i.e., 1580 cm^{-1}) as the power increased, as shown in Figs. 4.1b and 4.1c. Our main goal is to analyze the G peak, which is a unique feature of carbon−based materials. The G peak is sensitive to structural changes and is associated with the E_{2g} mode of sp^2 carbon atoms in the lattice structure [185, 242, 243]. While the D and G' peaks provide

valuable information, such as revealing defects or disorders in the carbon lattice, the G peak corresponds to the tangential mode in the plane and is linked to the stretching vibrations of C−C bonds in the graphene sheet [185, 243].

To discern between laser heating effects and intrinsic resonance effects, a controlled heating stage was introduced, systematically varying initial temperatures from 293 to 318 K (20 to 45 °C). The intensity ratio of Stokes and anti−Stokes signals (I_{aS}/I_S) was analyzed at different laser power levels and initial stage temperature values, as depicted in Fig. 4.1d. The relationship between laser power and temperature is observed to be linear for stages with temperatures ranging from 293 K to 308 K. Linear fits were conducted for each temperature set, revealing consistent slopes ranging from 0.200 ± 0.003 mW^{-1} to 0.293 ± 0.001 mW^{-1}, with an overall average of 0.027 ± 0.005 mW^{-1}, as shown in Fig. 4.1d. The strong linear correlation supports the assumption of linear photothermal heating validity. Regarding the temperature measurements at 318 K (45 °C), the laser power−dependent I_{aS}/I_S ratio overlaps with temperature measurements at 308 K (35 °C). These temperature changes may be due to overall system overheating, resulting in unexpected responses. Despite a low standard deviation observed at 318 K (45 °C), various factors, such as structural changes, degradation, or phase transitions in MWCNTs−GNRs at higher temperatures, could contribute to anomalies in the I_{aS}/I_S ratio at 318 K (45 °C). Mechanisms like vibrational pumping, colloid substrate heating, or underlying resonance may also play a role.

The determination of the local temperature of a sample is facilitated through Boltzmann distribution of the ground and first excited states of electron populations, utilizing the signal of a Raman band [177, 235]. The frequency dependence, raised to the third power in this equation, is derived from spectra acquired with a charged coupled device (CDD) detector, specifically designed for photon counting [177, 235]. The temperature−dependent equation governing the intensity ratio of Stokes (I_S) and anti−Stokes (I_{aS}) for a specific Raman mode is expressed through the contribution ratio (ρ) [177, 235]:

$$\rho = \frac{I_{aS}}{I_S} = A_i \frac{(\nu_o + \nu_m)^3}{(\nu_o - \nu_m)^3} \exp\left(-h\nu_m / k_B T\right) \tag{4.1}$$

Here, I_{aS} and I_S are the intensities of a Raman band, A_i is the asymmetry factor arising

from the different Raman enhancements of the anti−Stokes and Stokes components by a plasmon−excited nanostructure, ν_o [1/s] is the frequency of the vibrational Raman mode (i.e., Raman peak position), ν_m [1/s] is the frequency of the laser at a specific wavelength, h [J · s] is the Planck constant, k_B [J · K] is the Boltzmann constant, and T [K] is the temperature. As part of our investigation, we used power−dependent Raman measurements to determine the anti−Stokes/Stokes ratio, as shown in Fig. 4.1d. Our aim was to obtain accurate intensity measurements, which can be challenging due to the resonance factor that influences Raman signals when the excitation laser aligns with electronic transitions in the material. Tschannen et al. [185] explain that to extract the resonance factor experimentally, one must calculate the difference between the observed anti−Stokes/Stokes ratio ($I_{aS}/I_S = 7.5 \times 10^{-3}$) and the expected value from Eq. (4.1) at room temperature ($I_{aS}/I_S = 4.89 \times 10^{-4}$ at 293 K). The resulting disparity between the calculated and experimental anti−Stokes/Stokes ratio is 15.31. The two factors contributing to this disparity are the laser heating effect and the resonance effect of the MWCNTs−GNRs. The laser heating effect can be determined by calculating the factor that raises the ratio at room temperature ($I_{aS}/I_S = 1.1 \times 10^{-3}$ at 293 K) to the observed ratio at a higher temperature. With a 1.2 mW excitation power (using a 50X objective), the laser irradiation raises the local temperature to 308 K (35 °C), resulting in a 1.56−fold increase in the I_{aS}/I_S ratio ($I_{aS}/I_S = 2.0 \times 10^{-3}$ at 308 K) compared to room temperature (293 K). The remaining factor of 13.75, accounting for the deviation of the experimental I_{aS}/I_S ratio from Eq. (4.1), is attributed to a resonance effect in the air immersion experiment. Temperature values were extracted from Fig. 4.1e using Eq. (4.1), wherein $T = T_{set} + \beta I_{laser}$. Here, β refers to the photothermal heating coefficients, which is the slope obtained from the temperature as a function of power, and I_{laser} is the measured laser power. The determined average value of β was 52 ± 5 K/mW, providing valuable insights into the intrinsic photothermal properties of the plasmonic hybrid nanostructures under study, as depicted in Fig. 4.1f.

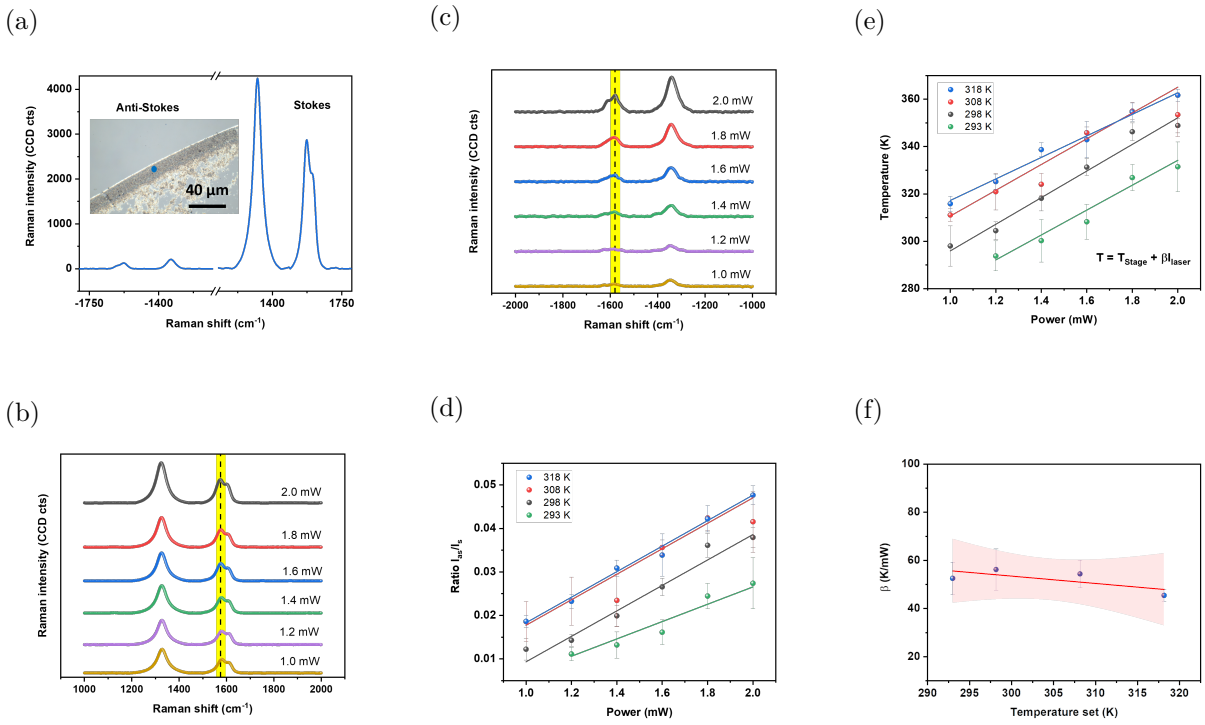

Fig. 4.1. Raman temperature characterization of MWCNTs–GNRs. (a) Stokes and anti–Stokes Raman spectra of MWCNTs–GNRs recorded at 633 nm, employing an input power of 2 mW and a 50X air objective. The inset image depicts the air–dried MWCNTs–GNRs, denoted by a blue dot, illustrating the chosen area. (b) Laser–dependent Stokes and (c) anti–Stokes spectra within the G vibrational mode at 1580 cm^{-1}, indicated by the yellow band, and an offset to distinguish each averaged spectrum. (d) The anti–Stokes/Stokes intensity ratio plotted against the excitation laser power at various temperature stages (293, 298, 308, and 318 K). The derived linear fit for each temperature set ranges from 0.200 ± 0.003 mW^{-1} to 0.293 ± 0.001 mW^{-1}. (e) Temperature–dependent behavior observed under different laser power conditions at distinct temperature stages. The temperature values are extracted utilizing Eq. (4.1) based on the data derived from (d). The derived linear fit for each temperature set is present in (f) as the intrinsic photothermal heating coefficient (β) of MWCNTs–GNRs determined at different stage temperature values. The light red shadow represents the 95% confidence band, along with the linear fit (red line), which represents the average photothermal heating coefficient of $\beta = 52 \pm 5$ K/mW. The error bars represent the standard deviation after 5 runs.

4.3.2 Raman Temperature Mapping of MWCNTs−GNRs

Raman temperature mapping of MWCNTs−GNRs was conducted to gain a comprehensive understanding of temperature distribution within a selected area, specifically a 10 μm × 10 μm area region. This transition to Raman mapping is aimed at providing a more detailed exploration of the material's properties, ensuring a foundation for subsequent *in vitro* investigations. The investigation involved studying the temperature distribution within the chosen area, as depicted in Fig. 4.2a, revealing intensity variations and hot spots. An example of a Raman spectrum from a single pixel is shown in Fig. 4.2b. Following background removal, a Σ−filter function, defined as the sum of the pixels covered by the selected area, (extracted using ProjectFive 5.1 software, Witec) was applied to extract the Stokes and anti−Stokes at 1580 cm^{-1}. The average neighborhood method (utilizing a 3×3−pixel block, see Appendix A.12) was then employed to smooth out the pixel map, resulting in Figs. 4.2c and 4.2d. Utilizing Eq. (4.1), the ratio intensity for the pixel map was extracted, leading to the creation of the ratio and temperature map in Figs. 4.2e and 4.2f, respectively. Analysis of the data showed a heterogeneous distribution within the temperature map, spanning from 300 to 340 K. The observed temperature heterogeneity in the samples is attributed to the agglomeration of MWCNTs−GNRs and the intricate interplay between gold−carbon composite entities influenced by electromagnetic coupling effects. Additionally, the non−uniform distribution of gold nanorod−carbon nanotubes across the sample surface significantly impacts localized temperatures, resulting in variations in acquired spectra. These fluctuations stem from complex interactions, including electromagnetic coupling and van der Waals forces. The combined effects lead to a diverse temperature range, highlighting structural heterogeneity and intricate intermolecular interactions. The presence of carbon nanotubes, with variable graphene layers exhibiting metallic or semiconductor properties, contributes to the heterogeneous temperature distribution. The dense coverage of gold on the carbon nanotube surface enhances Raman signals through the resonance effect, playing a pivotal role in the accuracy and sensitivity of temperature measurements.

Variations in spectral responses across individual spots, attributed to distinct temperature conditions, highlight the direct relationship between spatial temperature fluctuations and the diversity in collected spectra. In addition to these measurements, we calculated the

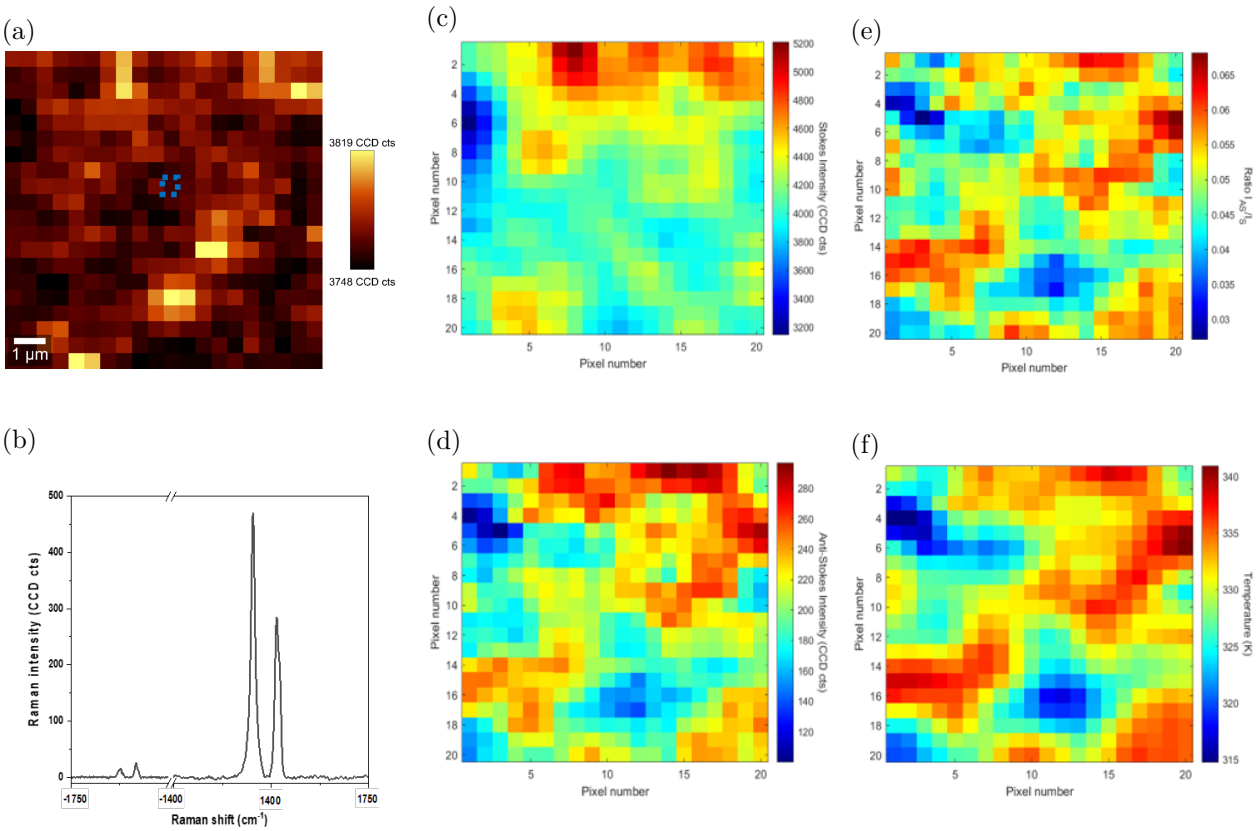

Fig. 4.2. Raman imaging and mapping of MWCNTs−GNRs. (a) Intensity Raman spectra mapping of MWCNTs−GNRs excited at 633 nm with 2 mW power, utilizing a 50X air objective. Scale bar is 1 μm. (b) Raman spectra taken from a single pixel (blue dashed square), encompassing both Stokes and anti−Stokes signals of MWCNTs−GNRs. (c) Map displaying the G frequency mode intensity distribution of Stokes peaks at 1580 cm^{-1}. (d) Map illustrating the intensity distribution of anti−Stokes peaks at −1580 cm^{-1}. (e) Map presenting the ratio of anti−Stokes to Stokes intensities. (f) Temperature map derived from Eq. (4.1). All the maps were measured over a 10 μm × 10 μm area with 20 × 20 pixels on the substrate.

expected confidence in the reported temperature at each pixel, in terms of a standard error of temperature (σ_T). The standard error in temperature values across the map serves as a key metric, allowing the evaluation of the consistency and dependability of temperature measurements spanning diverse points within the chosen area [235].

In the temperature determination based on the ratio of Stokes to anti−Stokes intensities, the typically low anti−Stokes intensity can significantly magnify inaccuracies due to noise [235]. Considering these variances as equivalent to the noise on the CDD pixel in the absence of a signal, commonly referred to as the dark intensity, provides a basis for standard error computation in our temperature assessment [235]. To establish confidence intervals for the calculated temperatures, it is essential to account for the dark noise. The blank measurement corresponds to the signal obtained just outside the Raman band, specifically on the anti−Stokes side, subsequent to background subtraction. Here we assume the dark noise signal on the anti−Stokes aligns with the Stokes signal, it follows that σ_{I_S} is equivalent to $\sigma_{I_{aS}}$ (i.e. 0.2162 CCD counts (cts)). This methodology ensures a consideration of noise factors, enhancing the reliability of our temperature assessments, and enabling the calculation of σ_T for each pixel in the temperature map. Figure 4.3 demonstrates that the spatial temperature distribution causes the elevated standard deviation in single−spot spectra. As shown in Fig. 4.3b, to calculate these intervals, we employed a standard error calculation approach, involving the determination of variances for both Stokes and anti−Stokes intensities, as expressed in Eq. (4.2):

$$\sigma_T = \sqrt{\left(\frac{\partial T}{\partial I_S}\sigma_{I_s}\right)^2 + \left(\frac{\partial T}{\partial I_{aS}}\sigma_{I_{aS}}\right)^2} \tag{4.2}$$

These expressions $\frac{\partial T}{\partial I_s}$ and $\frac{\partial T}{\partial I_{aS}}$ represent the partial derivatives of Eq. (4.1) with respect to the Stokes intensity and anti−Stokes intensity, respectively. Contributing to the variance are electromagnetic effects, thermal mechanisms, and the aggregated carbon−gold nanoparticle. Considering the anharmonic heating effect is essential because it arises from metallic nanostructures with gold−carbon or carbon−carbon. As shown in Fig. 4.3c, the relative error is calculated using Eq. (4.3):

$$Relative\ error = \frac{\sigma_T}{T} \tag{4.3}$$

A low relative error denotes a certain level of dependability in temperature measurements. It suggests that the signal−to−noise ratio was sufficiently high, enabling us to have a reasonable assurance in the reported temperature value. This statistical measure, such as 330 K ± 3 K with a confidence level of 95%, provides a range within which we can confidently state that the temperature of a specific pixel falls, as shown in Fig. 4.3c.

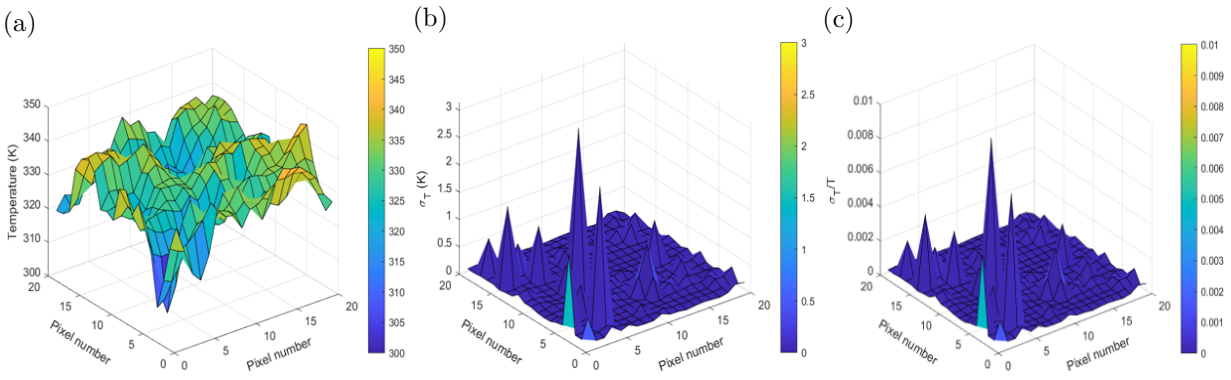

Fig. 4.3. Raman mapping of MWCNTs−GNRs under 633 nm excitation with 2 mW power using a 50X air objective. (a) Surface temperature distribution, (b) standard error mapping based on Eq. (4.2), and (c) relative error assessment from each pixel map, based on Eq. (4.3). All the maps were measured over a 10 μm × 10 μm area with 20 × 20 pixels on the substrate.

4.3.3 *In situ* Raman Temperature Measurement of a Single Cell

In situ Raman temperature measurements of a single living cell were conducted to assess the potential of MWCNTs−GNRs as temperature probes in prostate cancer cells. Our comprehensive investigation involved Raman's characterization of these probes, followed by their evaluation in cellular environments. For each power−dependent temperature experiment, we analyzed the Raman spectra using samples from five different cells. Figure 4.4a illustrates single Raman spectra, enabling differentiation between distinct components within the

sample, including PBS, a single PC3 cell, and the decorated carbon nanotubes. Raman spectra associated with biological specimens include distinct features such as carbohydrate signals in the range of 470−1200 cm^{-1} and bond vibrations of proteins in the range of 1500−1700 cm^{-1}. By extracting intensity ratios at various power levels, we calculated the corresponding temperatures using a predetermined equation, as depicted in Fig. 4.4b. Notably, our investigation covered a temperature range from 60 to 100 °C, surpassing the critical temperature threshold of 50 °C known for inducing cell death, as indicated in Fig. 4.4c. Concurrently, we observed cellular debris and structural changes through optical imaging in response to elevated temperatures. Our data revealed a substantial standard deviation for each data extract at different power levels, suggesting a complex interplay between the energy supplied to the sample and the resulting cellular temperature change.

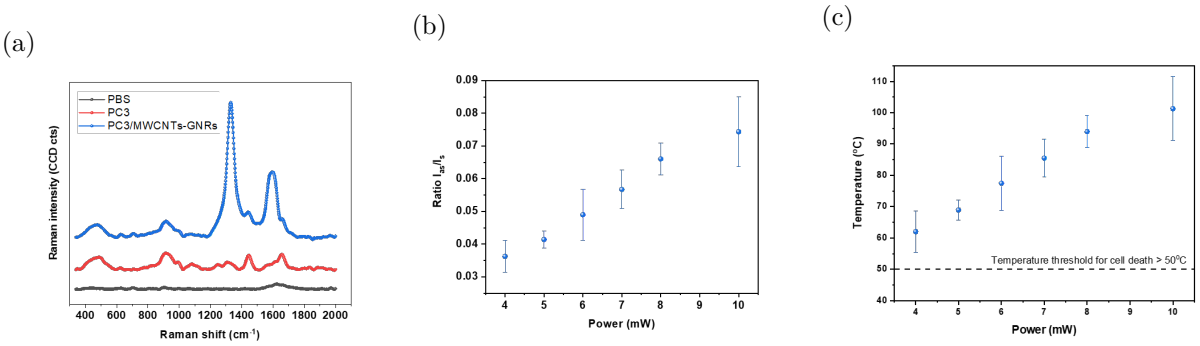

Fig. 4.4. Raman spectroscopy analysis of distinctive MWCNTs−GNRs incubated with PC3 cells. (a) Representative Raman spectra of MWCNTs−GNRs incubated with PC3 cells, where the black, red, and blue curves represent phosphate−buffered saline (PBS), the PC3 cell line, and gold−decorated MWCNTs with PC3 cells, respectively. Excitation was performed at 633 nm with 6 mW power, utilizing a 100X oil objective. (b) Anti−Stokes/Stokes ratio plotted against the excitation laser power at room temperature (293 K). (c) Temperature dependence observed under varying laser power conditions at room temperature. The temperature values are determined using Eq. (4.1). The dashed black line indicates the temperature threshold for cell death, set above 50 °C.

In order to gain a more comprehensive understanding of the observed variability, we conducted a Trypan blue−based assessment of cell viability. This assessment was designed to uncover the underlying factors contributing to the high standard deviation and to evaluate

the influence of the experimental conditions on cell viability. As depicted in Fig. 4.5a, the images were taken before and after with a 10X objective, but the measurements were taken at 100X for laser exposure. Our findings reveal varying degrees of cell viability across a range of powers, from 2 mW to 6 mW, shedding light on cellular responses to different energy inputs. Particularly noteworthy was the observation of diverse concentrations of decorated carbon nanotubes within individual cells, prompting an investigation into the viability of distinct cells under a constant power setting. The cellular viability studies provide essential information on the way hybrid nanoparticles are internalized by cells, resulting in differing intracellular concentrations and subsequent distinct temperature changes based on the effectiveness of light conversion into heat. The current work presents a comprehensive insight into the cellular responses to thermal stimuli, while simultaneously showcasing the promising potential of our Raman temperature probes in assessing the thermal sensitivities of biological systems. The results obtained from the use of Trypan blue, which displayed distinct responses by individual cells under constant conditions (Fig. 4.5b), may explain the observed variability in our temperature readings, ranging from 3 to 10 °C. This variability in temperature readings is believed to be caused by the divergent paths taken by the decorated carbon nanotubes in each cell.

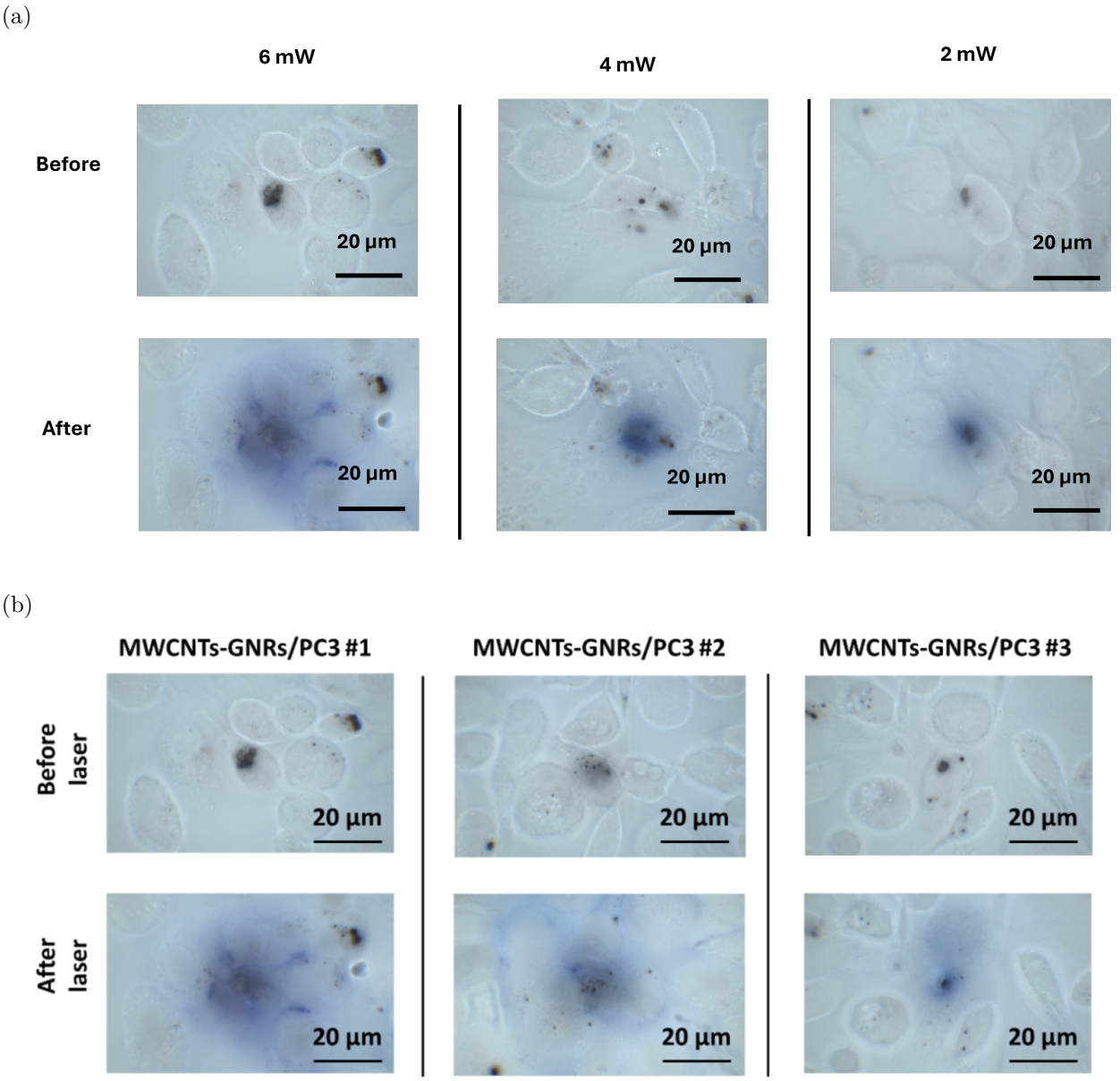

Fig. 4.5. Confocal image depicting comparative cell viability. (a) Assessment of PC3 trypan blue staining before and after laser exposure at various power levels, excited at 633 nm under the 100X oil objective. (b) PC3 cells incubated with MWCNTs−GNRs, excited at 633 nm with 6 mW power, captured under the 100X oil objective. Three examples are illustrated.

4.3.4 Raman Temperature Mapping of MWCNTs−GNRs with a Single Cell

Here, we conducted Raman mapping of a single cell with aggregated MWCNTs−GNRs to understand the temperature distribution within a selected area, specifically a 10 μm x 10 μm region, as shown in Fig. 4.6a. The intensity variation in different areas is evident, revealing a centered hot spot in the region containing MWCNTs−GNRs (Fig. 4.6b). After background removal, a Σ−filter function was applied to extract the Stokes and anti−Stokes at 1580 cm^{-1}. The average neighborhood method was then employed to smooth out the map, as shown in Figs. 4.6c and 4.6d. Based on the Raman intensity ratio Eq. (4.1), we extracted the ratio intensity for the pixel map, followed by the creation of the temperature map, as depicted in Figs. 4.6e and 4.6f. As previously demonstrated, the resonance factor was extracted based on the discrepancy between the observed and calculated anti−Stokes and Stokes intensities ratio. The cellular environment caused an increase in the resultant resonance factor of 17.45. The data results show a heterogeneous distribution in the temperature map ranging from 300 to 380 K. Agglomeration of MWCNTs−GNRs and electromagnetic coupling interactions in the gold−carbon composite explain this observation. The non−uniform distribution of MWCNTs−GNRs and van der Waals interactions cause the spatial temperature distribution, which explains the high standard deviation seen in single−spot spectra, as depicted in Fig. 4.1e.

It is essential to incorporate a confidence interval into the pixel map when analyzing the temperature map from our Raman mapping of a single cell incubated with nanoparticles, as depicted in Fig. 4.7a. Accuracy in temperature determination is important due to the reliance on the ratio of Stokes to anti−Stokes intensities, and it provides the means to confidently assert that the temperature within a specific pixel falls within a defined range, such as 340 K $\pm$ 10 K, with a confidence level of 95%, as shown in Fig. 4.7b. This approach provides a means to assess our confidence in the respective temperature values, enhancing the reliability of our temperature mapping, as depicted in Fig. 4.7c.

In our Raman experiments, challenges emerged, including cross−contamination risks in cell sampling, carbonization effects, and bubble formation at high energy density. Scaling up for bulk cellular temperature measurements presented additional complexities [224]. The

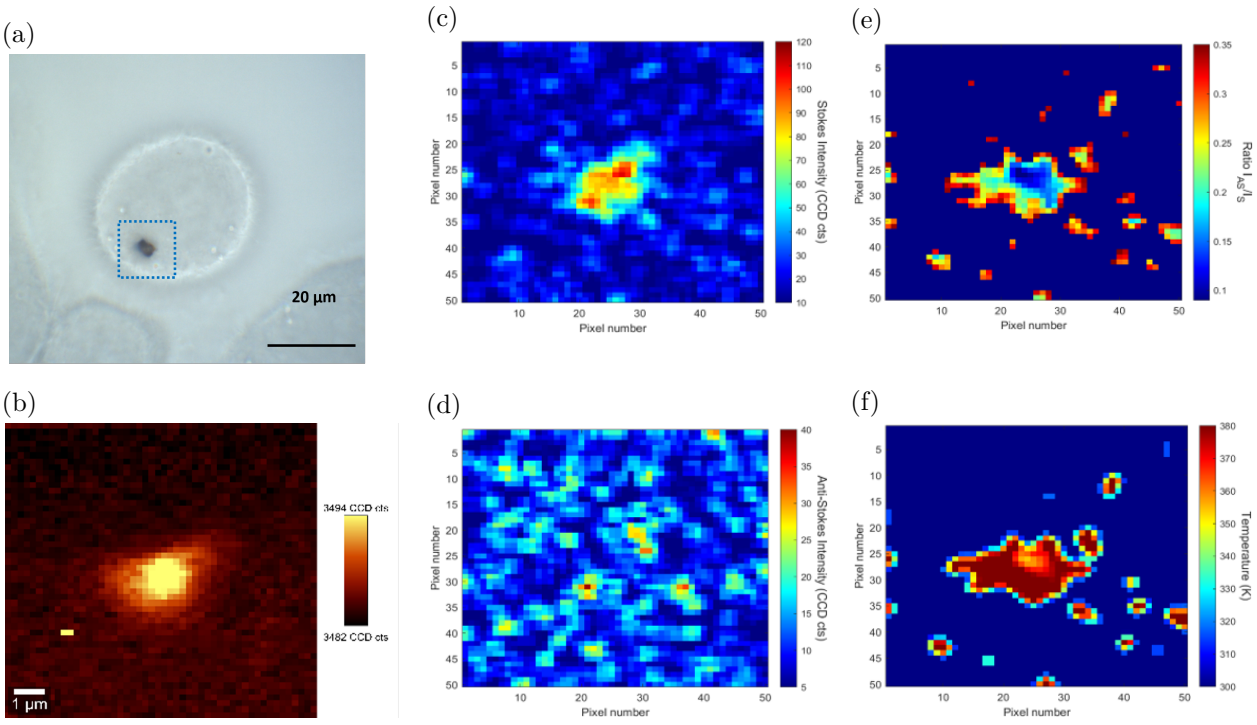

Fig. 4.6. Raman imaging and mapping of MWCNTs−GNRs incubated with a single PC3 cell. (a) Optical microscope image of the surface of a single cell with aggregated MWCNTs−GNRs and (b) corresponding Raman mapping excited at 633 nm with 6 mW power, utilizing a 100X oil objective. Raman map illustrating the intensity distribution of (c) Stokes and (d) anti−Stokes G band peak at 1580 cm^{-1}. (e) Raman map presenting the G frequency mode of the ratio of anti−Stokes to Stokes intensities. (f) Temperature map derived from Eq. (4.1). All the maps were measured over a 10 μm ×10 μm area with 50 × 50 pixels on the substrate.

interaction of non−targeted moieties with carbon nanotubes led to nanoparticle aggregation around cells, necessitating the exploration of unknown factors such as electrostatics, surface deposition, and cellular uptake mechanisms. The identification of temperature fluctuations and uneven distributions, highlighted by a higher relative error, is critical in the context of nanoparticle−cell interactions [244]. Precise temperature control is fundamental for interpreting nuanced dynamics, and attention to σ_T of temperature and its relative error ensures data integrity and accuracy in temperature assessments.

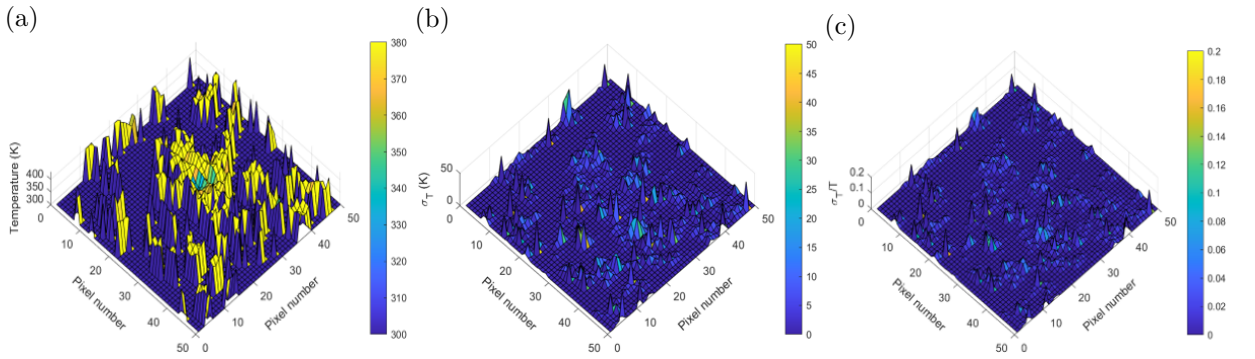

Fig. 4.7. Raman mapping of MWCNTs−GNRs incubated with a single PC3 cell under 633 nm excitation with 6 mW power using a 100X oil objective. (a) Spatial distribution of surface temperatures, showcasing localized variations ranging from 300 to 380 K. (b) Mapping of standard error derived from Eq. (4.2), ranging from 300 to 380 K. (c) Assessment of relative error at each pixel map, calculated on Eq. (4.3), offering insights into measurement reliability. All the maps were measured over a 10 μm × 10 μm area with 50 × 50 pixels on the substrate.

4.4 Discussion

Raman thermometry stands as a pioneering technique for non−contact temperature measurement through Raman scattering, offering precise monitoring within localized regions and facilitating optimal adjustment of laser parameters [184, 245, 246]. The method involves light−molecule interactions, inducing a frequency shift in the scattered light. By extracting Stokes and anti−Stokes signals and analyzing their ratio within a specific Raman band, temperature−dependent changes in the molecule can be inferred [177, 235]. Leveraging Anti−Stokes Raman spectroscopy with gold−decorated MWCNTs as localized temperature probes enables direct measurement at the cellular level. This technique proves invaluable for monitoring temperature changes during photothermal therapy, enhancing treatment parameter optimization [181, 238, 247].

Nanothermometers, particularly MWCNTs−GNRs, exhibit extensive potential in cancer research, especially within the therapeutic near−infrared window [248]. Their sensitivity to temperature changes provides real−time thermal information in photothermal cancer research. Future research directions should refine nanothermometer design for enhanced sensitivity and

address potential cytotoxicity concerns. Exploring applications in three−dimensional cell cultures and animal models can bridge *in vitro* and *in vivo* studies. Integrating advanced imaging techniques, including multi−modal imaging, promises a comprehensive understanding of temperature dynamics, especially in micro−tumor environments [249]. Raman pulse lasers [250, 251], capable of distinguishing spectral signatures between healthy and tumor cells, offer potential real−time cancer screening and diagnosis [252]. This multidimensional approach advances our understanding of nanoscale temperature dynamics in cancer research.

4.5 Conclusion

In this chapter, we demonstrated the feasibility of MWCNTs−GNRs as a nanoscale temperature probe to achieve non−invasive, spontaneous, self−referencing, and label−free measurements without the need for external Raman probe molecules. And we provided a detailed characterization of their intrinsic photothermal heating properties. First, we showed that temperature dependence of MWCNTs−GNRs mode Stokes and anti−Stokes ratio under varied conditions allows for *in situ* temperature measurements at the single−cell level. Second, we presented a temperature map distribution with pixel−level confidence intervals, thereby ensuring its reliability. Furthermore, we demonstrated the efficacy of gold−decorated MWCNTs as label−free temperature probes in cell heating experiments and identified the optimal temperature range for inducing cell death. The ability to provide temperature information during photothermal therapy positions this technique as a valuable asset in cancer research. We also assessed prostate cancer cell temperatures and viability by analyzing anti−Stokes and Stokes signals of the G peak at various laser powers. Our findings imply that MWCNTs−GNRs can efficiently heat cancer cells and serve as non−invasive temperature probes for *in situ* monitoring. This study thus opens avenues for future research, emphasizing the potential of MWCNTs−GNRs in advancing anti−Stokes Raman thermometry applications and their significance in the field of precision medicine.

Chapter 5

Final Remarks

5.1 Conclusions

In conclusion, this thesis explored the potential of multi-walled carbon nanotubes decorated with plasmonic gold nanorods for enhanced local absorption and heat conversion within the near-infrared biological window for PTT applications. The synergistic effects between these two nanomaterials lead to significant outcomes, including strong NIR absorption, and enhanced photothermal conversion efficiency. These results contribute to improving *in vitro* ablation efficacy. This thesis highlighted the unique advantages of GNRs-decorated MWCNTs in three key areas: 1) serving as NIR photothermal transducers and 2) functioning as nanoprobe thermometers in photothermal cancer therapy.

We demonstrated the superiority of MWCNTs−GNRs in the first NIR biological window by showing a significant photothermal enhancement compared to bare MWCNTs. To optimize light-to-heat conversion efficiency within the NIR biological transmission window, we decorated MWCNTs with plasmonic GNRs. We introduced and applied a new metric factor for NIR absorption per carbon atom. Our results indicate a significant photothermal enhancement of hybrid MWCNTs−GNRs compared to bare MWCNTs, with a 4.9 enhancement factor per unit mass of carbon. At a preliminary stage, the hybrid nanoparticles indicate biocompatibility with non-targeted prostate cancer cell lines after 72 hours of incubation at various concentrations. By using a continuous wave laser at 808 nm, we established a temperature profile at different

irradiation times, allowing us to link cell viability to energy delivery and temperature measured during irradiation. The results of the cell viability assessment of various nanoparticle components demonstrate that MWCNTs−GNRs induce the destruction of cancer cells, resulting in their conversion into debris.

The use of Raman spectroscopy is explored for potential therapeutic applications in this thesis. This is achieved through the employment of prostate cancer cell lines to examine the *in vitro* effects of hybrid plasmonic nanostructures. Notably, the incorporation of plasmonic nanoparticles onto carbon nanotubes exhibits significant advantages over existing PTT agents, as this feature leads to efficient heat generation at the cellular level, thereby maximizing damage to tumor cells. The research extends to the evaluation of MWCNTs−GNRs with prostate cancer PC3 cell lines, assessing *in situ* cellular temperature and generating temperature maps for a selected region. Importantly, the study covers a temperature range from 60 °C to 100 °C, exceeding the critical threshold of 50 °C associated with inducing cell death.

The research work encompasses the design and synthesis of a novel plasmonic nanomaterial for therapeutic applications, as well as experimental and numerical evaluations of its effectiveness as a photothermal agent using both continuous wave and short-pulse laser techniques.

5.1.1 Key Findings and Challenges

Throughout this thesis, we have focused on the development and characterization of a novel plasmonic hybrid nanomaterial− gold nanorods decorated on multiwalled carbon nanotubes − for NIR photothermal cancer therapy. A closer examination of its performance and potential enhancements is essential to advance this innovative approach. Notably, our key findings affirm the strong near-infrared absorption of this hybrid nanomaterial, establishing its effectiveness as a photothermal agent. These insights result from a comprehensive investigation utilizing both computational and experimental approaches.

5.1.1.1 Numerical Evaluation of Optical Properties

The optical properties of gold-decorated MWCNTs have been extensively examined through numerical simulations. Utilizing the finite element method software COMSOL Multiphysics

5.6, we studied the optical spectral distributions of both bare and plasmonic-decorated carbon nanotubes. This computational model has yielded an in-depth understanding of plasmonic photothermal therapy and demonstrated the effectiveness of plasmonic hybrid carbon nanotubes as photothermal agents.

The simulation of the optical properties of gold-decorated MWCNTs presents a multitude of challenges that may vary in nature. Among these challenges are the following: 1) the intricate modeling of the hybrid nanostructure, which necessitates consideration of its size, shape, and composition. 2) The actual distribution of GNRs on the surface of MWCNTs may not be uniform, leading to variations that are difficult to replicate in simulations. 3) The surface modifications that occur during the synthesis process are not fully accounted for in theoretical models, resulting in a discrepancy between the optical spectrum obtained from simulations and the UV-Vis spectra measured experimentally (as shown in Fig. 3.2f).

5.1.1.2 Synthesis and Morphology of MWCNTs−GNRs

Our synthesis approach involves the gold decoration of carbon nanotube surfaces, establishing strong covalent bonding. However, the covalent bonding process between carboxylated MWCNTs and amine-functionalized GNRs can be challenging due to various factors, such as the uniform distribution of GNRs in terms of aspect ratio and surface attachment variability of amine-functionalized GNRs to the surface of MWCNTs.

To improve covalent bonding, additional spectroscopic techniques such as X−ray photoelectron spectroscopy (XPS) can be used to provide detailed information about the chemical bonds and confirm the presence of desired functional groups. Also, addressing the challenge of accurately measuring the amount of GNRs adsorbed onto the surface of MWCNTs necessitates careful evaluation and the implementation of appropriate methods. Inductively coupled plasma mass spectrometry (ICP−MS) and UV−Vis spectroscopy are two methods that can be employed to determine the amount of gold present on the surface of MWCNTs. To improve the accuracy of quantitative measurements, calibration standards with known concentrations of GNRs should be established. By generating calibration curves that relate absorbance to particle concentration, the quantitative measurement of gold can be enhanced. These analytical techniques promise valuable insights into the chemical composition and con-

centration of the synthesized materials, facilitating the refinement of our synthesis approach and addressing challenges related to achieving an ideal composite concentration.

5.1.1.3 Experimental Setup for Efficient Thermal Ablation

The experimental setup, employing an 808 nm CW laser and an infrared pyrometer sensor for temperature measurement along two orthogonal axes, demonstrated effectiveness in water and cellular environments. Challenges encountered include the need for a versatile lens system to adjust focal lengths for varied beam diameters and implementing an adjustive piezo−electric stage for sample positioning, especially in cell culture plates. Additionally, a visible laser alignment (e.g., 633 nm, $\sim$ 1 mW) is needed to guide NIR laser irradiation.

When deciding between CW and pulsed lasers, it is important to consider the treatment protocols and the location of the tumor within the body, whether it involves *in vitro* or *in vivo* experiments in a complex biological environment. A pulsed laser might be preferable if tumors are deeper within the body because it can penetrate tissues more effectively than CW lasers. Pulsed lasers offer advantages in achieving precise spatial and temporal control for therapeutic effects while minimizing damage to healthy tissues, delivering high energy in a very short duration. However, the use of pulsed lasers necessitates careful consideration of the high−energy pulses applied to the biological system, as they have the potential to cause irreparable damage to surrounding healthy tissues. Integration of advanced imaging techniques, such as real−time CCD camera imaging, can address challenges related to monitoring temperature changes and MWCNTs−GNRs distribution with heightened spatial and temporal resolution.

5.1.1.4 Raman Spectroscopy for Cellular Temperature Measurement

Raman thermometry *in situ* of individual cells involves establishing a temperature probe without external Raman probes, utilizing intrinsic properties of MWCNTs, and enhancing signals with GNRs. This innovative pairing offers a nuanced understanding of temperature dynamics during experimental procedures, particularly in the context of photothermal therapy, emphasizing the importance of precise temperature monitoring for optimizing therapy outcomes. Challenges encountered include noise background from glass substrates and PBS

solutions (vital for cell viability during experiments), necessitating temperature mapping and data analysis to assess data reliability. Cell preparation and the diverse responses of different cells to nanoparticle incubations are integral considerations in the process. Targeting specific cells helps avoid nanoparticle agglomeration. The confocal objective setup, preferably from the bottom, further contributes to experimental success. One notable challenge in Raman spectroscopy, particularly with cell samples, is the interference from background signals. This interference is pronounced when using glass substrates and cell culture solutions. To address this issue, strategies such as exploring alternative substrates (e.g., quartz or calcium fluoride CaF_2) and cell solutions with minimal Raman signal interference are crucial. These adjustments enhance the precision of Raman spectroscopy in cellular studies, making it more applicable to the intricacies of photothermal therapy research.

5.2 Future Works

In the realm of advancing photothermal therapy using MWCNTs−GNRs, our future research endeavors focus on several key domains to augment the efficacy and clinical translatability of this innovative approach. Our research has laid the foundation for further exploration and application of MWCNTs−GNRs in NIR photothermal therapy and beyond.

5.2.1 Simulations

The utilization of advanced computational models and simulations serves as a pivotal foundation for future research endeavors. These computational approaches possess the capacity to elucidate intricate interactions and forecast the behavior of gold−decorated MWCNTs in a variety of biological settings. It is imperative to refine these models to simulate realistic conditions, incorporating variables such as physiological parameters, cellular responses, and pharmacokinetic data to enhance the predictive capabilities of the computational framework. Moreover, the development of realistic models of tumor tissue inoculated with nanoparticles is essential to overcome the assumption of uniform distribution. The integration of fluid dynamics and tissue optical data in the NIR spectrum, particularly in the second biological window range, is important to consider during the simulation. Additionally, the significance

of temperature management during therapy, as well as real−time control over temperature increment, should not be overlooked.

5.2.2 Improved Photothermal Agent

An important consideration in this field is evaluating the long-term stability and performance of nanomaterials under repeated irradiation schedules. Through systematic investigations, the impact of various dimensions, shapes, and compositions on the photothermal properties of these agents will be assessed. It is essential to understand their behavior when exposed repeatedly to near-infrared light to assess their viability and durability in therapeutic applications. Further research is needed to refine existing nanomaterials and explore novel candidates to enhance photothermal conversion efficiency. The investigation of alternative plasmonic materials, such as titanium nitride (TiN), is noteworthy. Their high absorption in the near-infrared spectrum, biocompatibility, and existing use in biomedical applications make TiN a promising candidate for photothermal therapy.

5.2.3 Enhanced Biocompatibility and Tumor Targeting

Preliminary *in vitro* experiments with non-targeted gold-decorated MWCNTs have demonstrated promising results in the treatment of prostate cancer cell lines. However, further investigation involving diverse prostate cancer cells, such as LNCAPs and PC3, incorporated with functional moieties, is necessary to comprehensively assess the photothermal performance. A thorough examination of the biodistribution, cytotoxicity, and pharmacokinetics of hybrid nanomaterials in animal models is essential to comprehensively assess safety and efficacy. This includes PEGylating the surface of MWCNTs−GNRs, exploring extracellular vs. intracellular therapy dynamics, cellular uptake, evaluating the effects of concentration and incubation time, studying circulation, biodistribution, and tolerance, and assessing cell viability through CCK−8 assays. The subsequent research phase will focus on refining the specificity and tumor selectivity of the nanomaterial through targeting ligands or surface modifications to minimize off-target effects and improve treatment outcomes. This will be achieved by immobilizing targeting reagents using antibodies, aptamers, and peptides to ensure precise and selective targeting of cancer cells or tumor sites.

5.2.4 Development of Multifunctional Photothermal Agents

Our research agenda focuses on creating multifunctional nanomaterials integrating photothermal therapy, nanothermometry, and photoacoustic imaging to enhance therapeutic efficacy. The primary objectives of our study include creating nanoparticles that offer combined heating, tracking, and sensing capabilities. The development of a new apparatus that combines heating, nanoparticle tracking, thermal sensing, and recording health-related parameters simultaneously is another key objective. To assess treatment response, we plan to design a comprehensive metric figure that integrates critical parameters such as energy delivery, temperature, and cell viability. Additionally, we suggest that a microfluidic device for real-time examination of dissected tumors, providing insights into their biological activities through Raman fingerprints, would advance future research in this field. A pulsed laser system for Anti−Stokes Raman scattering applications is also envisioned, and investigations into decorated MWCNTs along with the optical pulse delivery system would aim to optimize high-energy delivery to deep tissues while minimizing damage to surrounding normal cells.

Our envisioned approach involves implementing a pulsed laser beam delivery system with picosecond timescale pulses, maximizing tumor damage by generating highly localized heat and vapor bubbles around nanoparticle surfaces for mechanical damage. We also suggest exploring hybrid plasmonic nanobubbles through a pulse laser photoacoustic bubble detector system. Furthermore, we suggest designing beam variations for both *in vitro* and *in vivo* experiments, with a specific focus on the light-induced cavitation process. To enhance the reliability and interpretability of our experimental outcomes, we propose leveraging advanced characterization techniques, including *in situ* spectroscopy and imaging. Establishing reference figures for cell viability, temperature, and energy delivered will contribute to a comprehensive understanding of our study. These benchmarks will enhance the reliability and interpretability of experimental outcomes.

5.2.5 Clinical Translation and Combination therapy

Overcoming the current technological hurdles is crucial for advancing the clinical application of PTT. Investigating combination therapies, particularly those involving immunotherapy or targeted drug delivery, will be a critical pathway for improving treatment outcomes. By

exploring how these therapies can complement and enhance the benefits of near-infrared photothermal therapy, we envision developing more comprehensive and effective cancer treatment strategies. Furthermore, a multifaceted approach that integrates nanomaterial synthesis, analytical techniques, and computational modeling is necessary to address the challenges in advancing cancer therapy. The use of gold nanorods coated on multi-walled carbon nanotubes serves as a prime example of this approach, demonstrating both effectiveness and the potential for improving properties and exploring new applications, with the promise of translating theoretical potential into tangible benefits for cancer therapy in the future.

Appendix A

Characterization, Calculations, and Codes

A.1 Optical System

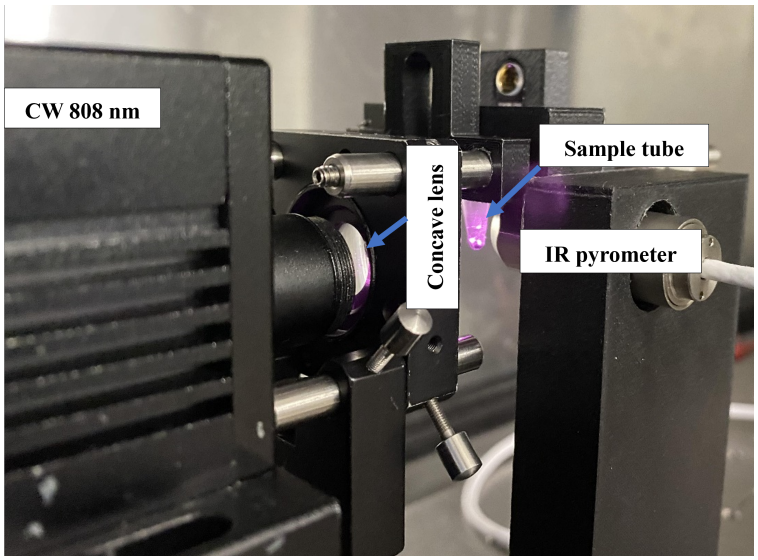

Fig. A.1. The optical system for NIR photothermal irradiation.

A.2 TGA and Zeta Potential Analysis of MWCNTs Conjugation Chemistry

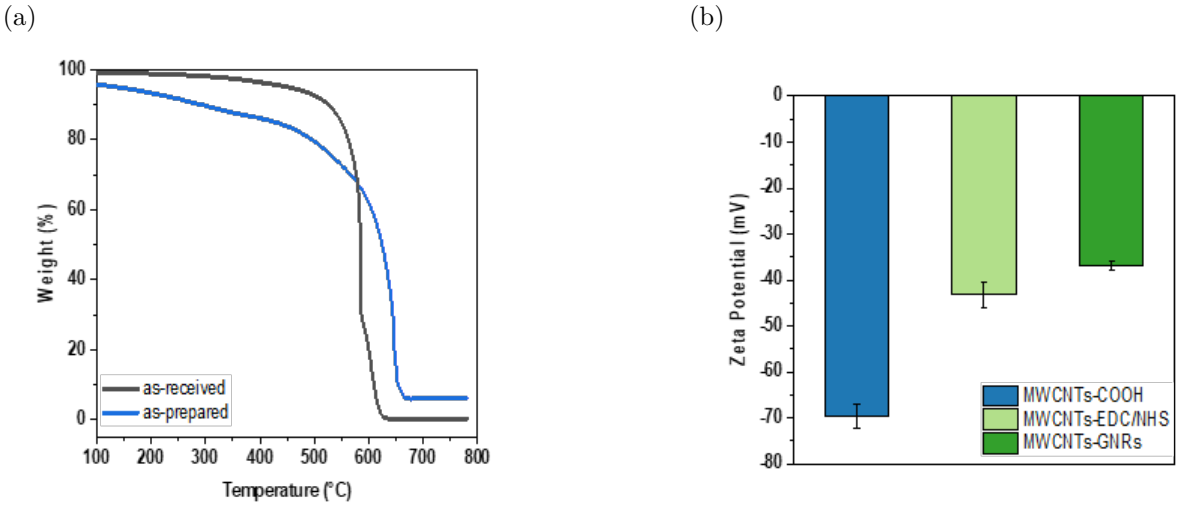

Fig. A.2. (a) TGA of as-received and as-prepared MWCNTs. (b) Zeta potential analysis of carboxylated MWCNTs (blue curve), MWCNTs−EDC/NHS (yellow-green curve), and GNRs−decorated MWCNTs (green curve).

Table A.1. The zeta potentials of MWCNTs at different stages during the covalent bonding process.

Samples	Zeta Potential (mV)
MWCNTs−COOH	-70 ± 3
MWCNTs−EDC/NHS	-43 ± 3
MWCNTs−GNRs	-37 ± 1

A.3 TEM Characterization of MWCNTs−GNRs

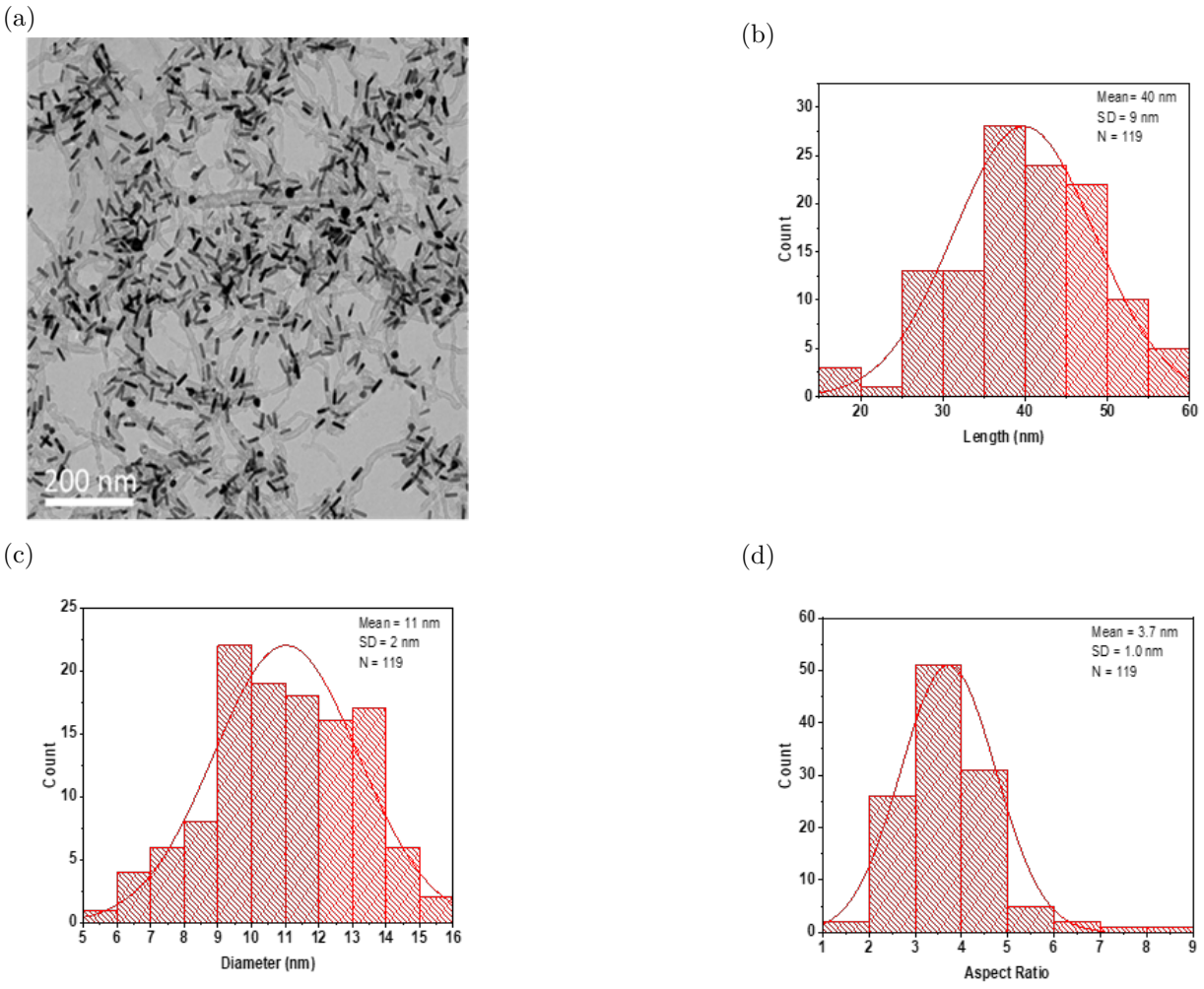

Fig. A.3. (a) TEM images of MWCNTs−GNRs at 200 nm scale. Statistical analysis of 120 GNRs based on TEM image to determine (b) the length, (c) the diameter, and (d) the aspect ratio.

A.4 UV−Vis Spectra of MWCNTs−GNRs and GNRs

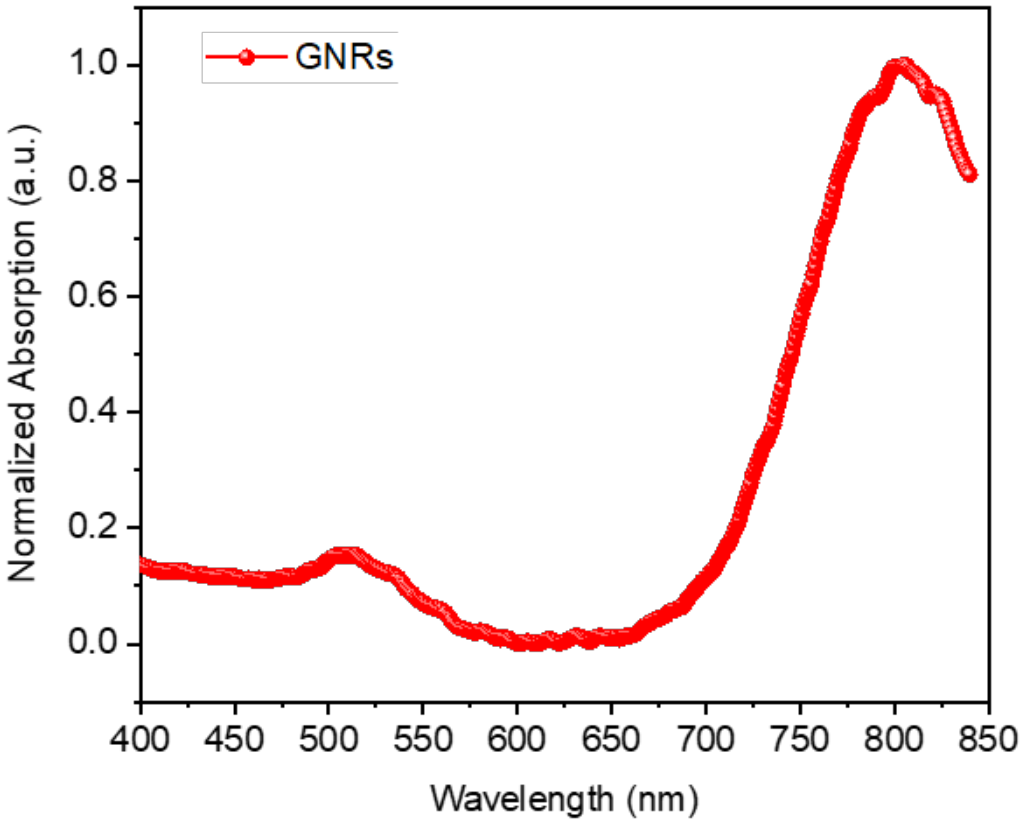

Fig. A.4. Normalized absorption spectra of GNRs.

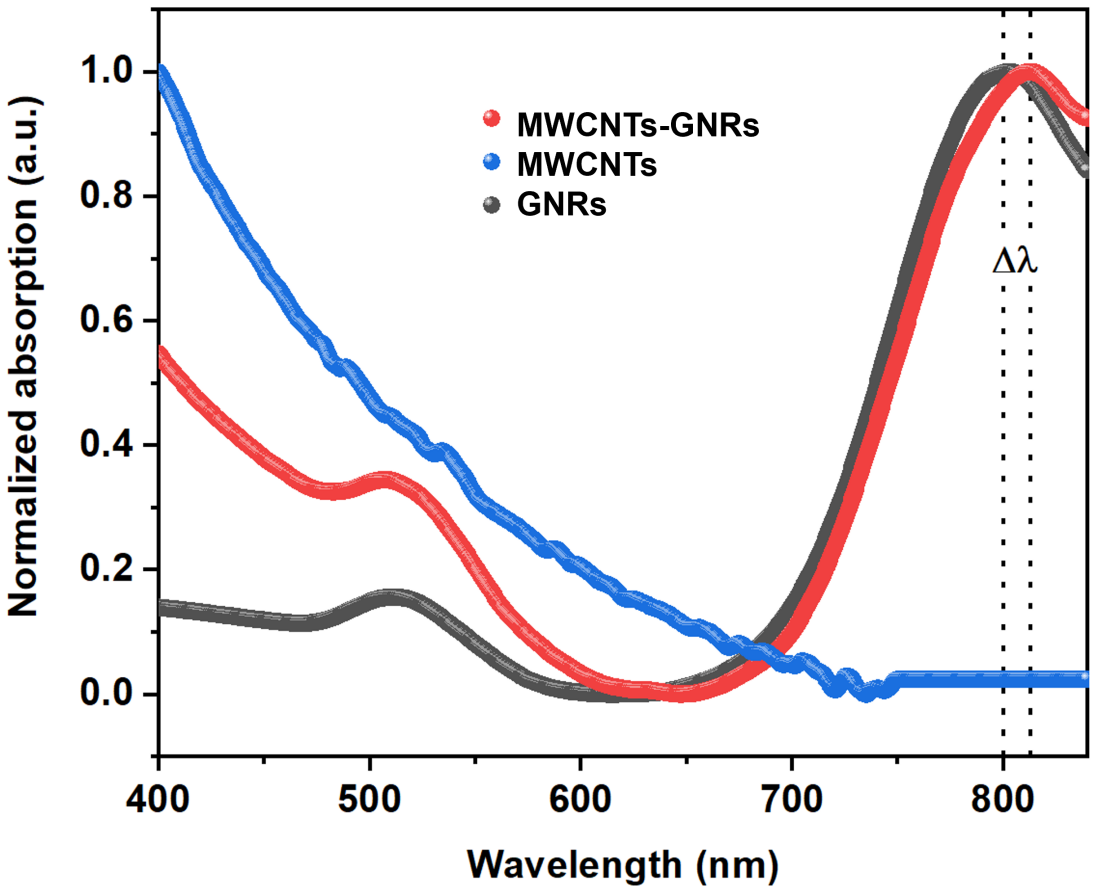

Fig. A.5. Normalized absorption spectra of MWCNTs−GNRs (red curve), MWCNTs (blue curve), and GNRs (black curve). The hybridized MWCNTs−GNRs exhibit a redshift of $\Delta\lambda$ = 13 nm compared to the bare GNRs.

Figure A.5 shows that the hybridized MWCNTs-GNRs exhibit a redshift of approximately 13 nm compared to the bare GNRs. This redshift is attributed to electromagnetic coupling between the two nanomaterials, which leads to modifications in the plasmonic properties of the GNRs, resulting in a shift in their NIR absorption peak position.

A.5 COMSOL Simulation and Far−Field Scattering of MWCNTs−GNRs

The near−field optical properties of the nanostructures were numerically solved in the frequency domain using the scattering field formulation in a commercially available FEM package (COMSOL Multiphysics 5.6 with the RF module). The 3D simulation space was composed of a nanostructure, an embedded spherical medium, and a perfectly matched layer (PML) spherical domain with a scattering boundary condition, as shown in Fig. 3.2b. The embedded medium was water, with a refractive index of n = 1.33. The dielectric permittivity of gold and carbon nanotube components were obtained from Johnson and Christy [253], and Djurišić [254], respectively. To perform the simulation, we employed a free tetrahedral meshing algorithm from COMSOL with a tetrahedral element. The simulation was performed in the visible and near-infrared wavelength ranges of 200 nm and 1200 nm, respectively, with a spectral resolution of 10 nm using a parametric sweep. The Helmholtz equation is used to describe the electromagnetic interaction between the laser and nanostructure in an aqueous environment as follows:

$$\nabla \times \mathbf{u}_r^{-1}(\nabla \times \mathbf{E}) - k_0^2 \varepsilon \mathbf{E} = 0 \tag{A.1}$$

where u_r is the relative permeability of the particle, E is the sum of the electric fields, which consists of the incident and scattered fields, $E = E_{inc} + E_{sca}$, k_0 is the wave propagation vector, and ϵ is the dielectric permittivity of gold, which is composed of both the real and imaginary parts. When solving the scattered field, the incident light for a plane wave polarized along the x-axis and propagated along the z-axis is defined as,

$$\mathbf{E}_{\text{inc}} = \mathbf{E}_o e^{(-j\frac{2\pi n}{\lambda}z)\hat{\imath}} \tag{A.2}$$

where E_o is the amplitude wave [V/m], n is the refractive index of the medium, λ and is the wavelength [nm]. The plane wave propagation direction is selected to resonate with the

longitudinal mode of MWCNTs−GNRs, thereby inducing NIR resonance.

(a) (b)

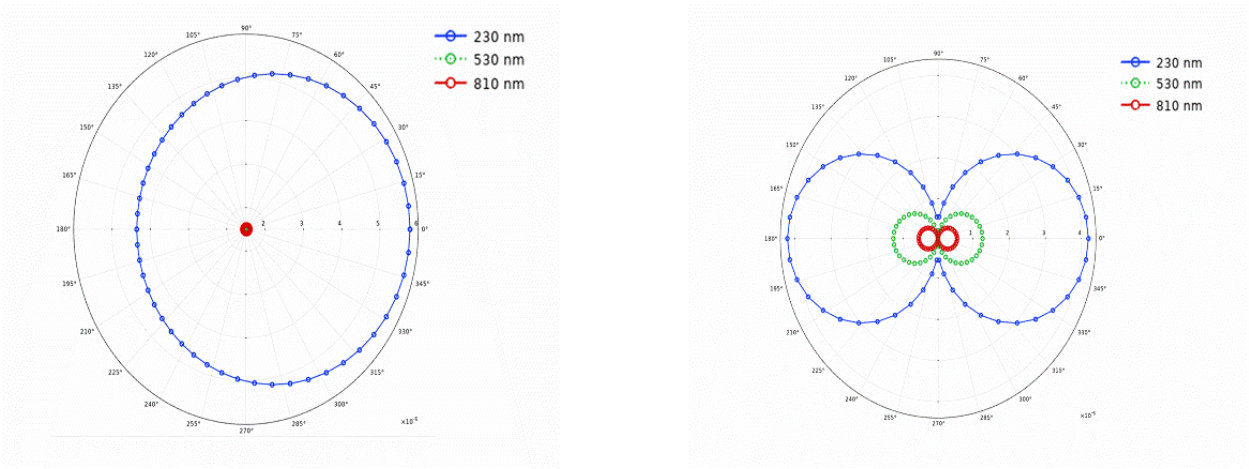

Fig. A.6. Numerically calculated far-field scattering of (a) transverse and (b) longitudinal resonance of MWCNTs−GNRs, at different wavelengths (230, 530, and 808 nm), showing insignificant scattering magnitude in the near-infrared wavelength.

A.6 Calculation of the Photothermal Conversion Efficiency

The figure of merit (η) determines the heating efficiency of the incident power transduced by the nanoparticles to generate heat that causes cell death. The optical absorbance of hybrid nanoparticles was investigated using a UV−Vis−NIR spectrometer. Using this spectrometer tool, we extracted the optical density (A_λ) at different nanoparticle concentrations, with a focus on the NIR wavelength (808 nm). Based on the total energy balance equation for the system [55]:

$$\sum_i m_i C_{p,i} \frac{dT}{dt} = Q_{\text{NP}} + Q_{\text{sys}} - Q_{\text{diss}} \tag{A.3}$$

where m and C_p are the mass and heat capacity of the sample solution, respectively. T is the temperature of the solution, and Q_{NP} is the energy input by the nanoparticles, and Q_{sys} is the baseline energy input by the solvent (i.e., deionized water), and Q_{diss} is the outgoing energy, which is the energy dissipated from the system to the surroundings. The term Q_{NP} is defined as the laser-induced heat input, as follows:

$$Q_{\mathrm{NP}} = I(1 - 10^{-A_{808}})\eta \tag{A.4}$$

where I is the incident laser power in W/cm^2, A_λ is the absorbance of the nanoparticles at a given wavelength λ (i.e., 808 nm). The term $\mathrm{Q_{diss}}$ is the heat dissipation linear to the temperature of the system, defined as:

$$Q_{\mathrm{diss}} = hS(T_{\mathrm{max}} - T_{\mathrm{sur}}) \tag{A.5}$$

where h is the heat transfer coefficient, S is the exposed surface area of the cuvette, T_{max} is the maximum temperature reached by the nanoparticles, and T_{sur} is the surrounding temperature. When the temperature reaches equilibrium, T_{max}, $\frac{dT}{dt} = 0$, and Eq. (A.3) becomes:

$$Q_{\mathrm{NP}} + Q_{\mathrm{sys}} - Q_{\mathrm{diss}} = 0 \tag{A.6}$$

When the laser is off, the heat input terms become zero, and Eq. (A.3) becomes:

$$\sum_i m_i C_{p,i} \frac{dT}{dt} = -Q_{\mathrm{diss}} = hS(T_{\mathrm{max}} - T_{\mathrm{sur}}) \tag{A.7}$$

Rearranging it, it gives:

$$dt = \frac{\sum_i m_i C_{p,i}}{hS} \frac{dT}{T_{\mathrm{max}} - T_{\mathrm{sur}}} \tag{A.8}$$

And with integration, it gives:

$$t = -\frac{\sum_i m_i C_{p,i}}{hS} \ln\left(\frac{T - T_{\mathrm{sur}}}{T_{\mathrm{max}} - T_{\mathrm{sur}}}\right) \tag{A.9}$$

The system time constant is defined as:

$$\tau_s = \frac{\sum_i m_i C_{p,i}}{hS} \tag{A.10}$$

The term τ_s is determined by the linear regression of the time versus the negative natural logarithm of θ, which is defined as:

$$\theta = \frac{T - T_{\text{sur}}}{T_{\text{max}} - T_{\text{sur}}} \tag{A.11}$$

Thus, the time is defined as:

$$t = -\tau_s \ln(\theta) \tag{A.12}$$

The term hS is determined by measuring the rate of temperature drop when the laser is off, then:

$$Q_{\text{sys}} = hS(T_{\text{max, water}} - T_{\text{sur}}) \tag{A.13}$$

Thus, the photothermal conversion efficiency (PCE) is defined as:

$$\eta = \frac{(hS(T_{\text{max}} - T_{\text{sur}}) - Q_{\text{diss}})}{I(1 - 10^{-A_{808}})} \tag{A.14}$$

where T_{sur} is the ambient room temperature, T_{max} is the equilibrium temperature, Q_{diss} is the energy input by the aqueous solution and the sample cell without the nanoparticles, h is the heat-transfer coefficient, S is the surface area for radiative heat transfer, I is the laser power (2 W/cm^2 at a spot diameter of 5 mm), and A_λ is the optical density of the nanoparticle solution at the laser wavelength $\lambda = 808$ nm.

Table A.2. Experimental parameters associated with the calculation of the photothermal conversion efficiency of each tested sample.

Samples	T_{max} **(°C)**	τ_s **(s)**	η **(%)**
MWCNTs	41 ± 1	158 ± 1	29 ± 2
GNRs	45 ± 2	152 ± 2	37 ± 2
MWCNTs−GNRs	63 ± 3	140 ± 10	69 ± 6

(a) (b)

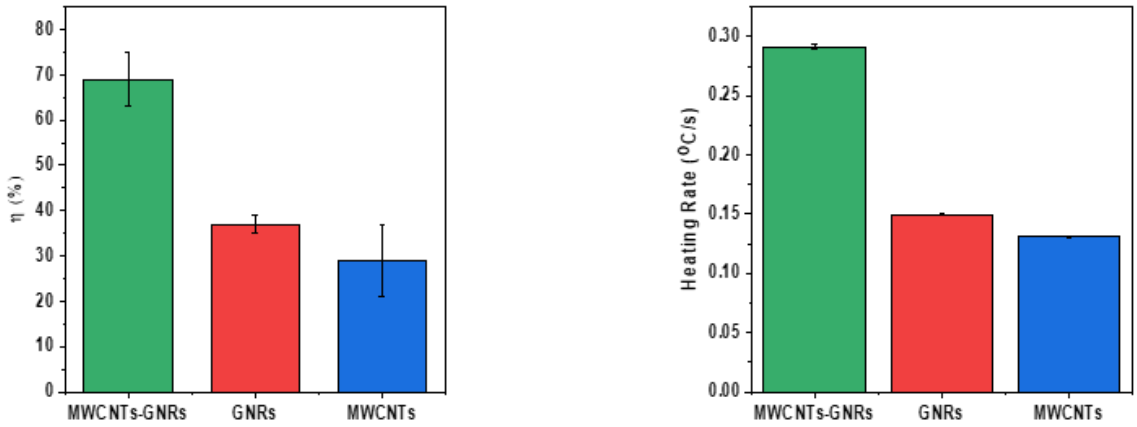

Fig. A.7. (a) Photothermal conversion efficiency and (b) heating rate (°C/s) of MWCNTs−GNRs, MWCNTs, and GNRs, exposed at 2 W/cm^2 for 300 s heating and cooling down for 300 s.

A.7 Photothermal Conversion Efficiency Per Unit Mass of MWCNTs

Dilution Factor (DF) is defined as the ratio of the absorption of decorated MWCNTs at 250 nm to the absorption of bare MWCNTs at 250 nm:

$$DF = \frac{A_{250\text{nm,MWCNT-GNR}}}{A_{250\text{nm,MWCNT}}} = \frac{3.41}{6.29} = 0.542 \tag{A.15}$$

Since hybridization with MWCNTs does not modify absorption at 250 nm, one can use DF to determine the final concentration of MWCNTs in the as-prepared hybrid composite:

$$DF = \frac{C_{f\ \text{MWCNT}}}{C_{i,\text{MWCNT}}} = \frac{C_{f\ \text{MWCNT}}}{0.1\,\text{g/mL}} \tag{A.16}$$

where $C_{f\ \text{MWCNT}}$ is 50.42 μg/ml. The mass of MWCNT is involved in the photothermal process by dividing the PCE by the mass of MWCNT present in each sample solution; thus, one will obtain the PCE per unit mass of MWCNT. This represents the efficiency of photothermal conversion with respect to the mass of MWCNT in the near-infrared region:

$$\text{PCE}_m = \frac{\text{PCE}}{m_{\text{MWCNT}}}\ [\text{a.u./g}] \tag{A.17}$$

The hybrid enhancement factor is calculated as the ratio of PCE per unit mass of MWCNTs−GNRs to PCE per unit mass of bare MWCNTs:

$$\text{Hybrid Enhancement Factor} = \frac{\text{PCE}_m(\text{MWCNTs}-\text{GNRs})}{\text{PCE}_m(\text{MWCNTs})} \tag{A.18}$$

Therefore, the PCE_m of MWCNTs−GNRs is approximately 4.9 times greater than bare MWCNT.

Table A.3. Experimental parameters associated with PCE per unit MWCNT mass at 808 nm.

Samples	**MWCNT mass per 100 μl volume**	**PCE [a.u.] at 808 nm**	**PCE per unit MWCNT mass [a.u./g] at 808 nm**
MWCNTs	0.01 g	0.28	28
MWCNTs−GNRs	0.005 g	0.69	138

A.8 Cell Viability of PC3 Cells Incubated with Different Nanostrcutures

Cell viability of PC3 cells incubated with MWCNTs−GNRs over several days, and cell viability of PC3 cells irradiated with MWCNTs−GNRs, GNRs, and MWCNTs.

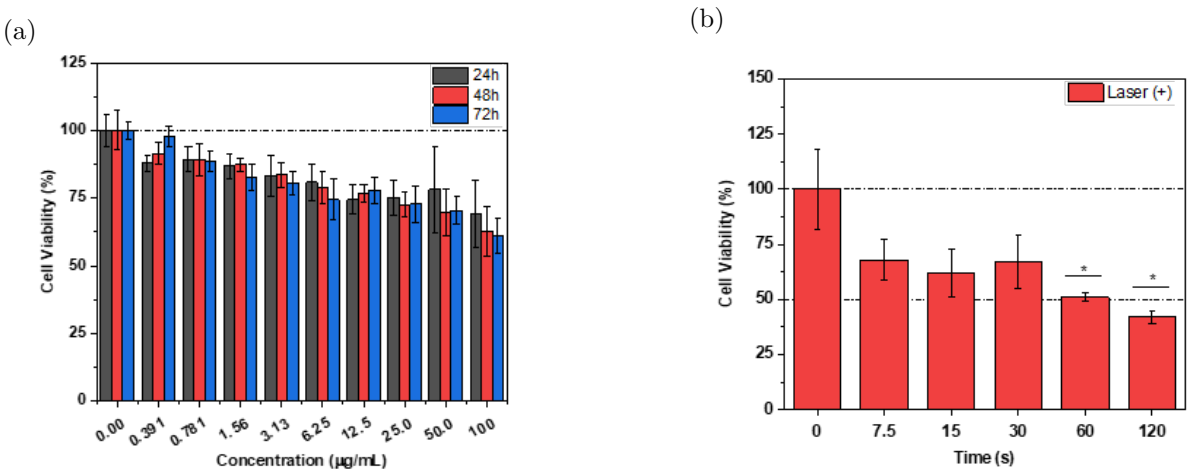

Fig. A.8. (a) The relative viability of PC3 cells incubated with different concentrations of MWCNTs−GNRs after 24, 48, and 72 hours of incubation. (b) The relative viability of PC3 cells incubated with MWCNTs−GNRs and exposed at different irradiation times. A two−paired student t−test was used to evaluate the statistical significance; * = $p < 0.05$.

A.9 Fluorescent Imaging of PC3 Cells Incubated with Different Nanostrcutures

Fluorescent staining of cells with calcein AM to assess PC3 cell viability mixed with MWCNTs−GNRs, GNRs, and MWCNTs.

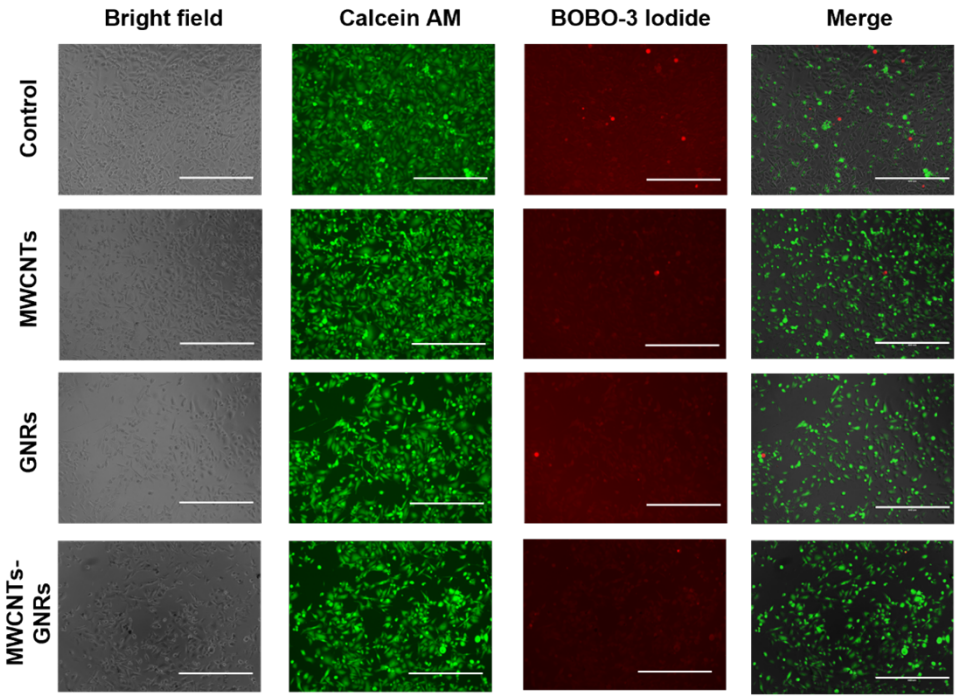

Fig. A.9. Fluorescence images of unexposed PC3 cells incubated for 24h with MWCNTs, GNRs, MWCNTs−GNRs. Fluorescence images of Calcein AM (green fluorescence, live cells), BOBO−3 Iodide (red fluorescence, dead cells). Scale bars 400 µm.

A.10 Photothermal Conversion Efficiency of Several Carbon−Based PTT Agents

Table A.4. Photothermal conversion efficiency (η) of several carbon−based PTT agents.

PTT agents	η (%)	**Experimental conditions**	**References**
MWCNTs−GNRs	69	2 W/cm^2 at 808 nm	Our work
CNTs−GNPs (Rings)	61	0.5 W/cm^2 at 808 nm	[148]
CNTs−GNPs	76	0.5 W/cm^2 at 808 nm	[148]
CNTs−GNSs	−	1 W/cm^2 at 808 nm	[141]
CNTs−PAMAM−Ag	21	0.2 W at 980 nm	[138]
Carbon spheres	54.2	1 W/cm^2 at 808 nm	[255]

A.11 Estimation of GNRs Concentration

To calculate the concentration of GNR using Gan's theory at 808 nm [210]:

$$C_{\text{GNR}} = N_{\text{GNR}} = 2 \times \frac{\sigma_{808\text{nm}}}{C_{\text{abs}} \times l} \tag{A.19}$$

$$C_{\text{GNR}} = N_{\text{GNR}} = 2.13 \times 10^{14} \text{ nanoparticles/mL} \tag{A.20}$$

where C_{GNR} is the concentration of GNRs [nanoparticles/mL] equal to N_{GNR}, defined as the number concentration of nanoparticles in unit of particles/mL, $\sigma_{808\text{nm}}$ is the measured optical absorption at 808 nm [a.u.], which is 1.859, C_{abs} is the extracted absorption cross-section [m^{-2}] of GNRs, which is 1.74×10^{-15} m^{-2}, and l is the cuvette path length [cm], which is 1 cm.

Nanoparticle concentration in molar concentration (molarity):

$$M = \frac{N_{\text{GNR}}}{6.02 \times 10^{23}} \tag{A.21}$$

where N_{GNR} is the number concentration of nanoparticles in units of particles/mL, and the denominator is Avogadro's number.

1) The estimated molarity of GNRs from the measurement of absorption at the longitudinal resonance (i.e., 808 nm) is

$$M = 3.54 \times 10^{-10} \text{ mol/L} = 35.4 \text{ nM} \tag{A.22}$$

2) The estimated molarity of GNRs from measurement at the transverse resonance (i.e., 510 nm) is

$$M = 5.65 \times 10^{-10} \text{ mol/L} = 56.5 \text{ nM} \tag{A.23}$$

A.12 MATLAB Codes

```
%%%%%%%%%%%%% G Stokes %%%%%%%%%%%%
data1= readtable('G_1580_Data_0_air');

%transfomr your table into a matrix for mapping
pixelMap1 = table2array(data1);

% Create a new matrix for the smoothed image
smoothedMap1 = zeros(size(pixelMap1));

% Define the neighborhood size (3x3 neighborhood)
neighborhoodSize = 3;

% Iterate through the pixel map and calculate the average of
   the neighborhood
for i = 1:size(pixelMap1, 1)
    for j = 1:size(pixelMap1, 2)
        % Define the neighborhood boundaries
        rowStart = max(1, i - floor(neighborhoodSize / 2));
        rowEnd = min(size(pixelMap1, 1), i + floor(
           neighborhoodSize / 2));
        colStart = max(1, j - floor(neighborhoodSize / 2));
        colEnd = min(size(pixelMap1, 2), j + floor(
           neighborhoodSize / 2));

        % Extract the neighborhood from the original image
        neighborhood = pixelMap1(rowStart:rowEnd, colStart:
           colEnd);
```

```
        % Calculate the average value of the neighborhood
        averageValue = mean(neighborhood(:));

        % Assign the average value to the corresponding pixel
           in the smoothed image
        smoothedMap1(i, j) = averageValue;
    end
end

%%%%%%%%%% G Anti-Stokes %%%%%%%%%
data2= readtable('G_1580_AS_Data_0_air');

%transfomr your table into a matrix for mapping
pixelMap2 = table2array(data2);

% Create a new matrix for the smoothed image
smoothedMap2 = zeros(size(pixelMap2));

% Define the neighborhood size ( 3x3 neighborhood)
neighborhoodSize = 3;

% Iterate through the pixel map and calculate the average of
   the neighborhood
for i = 1:size(pixelMap2, 1)
    for j = 1:size(pixelMap2, 2)
        % Define the neighborhood boundaries
        rowStart = max(1, i - floor(neighborhoodSize / 2));
        rowEnd = min(size(pixelMap2, 1), i + floor(
           neighborhoodSize / 2));
        colStart = max(1, j - floor(neighborhoodSize / 2));
        colEnd = min(size(pixelMap2, 2), j + floor(
```

```
            neighborhoodSize / 2));

        % Extract the neighborhood from the original image
        neighborhood = pixelMap2(rowStart:rowEnd, colStart:
            colEnd);

        % Calculate the average value of the neighborhood
        averageValue = mean(neighborhood(:));

        % Assign the average value to the corresponding pixel
            in the smoothed image
        smoothedMap2(i, j) = averageValue;
    end
end

%%%%%%%%%%%% Ratio AS/S %%%%%%%%%%%%%%%
ratio_matrix = pixelMap2./pixelMap1;

% Create a new matrix for the smoothed image
smoothedMap3 = zeros(size(ratio_matrix));

% Define the neighborhood size ( 3x3 neighborhood)
neighborhoodSize = 3;

% Iterate through the pixel map and calculate the average of
   the neighborhood
for i = 1:size(ratio_matrix, 1)
    for j = 1:size(ratio_matrix, 2)
        % Define the neighborhood boundaries
        rowStart = max(1, i - floor(neighborhoodSize / 2));
        rowEnd = min(size(ratio_matrix, 1), i + floor(
```

```
            neighborhoodSize / 2));
        colStart = max(1, j - floor(neighborhoodSize / 2));
        colEnd = min(size(ratio_matrix, 2), j + floor(
            neighborhoodSize / 2));

        % Extract the neighborhood from the original image
        neighborhood = ratio_matrix(rowStart:rowEnd, colStart:
            colEnd);

        % Calculate the average value of the neighborhood
        averageValue = mean(neighborhood(:));

        % Assign the average value to the corresponding pixel
            in the smoothed image
        smoothedMap3(i, j) = averageValue;
    end
end

%%%%%%%%%% Temperature (K) %%%%%%%
h=6.6261*10^-34;                %planck constant [Js]
Kb= 1.28*10^-23;                % Boltzmann constant [J/k]?
Ti= 293;                        % Temperature in Kelvin [K] for
   20oC
c=299792458;                    %speed of light     [m/s]
omega_l= c/(633*(10^(-9)))      % laser frequency [s] for 633nm
omega_ph=c/((10^7)/1580*10^-9);%frequency of Raman mode 1580 /
   cm
omega_as = (omega_l+omega_ph)^3;% Frequency shift (anti-Stokes)
omega_s=(omega_l-omega_ph)^3;   % Frequency shift (Stokes)

% calculated resonnance factor due the the material in cellular
```

```
    environment
R = 13.75;          % resonnance factor

%Calculate the temperature based on the ratio in Kelvin units
Tf= (h*omega_ph/Kb)*(1./(3*log(omega_as/omega_s)-log(
   smoothedMap3./R)));

% Create a new matrix for the smoothed image
smoothedMap4 = zeros(size(Tf));

% Define the neighborhood size (for example, a 3x3 neighborhood
   )
neighborhoodSize = 3;

% Iterate through the pixel map and calculate the average of
   the neighborhood
for i = 1:size(Tf, 1)
    for j = 1:size(Tf, 2)
        % Define the neighborhood boundaries
        rowStart = max(1, i - floor(neighborhoodSize / 2));
        rowEnd = min(size(Tf, 1), i + floor(neighborhoodSize /
           2));
        colStart = max(1, j - floor(neighborhoodSize / 2));
        colEnd = min(size(Tf, 2), j + floor(neighborhoodSize /
           2));

        % Extract the neighborhood from the original image
        neighborhood = Tf(rowStart:rowEnd, colStart:colEnd);

        % Calculate the average value of the neighborhood
        averageValue = mean(neighborhood(:));
```

```
        % Assign the average value to the corresponding pixel
           in the smoothed image
        smoothedMap4(i, j) = averageValue;
    end
end

%%%%%%%%%%%%%%%%%%%%%%%%%%%%%%%%%%%%%%%%%%%%%%%%%%%%%%%%%%%%
% Define the symbolic variables
syms Ias Is h omega_ph Kb R omega_as omega_s

h=6.6261*10^-34;                %planck constant [Js]
Kb= 1.28*10^-23;                % Boltzmann constant [J/k]?
Ti= 293;                        % Temperature in Kelvin [K] for
   20oC RT
c=299792458;                    %speed of light     [m/s]
omega_l= c/(633*(10^(-9)));     % laser frequency [s] for 633nm
omega_ph=c/((10^7)/1580*10^-9);%frequency of Raman mode 1580 /
   cm
omega_as = (omega_l+omega_ph)^3;% Frequency shift
omega_s=(omega_l-omega_ph)^3;

% calculated resonnance factor due the the material in cellular
    environment
R = 13.75;          % resonnance factor R = 13.75 in air

Ias = smoothedMap2;
Is =  smoothedMap1;

% Define the standard deviations (assuming they are the same
   for all elements)
```

```
values = [0.2206, 0.23011, 0.1978];

% Calculate the mean
mean_value = mean(values);

sigma_Ias = mean_value;  %single standard deviation for all
   elements in Ias
sigma_Is = mean_value;  %single standard deviation for all
   elements in Is

Tf_eq = (h * omega_ph / Kb) * (1./(3*log(omega_as/omega_s) -
   log((Ias./Is)./R)));

% Compute the partial derivative with respect to Is
DTf_DIs= gradient(Tf_eq(:), Is(:));
DTf_DIs= reshape(DTf_DIs, size(Is));
partial_derivative_Is = DTf_DIs;

% Compute the partial derivative with respect to Is
DTf_DIas= gradient(Tf_eq(:), Ias(:));
DTf_DIas= reshape(DTf_DIas, size(Ias));
partial_derivative_Ias = DTf_DIas;

% Calculate the standard deviation of Tf using the propagation
   of uncertainty formula
sigma_Tf = sqrt((partial_derivative_Ias.* sigma_Ias).^2 + (
   partial_derivative_Is.* sigma_Is).^2);

relative_error = sigma_Tf./Tf_eq;
```

```
%%%%%%%%%%%%%% Figures %%%%%%%%%%%%%%%%%%%
% Display the original and smoothed images for both maps
figure;
ax = gca;
ax.FontSize = 12;
imagesc(smoothedMap1);
colormap("jet");  % Choose a colormap (e.g., jet)
h = colorbar; % Add a colorbar to the plot
h.Label.String = "Stokes Intensity (CCD cts)";
h.Label.Rotation = 270;
h.Label.VerticalAlignment = "bottom";
h.Label.FontSize = 10;
xlabel('Pixel number');
ylabel('Pixel number');

figure;
imagesc(smoothedMap2);
colormap("jet");  % Choose a colormap (e.g., jet)
h = colorbar; % Add a colorbar to the plot
h.Label.String = "Anti-Stokes Intensity (CCD cts)";
h.Label.Rotation = 270;
h.Label.VerticalAlignment = "bottom";
h.Label.FontSize = 10;
xlabel('Pixel number');
ylabel('Pixel number');

figure;
imagesc(smoothedMap3);
colormap("jet");  % Choose a colormap (e.g., jet)
h = colorbar; % Add a colorbar to the plot
h.Label.String = "Ratio I_{AS}/I_{S}";
```

```
h.Label.Rotation = 270;
h.Label.VerticalAlignment = "bottom";
h.Label.FontSize = 10;
xlabel('Pixel number');
ylabel('Pixel number');

figure;
imagesc(smoothedMap4);
colormap("jet");  % Choose a colormap (e.g., jet)
h = colorbar; % Add a colorbar to the plot
h.Label.String = "Temperature (K)";
h.Label.Rotation = 270;
h.Label.VerticalAlignment = "bottom";
h.Label.FontSize = 10;
xlabel('Pixel number');
ylabel('Pixel number');
```

Bibliography

[1] R. Weissleder, A clearer vision for in vivo imaging, Nat Biotechnol 19 (2001) 316–7. doi:10.1038/86684.

[2] L. M. Maestro, P. Haro-Gonzalez, B. del Rosal, J. Ramiro, A. J. Caamano, E. Carrasco, A. Juarranz, F. Sanz-Rodriguez, J. G. Sole, D. Jaque, Heating efficiency of multi-walled carbon nanotubes in the first and second biological windows, Nanoscale 5 (2013) 7882–9. doi:10.1039/c3nr01398g.

[3] Biophotonics, 2016. doi:10.1007/978-981-10-0945-7.

[4] S. K. Calderwood, Hyperthermia, the Tumor Microenvironment and Immunity, 2013, pp. 29–37. doi:10.1007/978-94-007-4694-7_2.

[5] A. S. Song, A. M. Najjar, K. R. Diller, Thermally induced apoptosis, necrosis, and heat shock protein expression in 3d culture, J Biomech Eng 136 (2014). doi:10.1115/1.4027272.

[6] C. Vilches, R. Quidant, Targeted hyperthermia with plasmonic nanoparticles, Frontiers of Nanoscience, 2020, pp. 307–352. doi:10.1016/b978-0-08-102828-5.00012-7.

[7] A. C. Society, Facts Figures 2023, Report, American Cancer Society, 2023.

[8] M. J. Connor, M. A. Gorin, H. U. Ahmed, R. Nigam, Focal therapy for localized prostate cancer in the era of routine multi-parametric mri, Prostate Cancer Prostatic Dis 23 (2020) 232–243. doi:10.1038/s41391-020-0206-6.

[9] M. Perera, N. Krishnananthan, U. Lindner, N. Lawrentschuk, An update on focal therapy for prostate cancer, Nat Rev Urol 13 (2016) 641–653. doi:10.1038/nrurol.2016.177.

[10] D. Cantarero-Prieto, J. Lera, P. Lanza-Leon, M. Barreda-Gutierrez, V. Guillem-Porta, L. Castelo-Branco, J. M. Martin-Moreno, The economic burden of localized prostate cancer and insights derived from cost-effectiveness studies of the different treatments, Cancers (Basel) 14 (2022). doi:10.3390/cancers14174088.

[11] M. Valerio, H. U. Ahmed, M. Emberton, Focal therapy of prostate cancer using irreversible electroporation, Tech Vasc Interv Radiol 18 (2015) 147–52. doi:10.1053/j.tvir.2015.06.005.

[12] G. Jindal, M. Friedman, J. Locklin, B. J. Wood, Palliative radiofrequency ablation for recurrent prostate cancer, Cardiovasc Intervent Radiol 29 (2006) 482–5. doi:10.1007/s00270-004-0200-8.

[13] H. Kunogi, Y. Wakumoto, T. Kawamoto, M. Oshima, S. Horie, K. Sasai, Focal low-dose-rate prostate brachytherapy for low- and intermediate-risk prostate cancer, J Contemp Brachytherapy 12 (2020) 554–561. doi:10.5114/jcb.2020.101688.

[14] J. M. Phillips, S. Catarinicchia, K. Krughoff, A. B. Barqawi, Cryotherapy in prostate cancer, Journal of Clinical Urology 7 (2014) 308–317. doi:10.1177/2051415814521806.

[15] H. Sun, Q. Zhang, J. Li, S. Peng, X. Wang, R. Cai, Near-infrared photoactivated nanomedicines for photothermal synergistic cancer therapy, Nano Today 37 (2021). doi:10.1016/j.nantod.2020.101073.

[16] A. Wicki, D. Witzigmann, V. Balasubramanian, J. Huwyler, Nanomedicine in cancer therapy: challenges, opportunities, and clinical applications, J Control Release 200 (2015) 138–57. doi:10.1016/j.jconrel.2014.12.030.

[17] H. U. Ahmed, A. Freeman, A. Kirkham, M. Sahu, R. Scott, C. Allen, J. Van der Meulen, M. Emberton, Focal therapy for localized prostate cancer: a phase i/ii trial, J Urol 185 (2011) 1246–54. doi:10.1016/j.juro.2010.11.079.

[18] J. Chen, C. Ning, Z. Zhou, P. Yu, Y. Zhu, G. Tan, C. Mao, Nanomaterials as photothermal therapeutic agents, Prog Mater Sci 99 (2019) 1–26. doi:10.1016/j.pmatsci.2018.07.005.

[19] X. Huang, P. K. Jain, I. H. El-Sayed, M. A. El-Sayed, Plasmonic photothermal therapy (pptt) using gold nanoparticles, Lasers Med Sci 23 (2008) 217–28. doi:10.1007/s10103-007-0470-x.

[20] M. Kim, J. H. Lee, J. M. Nam, Plasmonic photothermal nanoparticles for biomedical applications, Adv Sci (Weinh) 6 (2019) 1900471. doi:10.1002/advs.201900471.

[21] A. R. Rastinehad, H. Anastos, E. Wajswol, J. S. Winoker, J. P. Sfakianos, S. K. Doppalapudi, M. R. Carrick, C. J. Knauer, B. Taouli, S. C. Lewis, A. K. Tewari, J. A. Schwartz, S. E. Canfield, A. K. George, J. L. West, N. J. Halas, Gold nanoshell-localized photothermal ablation of prostate tumors in a clinical pilot device study, Proc Natl Acad Sci U S A 116 (2019) 18590–18596. doi:10.1073/pnas.1906929116.

[22] A. C. Society, Cancer Facts Figures 2023, Report, 2023.

[23] R. L. Siegel, K. D. Miller, N. S. Wagle, A. Jemal, Cancer statistics, 2023, CA Cancer J Clin 73 (2023) 17–48. doi:10.3322/caac.21763.

[24] V. Y. T. Cheung, High-intensity focused ultrasound therapy, Best Pract Res Clin Obstet Gynaecol 46 (2018) 74–83. doi:10.1016/j.bpobgyn.2017.09.002.

[25] H. Takahashi, B. Kahramangil, E. Kose, E. Berber, A comparison of microwave thermosphere versus radiofrequency thermal ablation in the treatment of colorectal liver metastases, HPB (Oxford) 20 (2018) 1157–1162. doi:10.1016/j.hpb.2018.05.012.

[26] S. Pang, A. Kapur, K. Zhou, P. Anastasiadis, N. Ballirano, A. J. Kim, J. A. Winkles, G. F. Woodworth, H. C. Huang, Nanoparticle-assisted, image-guided laser interstitial thermal therapy for cancer treatment, Wiley Interdiscip Rev Nanomed Nanobiotechnol 14 (2022) e1826. doi:10.1002/wnan.1826.

[27] D. Hanahan, R. A. Weinberg, Hallmarks of cancer: the next generation, Cell 144 (2011) 646–74. doi:10.1016/j.cell.2011.02.013.

[28] Y. Gong, Z. Fan, G. Luo, C. Yang, Q. Huang, K. Fan, H. Cheng, K. Jin, Q. Ni, X. Yu, C. Liu, The role of necroptosis in cancer biology and therapy, Mol Cancer 18 (2019) 100. doi:10.1186/s12943-019-1029-8.

[29] M. R. Ali, H. R. Ali, C. R. Rankin, M. A. El-Sayed, Targeting heat shock protein 70 using gold nanorods enhances cancer cell apoptosis in low dose plasmonic photothermal therapy, Biomaterials 102 (2016) 1–8. doi:10.1016/j.biomaterials.2016.06.017.

[30] M. H. Niemz, Laser-Tissue Interactions, 2019. doi:10.1007/978-3-030-11917-1.

[31] T. Vo-Dinh, Biomedical Photonics Handbook, 2003. doi:10.1201/9780203008997.

[32] R. Narayan, Encyclopedia of Biomedical Engineering, Elsevier Science, 2018. URL: https://books.google.ca/books?id=ZORyDwAAQBAJ.

[33] A. Marcos-Vidal, J. J. Vaquero, J. Ripoll, Optical Properties of Tissues in the Near Infrared: Their Relevance for Optical Bioimaging, Springer International Publishing, 2020, pp. 1–20. doi:10.1007/978-3-030-32036-2_1.

[34] P. Agostinis, K. Berg, K. A. Cengel, T. H. Foster, A. W. Girotti, S. O. Gollnick, S. M. Hahn, M. R. Hamblin, A. Juzeniene, D. Kessel, M. Korbelik, J. Moan, P. Mroz, D. Nowis, J. Piette, B. C. Wilson, J. Golab, Photodynamic therapy of cancer: an update, CA Cancer J Clin 61 (2011) 250–81. doi:10.3322/caac.20114.

[35] R. R. Allison, Photodynamic therapy: oncologic horizons, Future Oncol 10 (2014) 123–4. doi:10.2217/fon.13.176.

[36] R. Baskaran, J. Lee, S. G. Yang, Clinical development of photodynamic agents and therapeutic applications, Biomater Res 22 (2018) 25. doi:10.1186/s40824-018-0140-z.

[37] S. Gai, G. Yang, P. Yang, F. He, J. Lin, D. Jin, B. Xing, Recent advances in functional nanomaterials for light–triggered cancer therapy, Nano Today 19 (2018) 146–187. doi:10.1016/j.nantod.2018.02.010.

[38] Y. H. Cheng, C. He, J. E. Riviere, N. A. Monteiro-Riviere, Z. Lin, Meta-analysis of nanoparticle delivery to tumors using a physiologically based pharmacokinetic modeling

and simulation approach, ACS Nano 14 (2020) 3075–3095. doi:10.1021/acsnano.9b08142.

[39] Y. Shi, R. van der Meel, X. Chen, T. Lammers, The epr effect and beyond: Strategies to improve tumor targeting and cancer nanomedicine treatment efficacy, Theranostics 10 (2020) 7921–7924. doi:10.7150/thno.49577.

[40] A. L. Oei, L. E. Vriend, J. Crezee, N. A. Franken, P. M. Krawczyk, Effects of hyperthermia on dna repair pathways: one treatment to inhibit them all, Radiat Oncol 10 (2015) 165. doi:10.1186/s13014-015-0462-0.

[41] S. Lee, B. Son, G. Park, H. Kim, H. Kang, J. Jeon, H. Youn, B. Youn, Immunogenic effect of hyperthermia on enhancing radiotherapeutic efficacy, Int J Mol Sci 19 (2018). doi:10.3390/ijms19092795.

[42] J.-M. JIN, The Finite Element Method in Electromagnetics, 2nd edition ed., WILEY, New York, 2002.

[43] Z. J. Coppens, W. Li, D. G. Walker, J. G. Valentine, Probing and controlling photothermal heat generation in plasmonic nanostructures, Nano Lett 13 (2013) 1023–8. doi:10.1021/nl304208s.

[44] Y. Kane, Numerical solution of initial boundary value problems involving maxwell's equations in isotropic media, IEEE Transactions on Antennas and Propagation 14 (1966) 302–307. doi:10.1109/tap.1966.1138693.

[45] C. Oubre, P. Nordlander, Optical properties of metallodielectric nanostructures calculated using the finite difference time domain method, The Journal of Physical Chemistry B 108 (2004) 17740–17747. doi:10.1021/jp0473164.

[46] J. Zhao, A. O. Pinchuk, J. M. McMahon, S. Li, L. K. Ausman, A. L. Atkinson, G. C. Schatz, Methods for describing the electromagnetic properties of silver and gold nanoparticles, Acc Chem Res 41 (2008) 1710–20. doi:10.1021/ar800028j.

[47] C. Zhou, L. Zhang, T. Sun, Y. Zhang, Y. Liu, M. Gong, Z. Xu, M. Du, Y. Liu, G. Liu, D. Zhang, Activatable nir-ii plasmonic nanotheranostics for efficient photoacoustic imaging and photothermal cancer therapy, Adv Mater 33 (2021) e2006532. doi:10.1002/adma.202006532.

[48] B. T. Draine, P. J. Flatau, Discrete-dipole approximation for scattering calculations, Journal of the Optical Society of America a-Optics Image Science and Vision 11 (1994) 1491–1499. doi:Doi10.1364/Josaa.11.001491.

[49] R. Q. Guillaume Baffou, C. Girard, Thermoplasmonics modeling: A green's function approach, Phys. Rev. B (2012). doi:https://doi-org/10.1103/PhysRevB.82.165424.

[50] Z. Qin, Y. Wang, J. Randrianalisoa, V. Raeesi, W. C. Chan, W. Lipinski, J. C. Bischof, Quantitative comparison of photothermal heat generation between gold nanospheres and nanorods, Sci Rep 6 (2016) 29836. doi:10.1038/srep29836.

[51] W. W. Gärtner, Photothermal effect in semiconductors, Physical Review 122 (1961) 419–424. doi:10.1103/PhysRev.122.419.

[52] Y. Wang, H.-M. Meng, G. Song, Z. Li, X.-B. Zhang, Conjugated-polymer-based nanomaterials for photothermal therapy, ACS Applied Polymer Materials 2 (2020) 4258–4272. doi:10.1021/acsapm.0c00680.

[53] J. Chen, Z. Ye, F. Yang, Y. Yin, Plasmonic nanostructures for photothermal conversion, Small Science 1 (2021). doi:10.1002/smsc.202000055.

[54] H. H. Richardson, M. T. Carlson, P. J. Tandler, P. Hernandez, A. O. Govorov, Experimental and theoretical studies of light-to-heat conversion and collective heating effects in metal nanoparticle solutions, Nano Lett 9 (2009) 1139–46. doi:10.1021/nl8036905.

[55] D. K. Roper, W. Ahn, M. Hoepfner, Microscale heat transfer transduced by surface plasmon resonant gold nanoparticles, J Phys Chem C Nanomater Interfaces 111 (2007) 3636–3641. doi:10.1021/jp064341w.

[56] X. He, J. C. Bischof, Quantification of temperature and injury response in thermal therapy and cryosurgery, Crit Rev Biomed Eng 31 (2003) 355–422. doi:10.1615/critrevbiomedeng.v31.i56.10.

[57] X. Huang, P. K. Jain, I. H. El-Sayed, M. A. El-Sayed, Determination of the minimum temperature required for selective photothermal destruction of cancer cells with the use of immunotargeted gold nanoparticles, Photochem Photobiol 82 (2006) 412–7. doi:10.1562/2005-12-14-RA-754.

[58] D. Incropera, F; Dewitt, Introduction to heat transfer, Incropera, F, and Dewitt, D. Introduction to heat transfer. United States: N. p., 1985., ????

[59] T. Guo, Q. Tang, Y. Guo, H. Qiu, J. Dai, C. Xing, S. Zhuang, G. Huang, Boron quantum dots for photoacoustic imaging-guided photothermal therapy, ACS Appl Mater Interfaces 13 (2021) 306–311. doi:10.1021/acsami.0c21198.

[60] J. Estelrich, M. A. Busquets, Iron oxide nanoparticles in photothermal therapy, Molecules 23 (2018). doi:10.3390/molecules23071567.

[61] B. McCarthy, A. Cudykier, R. Singh, N. Levi-Polyachenko, S. Soker, Semiconducting polymer nanoparticles for photothermal ablation of colorectal cancer organoids, Sci Rep 11 (2021) 1532. doi:10.1038/s41598-021-81122-w.

[62] B. N. Eldridge, B. W. Bernish, C. D. Fahrenholtz, R. Singh, Photothermal therapy of glioblastoma multiforme using multiwalled carbon nanotubes optimized for diffusion in extracellular space, ACS Biomater Sci Eng 2 (2016) 963–976. doi:10.1021/acsbiomaterials.6b00052.

[63] S. S. Lee, P. J. Roche, P. N. Giannopoulos, E. J. Mitmaker, M. Tamilia, M. Paliouras, M. A. Trifiro, Prostate-specific membrane antigen-directed nanoparticle targeting for extreme nearfield ablation of prostate cancer cells, Tumour Biol 39 (2017) 1010428317695943. doi:10.1177/1010428317695943.

[64] C. Huang, X. Hu, Z. Hou, J. Ji, Z. Li, Y. Luan, Tailored graphene oxide-doxorubicin nanovehicles via near-infrared dye-lactobionic acid conjugates for chemo-photothermal therapy, J Colloid Interface Sci 545 (2019) 172–183. doi:10.1016/j.jcis.2019.03.019.

[65] J. H. Lim, D. E. Kim, E.-J. Kim, C. D. Ahrberg, B. G. Chung, Functional graphene oxide-based nanosheets for photothermal therapy, Macromolecular Research 26 (2018) 557–565. doi:10.1007/s13233-018-6067-3.

[66] M. Xie, F. Zhang, H. Peng, Y. Zhang, Y. Li, Y. Xu, J. Xie, Layer-by-layer modification of magnetic graphene oxide by chitosan and sodium alginate with enhanced dispersibility for targeted drug delivery and photothermal therapy, Colloids Surf B Biointerfaces 176 (2019) 462–470. doi:10.1016/j.colsurfb.2019.01.028.

[67] Y. Li, G. Bai, S. Zeng, J. Hao, Theranostic carbon dots with innovative nir-ii emission for in vivo renal-excreted optical imaging and photothermal therapy, ACS Appl Mater Interfaces 11 (2019) 4737–4744. doi:10.1021/acsami.8b14877.

[68] E. Miyako, T. Deguchi, Y. Nakajima, M. Yudasaka, Y. Hagihara, M. Horie, M. Shichiri, Y. Higuchi, F. Yamashita, M. Hashida, Y. Shigeri, Y. Yoshida, S. Iijima, Photothermic regulation of gene expression triggered by laser-induced carbon nanohorns, Proc Natl Acad Sci U S A 109 (2012) 7523–8. doi:10.1073/pnas.1204391109.

[69] Z. Chen, L. Ma, Y. Liu, C. Chen, Applications of functionalized fullerenes in tumor theranostics, Theranostics 2 (2012) 238–50. doi:10.7150/thno.3509.

[70] A. M. Gobin, D. P. O'Neal, D. M. Watkins, N. J. Halas, R. A. Drezek, J. L. West, Near infrared laser-tissue welding using nanoshells as an exogenous absorber, Lasers Surg Med 37 (2005) 123–9. doi:10.1002/lsm.20206.

[71] L. R. Hirsch, R. J. Stafford, J. A. Bankson, S. R. Sershen, B. Rivera, R. E. Price, J. D. Hazle, N. J. Halas, J. L. West, Nanoshell-mediated near-infrared thermal therapy of tumors under magnetic resonance guidance, Proc Natl Acad Sci U S A 100 (2003) 13549–54. doi:10.1073/pnas.2232479100.

[72] D. P. O'Neal, L. R. Hirsch, N. J. Halas, J. D. Payne, J. L. West, Photo-thermal tumor ablation in mice using near infrared-absorbing nanoparticles, Cancer Lett 209 (2004) 171–6. doi:10.1016/j.canlet.2004.02.004.

[73] Y. S. Chen, Y. Zhao, S. J. Yoon, S. S. Gambhir, S. Emelianov, Miniature gold nanorods for photoacoustic molecular imaging in the second near-infrared optical window, Nat Nanotechnol 14 (2019) 465–472. doi:10.1038/s41565-019-0392-3.

[74] Y. Wang, K. C. Black, H. Luehmann, W. Li, Y. Zhang, X. Cai, D. Wan, S. Y. Liu, M. Li, P. Kim, Z. Y. Li, L. V. Wang, Y. Liu, Y. Xia, Comparison study of gold nanohexapods, nanorods, and nanocages for photothermal cancer treatment, ACS Nano 7 (2013) 2068–77. doi:10.1021/nn304332s.

[75] C. Ayala-Orozco, C. Urban, M. W. Knight, A. S. Urban, O. Neumann, S. W. Bishnoi, S. Mukherjee, A. M. Goodman, H. Charron, T. Mitchell, M. Shea, R. Roy, S. Nanda, R. Schiff, N. J. Halas, A. Joshi, Au nanomatryoshkas as efficient near-infrared photothermal transducers for cancer treatment: Benchmarking against nanoshells, Acs Nano 8 (2014) 6372–6381. doi:10.1021/nn501871d.

[76] E. J. Comparetti, V. A. Pedrosa, R. Kaneno, Carbon nanotube as a tool for fighting cancer, Bioconjug Chem 29 (2018) 709–718. doi:10.1021/acs.bioconjchem.7b00563.

[77] S. Iijima, Helitical microtubules of graphitic carbon, NATURE 354 (1991).

[78] K. G.-R. P. M. A. Bachtold, M. de Jonge, Suppression of tunneling into multi-wall carbon nanotubes (2000).

[79] A. Grüneis, R. Saito, G. G. Samsonidze, T. Kimura, M. A. Pimenta, A. Jorio, A. G. S. Filho, G. Dresselhaus, M. S. Dresselhaus, Inhomogeneous optical absorption around thekpoint in graphite and carbon nanotubes, Physical Review B 67 (2003). doi:10.1103/PhysRevB.67.165402.

[80] A. M. Rao, A. Jorio, M. A. Pimenta, M. S. Dantas, R. Saito, G. Dresselhaus, M. S. Dresselhaus, Polarized raman study of aligned multiwalled carbon nanotubes, Phys Rev Lett 84 (2000) 1820–3. doi:10.1103/PhysRevLett.84.1820.

[81] Y. Wang, K. Kempa, B. Kimball, J. B. Carlson, G. Benham, W. Z. Li, T. Kempa, J. Rybczynski, A. Herczynski, Z. F. Ren, Receiving and transmitting light-like radio waves: Antenna effect in arrays of aligned carbon nanotubes, Applied Physics Letters 85 (2004) 2607–2609. doi:10.1063/1.1797559.

[82] Y. H. Yuan, R. C. Miao, J. T. Bai, X. Hou, Photoluminescence of multiwalled carbon nanotubes excited at different wavelengths, Chinese Physics 15 (2006) 2761–2764.

[83] M. S. Dresselhaus, G. Dresselhaus, A. Jorio, Unusual properties and structure of carbon nanotubes, Annual Review of Materials Research 34 (2004) 247–278. doi:10.1146/annurev.matsci.34.040203.114607.

[84] M. S. Dresselhaus, P. C. Eklund, Phonons in carbon nanotubes, Advances in Physics 49 (2000) 705–814. doi:10.1080/000187300413184.

[85] V. Meunier, A. ouza Filho, E. arros, M. resselhaus, Physical properties of low-dimensionalsp2-based carbon nanostructures, Reviews of Modern Physics 88 (2016). doi:10.1103/RevModPhys.88.025005.

[86] C. Fabbro, H. Ali-Boucetta, T. Da Ros, K. Kostarelos, A. Bianco, M. Prato, Targeting carbon nanotubes against cancer, Chem Commun (Camb) 48 (2012) 3911–26. doi:10.1039/c2cc17995d.

[87] M. Melchionna, M. Prato, Functionalizing carbon nanotubes: An indispensible step towards applications, ECS Journal of Solid State Science and Technology 2 (2013) M3040–M3045. doi:10.1149/2.008310jss.

[88] A. Burke, X. Ding, R. Singh, R. A. Kraft, N. Levi-Polyachenko, M. N. Rylander, C. Szot, C. Buchanan, J. Whitney, J. Fisher, H. C. Hatcher, J. D'Agostino, R., N. D. Kock, P. M. Ajayan, D. L. Carroll, S. Akman, F. M. Torti, S. V. Torti, Long-term survival following a single treatment of kidney tumors with multiwalled carbon nanotubes and near-infrared radiation, Proc Natl Acad Sci U S A 106 (2009) 12897–902. doi:10.1073/pnas.0905195106.

[89] J. W. Fisher, S. Sarkar, C. F. Buchanan, C. S. Szot, J. Whitney, H. C. Hatcher, S. V. Torti, C. G. Rylander, M. N. Rylander, Photothermal response of human and murine cancer cells to multiwalled carbon nanotubes after laser irradiation, Cancer Res 70 (2010) 9855–64. doi:10.1158/0008-5472.CAN-10-0250.

[90] S. V. Torti, F. Byrne, O. Whelan, N. Levi, B. Ucer, M. Schmid, F. M. Torti, S. Akman, J. Liu, P. M. Ajayan, O. Nalamasu, D. L. Carroll, Thermal ablation therapeutics based on cnx multi-walled nanotubes, International Journal of Nanomedicine 2 (2007) 707–714.

[91] M. S. Dresselhaus, Applied physics: nanotube antennas, Nature 432 (2004) 959–60. doi:10.1038/432959a.

[92] R. Saito, A. Grüneis, G. G. Samsonidze, G. Dresselhaus, M. S. Dresselhaus, A. Jorio, L. G. Cançado, M. A. Pimenta, A. G. Souza Filho, Optical absorption of graphite and single-wall carbon nanotubes, Applied Physics A 78 (2004) 1099–1105. doi:10.1007/s00339-003-2459-z.

[93] D. Boldor, N. M. Gerbo, W. T. Monroe, J. H. Palmer, Z. R. Li, A. S. Biris, Temperature measurement of carbon nanotubes using infrared thermography, Chemistry of Materials 20 (2008) 4011–4016. doi:10.1021/cm800428e.

[94] S. Ghosh, S. Dutta, E. Gomes, D. Carroll, J. D'Agostino, R., J. Olson, M. Guthold, W. H. Gmeiner, Increased heating efficiency and selective thermal ablation of malignant tissue with dna-encased multiwalled carbon nanotubes, ACS Nano 3 (2009) 2667–73. doi:10.1021/nn900368b.

[95] N. W. S. Kam, M. O'Connell, J. A. Wisdom, H. J. Dai, Carbon nanotubes as multifunctional biological transporters and near-infrared agents for selective cancer cell destruction, Proceedings of the National Academy of Sciences of the United States of America 102 (2005) 11600–11605. doi:10.1073/pnas.0502680102.

[96] H. K. Moon, S. H. Lee, H. C. Choi, In vivo near-infrared mediated tumor destruction by photothermal effect of carbon nanotubes, ACS Nano 3 (2009) 3707–13. doi:10.1021/nn900904h.

[97] J. T. Robinson, K. Welsher, S. M. Tabakman, S. P. Sherlock, H. Wang, R. Luong, H. Dai, High performance in vivo near-ir (>1 mum) imaging and photothermal cancer therapy with carbon nanotubes, Nano Res 3 (2010) 779–793. doi:10.1007/s12274-010-0045-1.

[98] J. W. Kim, E. V. Shashkov, E. I. Galanzha, N. Kotagiri, V. P. Zharov, Photothermal antimicrobial nanotherapy and nanodiagnostics with self-assembling carbon nanotube clusters, Lasers Surg Med 39 (2007) 622–34. doi:10.1002/lsm.20534.

[99] A. S. Biris, D. Boldor, J. Palmer, W. T. Monroe, M. Mahmood, E. Dervishi, Y. Xu, Z. Li, E. I. Galanzha, V. P. Zharov, Nanophotothermolysis of multiple scattered cancer cells with carbon nanotubes guided by time-resolved infrared thermal imaging, J Biomed Opt 14 (2009) 021007. doi:10.1117/1.3119135.

[100] L. Picou, C. McMann, P. H. Elzer, F. M. Enright, A. S. Biris, D. Boldor, Spatio-temporal thermal kinetics of in situ mwcnt heating in biological tissues under nir laser irradiation, Nanotechnology 21 (2010) 435101. doi:10.1088/0957-4484/21/43/435101.

[101] C. H. Wang, Y. J. Huang, C. W. Chang, W. M. Hsu, C. A. Peng, In vitro photothermal destruction of neuroblastoma cells using carbon nanotubes conjugated with gd2 monoclonal antibody, Nanotechnology 20 (2009) 315101. doi:10.1088/0957-4484/20/31/315101.

[102] A. R. Burke, R. N. Singh, D. L. Carroll, J. C. Wood, J. D'Agostino, R. B., P. M. Ajayan, F. M. Torti, S. V. Torti, The resistance of breast cancer stem cells to conventional hyperthermia and their sensitivity to nanoparticle-mediated photothermal therapy, Biomaterials 33 (2012) 2961–70. doi:10.1016/j.biomaterials.2011.12.052.

[103] Z. Lin, Y. Liu, X. Ma, S. Hu, J. Zhang, Q. Wu, W. Ye, S. Zhu, D. Yang, D. Qu, J. Jiang, Photothermal ablation of bone metastasis of breast cancer using pegylated multi-walled carbon nanotubes, Sci Rep 5 (2015) 11709. doi:10.1038/srep11709.

[104] J. Xu, M. Xiao, R. Czerw, D. L. Carroll, Optical limiting and enhanced optical nonlinearity in boron-doped carbon nanotubes, Chemical Physics Letters 389 (2004) 247–250. doi:10.1016/j.cplett.2004.03.111.

[105] Z. Liu, W. Cai, L. He, N. Nakayama, K. Chen, X. Sun, X. Chen, H. Dai, In vivo biodistribution and highly efficient tumour targeting of carbon nanotubes in mice, Nat Nanotechnol 2 (2007) 47–52. doi:10.1038/nnano.2006.170.

[106] R. Singh, D. Pantarotto, L. Lacerda, G. Pastorin, C. Klumpp, M. Prato, A. Bianco, Kostarelos, Kostas, Tissue biodistribution and blood clearance rates of intravenously administered carbon nanotube radiotracers, PNAS 103 (2006) 3357–3362.

[107] L. Lacerda, H. Ali-Boucetta, M. A. Herrero, G. Pastorin, A. Bianco, M. Prato, K. Kostarelos, Tissue histology and physiology following intravenous administration of different types of functionalized multiwalled carbon nanotubes, Nanomedicine (Lond) 3 (2008) 149–61. doi:10.2217/17435889.3.2.149.

[108] L. Lacerda, M. A. Herrero, K. Venner, A. Bianco, M. Prato, K. Kostarelos, Carbon-nanotube shape and individualization critical for renal excretion, Small 4 (2008) 1130–2. doi:10.1002/smll.200800323.

[109] V. P. Torchilin, Multifunctional nanocarriers, Adv Drug Deliv Rev 58 (2006) 1532–55. doi:10.1016/j.addr.2006.09.009.

[110] D. Mohanta, S. Patnaik, S. Sood, N. Das, Carbon nanotubes: Evaluation of toxicity at biointerfaces, J Pharm Anal 9 (2019) 293–300. doi:10.1016/j.jpha.2019.04.003.

[111] X. Huang, M. A. El-Sayed, Gold nanoparticles: Optical properties and implementations in cancer diagnosis and photothermal therapy, Journal of Advanced Research 1 (2010) 13–28. doi:10.1016/j.jare.2010.02.002.

[112] P. K. Jain, X. Huang, I. H. El-Sayed, M. A. El-Sayed, Review of some interesting surface plasmon resonance-enhanced properties of noble metal nanoparticles and their applications to biosystems, Plasmonics 2 (2007) 107–118. doi:10.1007/s11468-007-9031-1.

[113] D. Boyer, P. Tamarat, A. Maali, B. Lounis, M. Orrit, Photothermal imaging of nanometer-sized metal particles among scatterers, Science 297 (2002) 1160–3. doi:10.1126/science.1073765.

[114] J. Kadkhoda, A. Aghanejad, B. Safari, J. Barar, S. H. Rasta, S. Davaran, Aptamer-conjugated gold nanoparticles for targeted paclitaxel delivery and photothermal therapy in breast cancer, Journal of Drug Delivery Science and Technology 67 (2022). doi:10.1016/j.jddst.2021.102954.

[115] B. Albertini, V. Mathieu, N. Iraci, M. Van Woensel, A. Schoubben, A. Donnadio, S. M. L. Greco, M. Ricci, A. Temperini, P. Blasi, N. Wauthoz, Tumor targeting by peptide-decorated gold nanoparticles, Mol Pharm 16 (2019) 2430–2444. doi:10.1021/acs.molpharmaceut.9b00047.

[116] K. Hori, S. Higashida, T. Osaki, T. Kawano, H. Inaba, K. Matsuura, T. Iwasaki, Intracellular delivery and photothermal therapeutic effects of polyhistidine peptide-modified gold nanoparticles, J Biotechnol 354 (2022) 34–44. doi:10.1016/j.jbiotec.2022.06.006.

[117] P. K. Jain, M. A. El-Sayed, Plasmonic coupling in noble metal nanostructures, Chemical Physics Letters 487 (2010) 153–164. doi:10.1016/j.cplett.2010.01.062.

[118] P. K. Jain, K. S. Lee, I. H. El-Sayed, M. A. El-Sayed, Calculated absorption and scattering properties of gold nanoparticles of different size, shape, and composition: applications in biological imaging and biomedicine, J Phys Chem B 110 (2006) 7238–48. doi:10.1021/jp057170o.

[119] S. W. Prescott, P. Mulvaney, Gold nanorod extinction spectra, Journal of Applied Physics 99 (2006). doi:10.1063/1.2203212.

[120] R. D. Averitt, D. Sarkar, N. J. Halas, Plasmon resonance shifts of au-coatedau2snanoshells: Insight into multicomponent nanoparticle growth, Physical Review Letters 78 (1997) 4217–4220. doi:10.1103/PhysRevLett.78.4217.

[121] S. J. Oldenburg, R. D. Averitt, S. L. Westcott, N. J. Halas, Nanoengineering of optical resonances, Chemical Physics Letters 288 (1998) 243–247. doi:10.1016/s0009-2614(98)00277-2.

[122] R. Bardhan, S. Lal, A. Joshi, N. J. Halas, Theranostic nanoshells: From probe design to imaging and treatment of cancer, Accounts of Chemical Research 44 (2011) 936–946. doi:10.1021/ar200023x.

[123] E. Prodan, C. Radloff, N. J. Halas, P. Nordlander, A hybridization model for the plasmon response of complex nanostructures, Science 302 (2003) 419–22. doi:10.1126/science.1089171.

[124] K. Liu, X. Xue, E. P. Furlani, Theoretical comparison of optical properties of near-infrared colloidal plasmonic nanoparticles, Sci Rep 6 (2016) 34189. doi:10.1038/srep34189.

[125] L. Au, D. Zheng, F. Zhou, Z. Y. Li, X. Li, Y. Xia, A quantitative study on the photothermal effect of immuno gold nanocages targeted to breast cancer cells, ACS Nano 2 (2008) 1645–52. doi:10.1021/nn800370j.

[126] Y. Sun, Y. Xia, Mechanistic study on the replacement reaction between silver nanostructures and chloroauric acid in aqueous medium, J Am Chem Soc 126 (2004) 3892–901. doi:10.1021/ja039734c.

[127] X. Kang, X. Guo, X. Niu, W. An, S. Li, Z. Liu, Y. Yang, N. Wang, Q. Jiang, C. Yan, H. Wang, Q. Zhang, Photothermal therapeutic application of gold nanorods-porphyrin-trastuzumab complexes in her2-positive breast cancer, Sci Rep 7 (2017) 42069. doi:10.1038/srep42069.

[128] A. N. Kharlamov, A. E. Tyurnina, V. S. Veselova, O. P. Kovtun, V. Y. Shur, J. L. Gabinsky, Silica-gold nanoparticles for atheroprotective management of plaques: results of the nanom-fim trial, Nanoscale 7 (2015) 8003–15. doi:10.1039/c5nr01050k.

[129] D. Gentili, G. Ori, M. Comes Franchini, Double phase transfer of gold nanorods for surface functionalization and entrapment into peg-based nanocarriers, Chem Commun (Camb) (2009) 5874–6. doi:10.1039/b911582j.

[130] A. P. Leonov, J. Zheng, J. D. Clogston, S. T. Stern, A. K. Patri, A. Wei, Detoxification of gold nanorods by treatment with polystyrenesulfonate, ACS Nano 2 (2008) 2481–8. doi:10.1021/nn800466c.

[131] D. Harris-Birtill, M. Singh, Y. Zhou, A. Shah, P. Ruenraroengsak, M. E. Gallina, G. B. Hanna, A. E. G. Cass, A. E. Porter, J. Bamber, D. S. Elson, Gold nanorod reshaping in vitro and in vivo using a continuous wave laser, PLoS One 12 (2017) e0185990. doi:10.1371/journal.pone.0185990.

[132] H. Petrova, J. Perez Juste, I. Pastoriza-Santos, G. V. Hartland, L. M. Liz-Marzan, P. Mulvaney, On the temperature stability of gold nanorods: comparison between thermal and ultrafast laser-induced heating, Phys Chem Chem Phys 8 (2006) 814–21. doi:10.1039/b514644e.

[133] W. da Silva, M. E. Ghica, C. M. A. Brett, Gold nanoparticle decorated multiwalled carbon nanotube modified electrodes for the electrochemical determination of theophylline, Analytical Methods 10 (2018) 5634–5642. doi:10.1039/c8ay02150c.

[134] P. Dawson, J. A. Duenas, M. G. Boyle, M. D. Doherty, S. E. Bell, A. M. Kern, O. J. Martin, A. S. Teh, K. B. Teo, W. I. Milne, Combined antenna and localized plasmon resonance in raman scattering from random arrays of silver-coated, vertically aligned multiwalled carbon nanotubes, Nano Lett 11 (2011) 365–71. doi:10.1021/nl102838w.

[135] J. Zhang, X. Zhang, S. Chen, T. Gong, Y. Zhu, Surface-enhanced raman scattering properties of multi-walled carbon nanotubes arrays-ag nanoparticles, Carbon 100 (2016) 395–407. doi:10.1016/j.carbon.2016.01.025.

[136] N. M. Briggs, L. Barrett, E. C. Wegener, L. V. Herrera, L. A. Gomez, J. T. Miller, S. P. Crossley, Identification of active sites on supported metal catalysts with carbon nanotube hydrogen highways, Nat Commun 9 (2018) 3827. doi:10.1038/s41467-018-06100-9.

[137] V. Duc Chinh, G. Speranza, C. Migliaresi, N. Van Chuc, V. Minh Tan, N. T. Phuong, Synthesis of gold nanoparticles decorated with multiwalled carbon nanotubes (au-mwcnts) via cysteaminium chloride functionalization, Sci Rep 9 (2019) 5667. doi:10.1038/s41598-019-42055-7.

[138] G. M. Neelgund, A. Oki, Photothermal effect of ag nanoparticles deposited over poly(amidoamine) grafted carbon nanotubes, J Photochem Photobiol A Chem 364 (2018) 309–315. doi:10.1016/j.jphotochem.2018.06.007.

[139] D. Sun, J. McLaughlan, L. Zhang, B. G. Falzon, D. Mariotti, P. Maguire, D. Sun, Atmospheric pressure plasma-synthesized gold nanoparticle/carbon nanotube hybrids for photothermal conversion, Langmuir 35 (2019) 4577–4588. doi:10.1021/acs.langmuir.8b03945.

[140] X. Wang, C. Wang, L. Cheng, S. T. Lee, Z. Liu, Noble metal coated single-walled carbon nanotubes for applications in surface enhanced raman scattering imaging and photothermal therapy, J Am Chem Soc 134 (2012) 7414–22. doi:10.1021/ja300140c.

[141] Y. Zhu, Q. Sun, Y. Liu, T. Ma, L. Su, S. Liu, X. Shi, D. Han, F. Liang, Decorating gold nanostars with multiwalled carbon nanotubes for photothermal therapy, R Soc Open Sci 5 (2018) 180159. doi:10.1098/rsos.180159.

[142] S. A. Khan, R. Kanchanapally, Z. Fan, L. Beqa, A. K. Singh, D. Senapati, P. C. Ray, A gold nanocage-cnt hybrid for targeted imaging and photothermal destruction of cancer cells, Chem Commun (Camb) 48 (2012) 6711–3. doi:10.1039/c2cc32313c.

[143] T. J. Echtermeyer, L. Britnell, P. K. Jasnos, A. Lombardo, R. V. Gorbachev, A. N. Grigorenko, A. K. Geim, A. C. Ferrari, K. S. Novoselov, Strong plasmonic enhancement of photovoltage in graphene, Nat Commun 2 (2011) 458. doi:10.1038/ncomms1464.

[144] A. M. Gilbertson, Y. Francescato, T. Roschuk, V. Shautsova, Y. Chen, T. P. Sidiropoulos, M. Hong, V. Giannini, S. A. Maier, L. F. Cohen, R. F. Oulton, Plasmon-induced optical anisotropy in hybrid graphene-metal nanoparticle systems, Nano Lett 15 (2015) 3458–64. doi:10.1021/acs.nanolett.5b00789.

[145] Y. Liu, R. Cheng, L. Liao, H. Zhou, J. Bai, G. Liu, L. Liu, Y. Huang, X. Duan, Plasmon resonance enhanced multicolour photodetection by graphene, Nat Commun 2 (2011) 579. doi:10.1038/ncomms1589.

[146] D. K. Lim, A. Barhoumi, R. G. Wylie, G. Reznor, R. S. Langer, D. S. Kohane, Enhanced photothermal effect of plasmonic nanoparticles coated with reduced graphene oxide, Nano Lett 13 (2013) 4075–9. doi:10.1021/nl4014315.

[147] M. Derakhshi, A. A. Ashkarran, A. Bahari, S. Bonakdar, Synergistic effect of shape-selective silver nanostructures decorating reduced graphene oxide nanoplatelets for enhanced cytotoxicity against breast cancer, Nanotechnology 29 (2018) 285102. doi:10.1088/1361-6528/aac011.

[148] J. Song, F. Wang, X. Yang, B. Ning, M. G. Harp, S. H. Culp, S. Hu, P. Huang, L. Nie, J. Chen, X. Chen, Gold nanoparticle coated carbon nanotube ring with enhanced raman scattering and photothermal conversion property for theranostic applications, J Am Chem Soc 138 (2016) 7005–15. doi:10.1021/jacs.5b13475.

[149] Y. Y. Ou, M. H. Huang, High-density assembly of gold nanoparticles on multiwalled carbon nanotubes using 1-pyrenemethylamine as interlinker, Journal of Physical Chemistry B 110 (2006) 2031–2036. doi:10.1021/jp055920o.

[150] V. Georgakilas, D. Gournis, V. Tzitzios, L. Pasquato, D. M. Guldi, M. Prato, Decorating carbon nanotubes with metal or semiconductor nanoparticles, Journal of Materials Chemistry 17 (2007). doi:10.1039/b700857k.

[151] B. I. Kharisov, O. V. Kharissova, U. Ortiz Méndez, I. G. De La Fuente, Decoration of carbon nanotubes with metal nanoparticles: Recent trends, Synthesis and Reactivity in Inorganic, Metal-Organic, and Nano-Metal Chemistry 46 (2015) 55–76. doi:10.1080/15533174.2014.900635.

[152] Y. Li, N. Chopra, Gold nanoparticle integrated with nanostructured carbon and quantum dots: synthesis and optical properties, Gold Bulletin 48 (2015) 73–83. doi:10.1007/s13404-015-0163-3.

[153] J. Lu, Effect of surface modifications on the decoration of multi-walled carbon nanotubes with ruthenium nanoparticles, Carbon 45 (2007) 1599–1605. doi:10.1016/j.carbon.2007.04.013.

[154] J.-M. Yeh, K.-Y. Huang, S.-Y. Lin, Y.-Y. Wu, C.-C. Huang, S.-J. Liou, Noncovalent interaction between gold nanoparticles and multiwalled carbon nanotubes via an intermediatory, Journal of Nanotechnology 2009 (2009) 1–7. doi:10.1155/2009/217469.

[155] F. Oudjedi, S. S. Lee, M. Paliouras, M. Trifiro, A. G. Kirk, Enhancing in vitro photothermal therapy using plasmonic gold nanorod decorated multiwalled carbon nanotubes, Biomedical Optics Express 14 (2023). doi:10.1364/boe.504746.

[156] A. Bianco, K. Kostarelos, M. Prato, Opportunities and challenges of carbon-based nanomaterials for cancer therapy, Expert Opin Drug Deliv 5 (2008) 331–42. doi:10.1517/17425247.5.3.331.

[157] K. Kostarelos, A. Bianco, M. Prato, Promises, facts and challenges for carbon nanotubes in imaging and therapeutics, Nat Nanotechnol 4 (2009) 627–33. doi:10.1038/nnano.2009.241.

[158] S. S. Lee, F. Oudjedi, A. G. Kirk, M. Paliouras, M. A. Trifiro, Photothermal therapy of papillary thyroid cancer tumor xenografts with targeted thyroid stimulating hormone receptor antibody functionalized multiwalled carbon nanotubes, Cancer Nanotechnology 14 (2023). doi:10.1186/s12645-023-00184-9.

[159] L. Wang, J. Shi, Y. Hao, P. Zhang, Y. Zhao, D. Meng, D. Li, J. Chang, Z. Zhang, Magnetic multi-walled carbon nanotubes for tumor theranostics, J Biomed Nanotechnol 11 (2015) 1653–61. doi:10.1166/jbn.2015.2103.

[160] S. Wang, Q. Lin, J. Chen, H. Gao, D. Fu, S. Shen, Biocompatible polydopamine-encapsulated gadolinium-loaded carbon nanotubes for mri and color mapping guided photothermal dissection of tumor metastasis, Carbon 112 (2017) 53–62. doi:10.1016/j.carbon.2016.10.096.

[161] S. P. Sherlock, S. M. Tabakman, L. Xie, H. Dai, Photothermally enhanced drug delivery by ultrasmall multifunctional feco/graphitic shell nanocrystals, ACS Nano 5 (2011) 1505–12. doi:10.1021/nn103415x.

[162] Z. Abed, J. Beik, S. Laurent, N. Eslahi, T. Khani, E. S. Davani, H. Ghaznavi, A. Shakeri-Zadeh, Iron oxide-gold core-shell nano-theranostic for magnetically targeted photothermal therapy under magnetic resonance imaging guidance, J Cancer Res Clin Oncol 145 (2019) 1213–1219. doi:10.1007/s00432-019-02870-x.

[163] J. Liu, H. Cui, S. Yan, X. Jing, D. Wang, L. Meng, Gold nanostars decorated mno2 nanosheets for magnetic resonance imaging and photothermal erasion of lung cancer cell, Materials Today Communications 16 (2018) 97–104. doi:10.1016/j.mtcomm.2018.04.012.

[164] T. He, C. Jiang, J. He, Y. Zhang, G. He, J. Wu, J. Lin, X. Zhou, P. Huang, Manganese-dioxide-coating-instructed plasmonic modulation of gold nanorods for activatable duplex-imaging-guided nir-ii photothermal-chemodynamic therapy, Adv Mater 33 (2021) e2008540. doi:10.1002/adma.202008540.

[165] J. W. Kim, E. I. Galanzha, E. V. Shashkov, H. M. Moon, V. P. Zharov, Golden carbon nanotubes as multimodal photoacoustic and photothermal high-contrast molecular agents, Nat Nanotechnol 4 (2009) 688–94. doi:10.1038/nnano.2009.231.

[166] R. Kawasaki, K. Kondo, R. Miura, K. Yamana, H. Isozaki, R. Shimada, S. Kawamura, H. Hirano, T. Nishimura, N. Tarutani, K. Katagiri, A. Stubelius, S. I. Sawada, Y. Sasaki, K. Akiyoshi, A. Ikeda, Theranostic agent combining fullerene nanocrystals and gold nanoparticles for photoacoustic imaging and photothermal therapy, Int J Mol Sci 23 (2022). doi:10.3390/ijms23094686.

[167] Z. Wang, X. Sun, T. Huang, J. Song, Y. Wang, A sandwich nanostructure of gold nanoparticle coated reduced graphene oxide for photoacoustic imaging-guided photothermal therapy in the second nir window, Front Bioeng Biotechnol 8 (2020) 655. doi:10.3389/fbioe.2020.00655.

[168] L. An, Y. Wang, J. Lin, Q. Tian, Y. Xie, J. Hu, S. Yang, Macrophages-mediated delivery of small gold nanorods for tumor hypoxia photoacoustic imaging and enhanced photothermal therapy, ACS Appl Mater Interfaces 11 (2019) 15251–15261. doi:10.1021/acsami.9b00495.

[169] M. Zhou, B. Singhana, Y. Liu, Q. Huang, T. Mitcham, M. J. Wallace, R. J. Stafford, R. R. Bouchard, M. P. Melancon, Photoacoustic- and magnetic resonance-guided photothermal therapy and tumor vasculature visualization using theranostic magnetic gold nanoshells, J Biomed Nanotechnol 11 (2015) 1442–50. doi:10.1166/jbn.2015.2089.

[170] M. Zhang, W. Wang, F. Wu, P. Yuan, C. Chi, N. Zhou, Magnetic and fluorescent carbon nanotubes for dual modal imaging and photothermal and chemo-therapy of cancer cells in living mice, Carbon 123 (2017) 70–83. doi:10.1016/j.carbon.2017.07.032.

[171] A. Zhang, S. Pan, Y. Zhang, J. Chang, J. Cheng, Z. Huang, T. Li, C. Zhang, J. M. de la Fuentea, Q. Zhang, D. Cui, Carbon-gold hybrid nanoprobes for real-time imaging, photothermal/photodynamic and nanozyme oxidative therapy, Theranostics 9 (2019) 3443–3458. doi:10.7150/thno.33266.

[172] H. Zhang, Y. Wang, H. Zhong, J. Li, C. Ding, Near-infrared light-activated pt@au nanorings-based probe for fluorescence imaging and targeted photothermal therapy of cancer cells, ACS Appl Bio Mater 2 (2019) 5012–5020. doi:10.1021/acsabm.9b00712.

[173] O. O. Peltek, E. I. Ageev, P. M. Talianov, A. D. Mikushina, O. S. Epifanovskaya, A. Dubavik, V. P. Veiko, K. Lepik, D. A. Zuev, A. S. Timin, M. V. Zyuzin, Fluorescence-based thermometry for precise estimation of nanoparticle laser-induced heating in cancerous cells at nanoscale, Nanophotonics 11 (2022) 4323–4335. doi:10.1515/nanoph-2022-0314.

[174] E. N. Gerasimova, V. V. Yaroshenko, P. M. Talianov, O. O. Peltek, M. A. Baranov, P. V. Kapitanova, D. A. Zuev, A. S. Timin, M. V. Zyuzin, Real-time temperature monitoring of photoinduced cargo release inside living cells using hybrid capsules decorated with gold nanoparticles and fluorescent nanodiamonds, ACS Appl Mater Interfaces 13 (2021) 36737–36746. doi:10.1021/acsami.1c05252.

[175] H. D. Li, K. T. Yue, Z. L. Lian, Y. Zhan, L. X. Zhou, S. L. Zhang, Z. J. Shi, Z. N. Gu, B. B. Liu, R. S. Yang, H. B. Yang, G. T. Zou, Y. Zhang, S. Iijima, Temperature

dependence of the raman spectra of single-wall carbon nanotubes, Applied Physics Letters 76 (2000) 2053–2055. doi:10.1063/1.126252.

[176] M. Liu, K. L. Jiang, Q. Q. Li, H. T. Yang, S. S. Fan, Laser-induced high local temperature in carbon nanotube, Solid State Phenomena 121-123 (2007) 331–336. doi:10.4028/www.scientific.net/SSP.121-123.331.

[177] Raman Scattering in Materials Science, Springer Series in Materials Science, 2000. doi:10.1007/978-3-662-04221-2.

[178] R. McCreery, Raman Spectroscopy for Chemical Analysis, Wiley, 2005. URL: https://books.google.ca/books?id=qY4MI0Zln1YC.

[179] G. Baffou, Anti-stokes thermometry in nanoplasmonics, ACS Nano 15 (2021) 5785–5792. doi:10.1021/acsnano.1c01112.

[180] B. Gardner, P. Matousek, N. Stone, Direct monitoring of light mediated hyperthermia induced within mammalian tissues using surface enhanced spatially offset raman spectroscopy (t-sesors), Analyst 144 (2019) 3552–3555. doi:10.1039/c8an02466a.

[181] S. Hu, B. J. Liu, J. M. Feng, C. Zong, K. Q. Lin, X. Wang, D. Y. Wu, B. Ren, Quantifying surface temperature of thermoplasmonic nanostructures, J Am Chem Soc 140 (2018) 13680–13686. doi:10.1021/jacs.8b06083.

[182] D. N. Ngo, V. Ho, G. Kim, M. S. Song, M. R. Kim, J. Choo, S. W. Joo, S. Y. Lee, Raman thermometry nanopipettes in cancer photothermal therapy, Anal Chem 94 (2022) 6463–6472. doi:10.1021/acs.analchem.1c04452.

[183] M. Barella, I. L. Violi, J. Gargiulo, L. P. Martinez, F. Goschin, V. Guglielmotti, D. Pallarola, S. Schlucker, M. Pilo-Pais, G. P. Acuna, S. A. Maier, E. Cortes, F. D. Stefani, In situ photothermal response of single gold nanoparticles through hyperspectral imaging anti-stokes thermometry, ACS Nano 15 (2021) 2458–2467. doi:10.1021/acsnano.0c06185.

[184] S. Park, G. J. Yeon, H. Lee, H.-H. Shin, Z. H. Kim, Self-referenced sers thermometry of molecules on a metallic nanostructure, The Journal of Physical Chemistry C 126 (2021) 451–458. doi:10.1021/acs.jpcc.1c09717.

[185] C. D. Tschannen, M. Frimmer, T. L. Vasconcelos, L. Shi, T. Pichler, L. Novotny, Tip-enhanced stokes-anti-stokes scattering from carbyne, Nano Lett 22 (2022) 3260–3265. doi:10.1021/acs.nanolett.2c00154.

[186] E. Boulais, R. Lachaine, A. Hatef, M. Meunier, Plasmonics for pulsed-laser cell nanosurgery: Fundamentals and applications, Journal of Photochemistry and Photobiology C: Photochemistry Reviews 17 (2013) 26–49. doi:10.1016/j.jphotochemrev.2013.06.001.

[187] T. Katayama, K. Setoura, D. Werner, H. Miyasaka, S. Hashimoto, Picosecond-to-nanosecond dynamics of plasmonic nanobubbles from pump-probe spectral measurements of aqueous colloidal gold nanoparticles, Langmuir 30 (2014) 9504–13. doi:10.1021/la500663x.

[188] V. K. Pustovalov, A. S. Smetannikov, V. P. Zharov, Photothermal and accompanied phenomena of selective nanophotothermolysis with gold nanoparticles and laser pulses, Laser Physics Letters 5 (2008) 775–792. doi:10.1002/lapl.200810072.

[189] O. Ekici, R. K. Harrison, N. J. Durr, D. S. Eversole, M. Lee, A. Ben-Yakar, Thermal analysis of gold nanorods heated with femtosecond laser pulses, J Phys D Appl Phys 41 (2008) 185501. doi:10.1088/0022-3727/41/18/185501.

[190] A. Hatef, B. Darvish, A. Burke, A. Dagallier, M. Meunier, Computational characterization of plasma effects in ultrafast laser irradiation of spherical gold nanostructures for photothermal therapy, Journal of Physics D: Applied Physics 49 (2016). doi:10.1088/0022-3727/49/10/105401.

[191] S. Sánchez, O. Bautista, F. Méndez, Theoretical analysis of coupled thermal and denaturation processes in living tissues subject to a uniform surface heating condition, International Journal of Heat and Mass Transfer 90 (2015) 728–742. doi:10.1016/j.ijheatmasstransfer.2015.07.031.

[192] A. Sazgarnia, N. Naghavi, H. Mehdizadeh, Z. Shahamat, Investigation of thermal distribution for pulsed laser radiation in cancer treatment with nanoparticle-mediated hyperthermia, J Therm Biol 47 (2015) 32–41. doi:10.1016/j.jtherbio.2014.10.011.

[193] A. Hatef, S. Fortin-Deschênes, E. Boulais, F. Lesage, M. Meunier, Photothermal response of hollow gold nanoshell to laser irradiation: Continuous wave, short and ultrashort pulse, International Journal of Heat and Mass Transfer 89 (2015) 866–871. doi:10.1016/j.ijheatmasstransfer.2015.05.071.

[194] G. von Maltzahn, J. H. Park, A. Agrawal, N. K. Bandaru, S. K. Das, M. J. Sailor, S. N. Bhatia, Computationally guided photothermal tumor therapy using long-circulating gold nanorod antennas, Cancer Res 69 (2009) 3892–900. doi:10.1158/0008-5472.CAN-08-4242.

[195] A. Paul, N. Bandaru, A. Narasimhan, S. Das, Subsurface tumor ablation with near-infrared radiation using intratumoral and intravenous injection of nanoparticles, International Journal of Micro-Nano Scale Transport 5 (2014) 69–80. doi:10.1260/1759-3093.5.2.69.

[196] L. A. Dombrovsky, V. Timchenko, M. Jackson, G. H. Yeoh, A combined transient thermal model for laser hyperthermia of tumors with embedded gold nanoshells, International Journal of Heat and Mass Transfer 54 (2011) 5459–5469. doi:10.1016/j.ijheatmasstransfer.2011.07.045.

[197] S. Soni, H. Tyagi, R. A. Taylor, A. Kumar, Experimental and numerical investigation of heat confinement during nanoparticle-assisted thermal therapy, International Communications in Heat and Mass Transfer 69 (2015) 11–17. doi:10.1016/j.icheatmasstransfer.2015.10.001.

[198] S. S. H. T. A. Kumar, Light interaction of a nanoparticle embedded tissue towards a novel hyperthermia treatment, AIP Conference Proceedings 1391, ((2011)) 724–727. doi:https://doi.org/10.1063/1.3643661.

[199] J. Beik, M. Asadi, M. Mirrahimi, Z. Abed, A. Farashahi, R. Hashemian, H. Ghaznavi, A. Shakeri-Zadeh, An image-based computational modeling approach for prediction of

temperature distribution during photothermal therapy, Applied Physics B 125 (2019). doi:10.1007/s00340-019-7316-7.

[200] L. Wang, S. L. Jacques, L. Zheng, Mcml–monte carlo modeling of light transport in multi-layered tissues, Comput Methods Programs Biomed 47 (1995) 131–46. doi:10.1016/0169-2607(95)01640-f.

[201] D. Wang, W. Rao, Numerical simulation on thermal response of laser-irradiated biological tissues embedded with liquid metal nanoparticles, Journal of Thermal Science 31 (2022) 1220–1235. doi:10.1007/s11630-022-1623-8.

[202] Y. Xu, S. Long, Y. Yang, F. Zhou, N. Dong, K. Yan, B. Wang, Y. Zeng, N. Du, X. Li, W. R. Chen, Mathematical simulation of temperature distribution in tumor tissue and surrounding healthy tissue treated by laser combined with indocyanine green, Theor Biol Med Model 16 (2019) 12. doi:10.1186/s12976-019-0107-3.

[203] Y. Ren, H. Qi, Q. Chen, L. Ruan, Thermal dosage investigation for optimal temperature distribution in gold nanoparticle enhanced photothermal therapy, International Journal of Heat and Mass Transfer 106 (2017) 212–221. doi:10.1016/j.ijheatmasstransfer.2016.10.067.

[204] N. Manuchehrabadi, Y. Chen, A. Lebrun, R. Ma, L. Zhu, Computational simulation of temperature elevations in tumors using monte carlo method and comparison to experimental measurements in laser photothermal therapy, J Biomech Eng 135 (2013) 121007. doi:10.1115/1.4025388.

[205] A. De la Zerda, C. Zavaleta, S. Keren, S. Vaithilingam, S. Bodapati, Z. Liu, J. Levi, B. R. Smith, T. J. Ma, O. Oralkan, Z. Cheng, X. Chen, H. Dai, B. T. Khuri-Yakub, S. S. Gambhir, Carbon nanotubes as photoacoustic molecular imaging agents in living mice, Nat Nanotechnol 3 (2008) 557–62. doi:10.1038/nnano.2008.231.

[206] A. J. Caires, R. P. Vaz, C. Fantini, L. O. Ladeira, Highly sensitive and simple sers substrate based on photochemically generated carbon nanotubes-gold nanorods hybrids, J Colloid Interface Sci 455 (2015) 78–82. doi:10.1016/j.jcis.2015.04.071.

[207] H. Sharma, D. C. Agarwal, A. K. Shukla, D. K. Avasthi, V. D. Vankar, Surface-enhanced raman scattering and fluorescence emission of gold nanoparticle-multiwalled carbon nanotube hybrids, Journal of Raman Spectroscopy 44 (2013) 12–20. doi:10.1002/jrs.4136.

[208] E. Lidorikis, A. C. Ferrari, Photonics with multiwall carbon nanotube arrays, ACS Nano 3 (2009) 1238–48. doi:10.1021/nn900123a.

[209] I. Dotan, P. J. Roche, M. Paliouras, E. J. Mitmaker, M. A. Trifiro, Engineering multi-walled carbon nanotube therapeutic bionanofluids to selectively target papillary thyroid cancer cells, PLoS One 11 (2016) e0149723. doi:10.1371/journal.pone.0149723.

[210] S. Link, M. B. Mohamed, M. A. El-Sayed, Simulation of the optical absorption spectra of gold nanorods as a function of their aspect ratio and the effect of the medium dielectric constant, The Journal of Physical Chemistry B 103 (1999) 3073–3077. doi:10.1021/jp990183f.

[211] A. Muhammad, N. A. Yusof, R. Hajian, J. Abdullah, Decoration of carbon nanotubes with gold nanoparticles by electroless deposition process using ethylenediamine as a cross linker, Journal of Materials Research 31 (2016) 2897–2905. doi:10.1557/jmr.2016.304.

[212] O. Moradi, M. S. Maleki, S. Tahmasebi, Comparison between kinetics studies of protein adsorption by single-walled carbon nanotube and gold nanoparticles surfaces, Fullerenes, Nanotubes and Carbon Nanostructures 21 (2013) 733–748. doi:10.1080/1536383x.2012.654536.

[213] J. Ozhikandathil, S. Badilescu, M. Packirisamy, Plasmonic gold decorated mwcnt nanocomposite for localized plasmon resonance sensing, Sci Rep 5 (2015) 13181. doi:10.1038/srep13181.

[214] X. Suo, B. N. Eldridge, H. Zhang, C. Mao, Y. Min, Y. Sun, R. Singh, X. Ming, P-glycoprotein-targeted photothermal therapy of drug-resistant cancer cells using antibody-conjugated carbon nanotubes, ACS Appl Mater Interfaces 10 (2018) 33464–33473. doi:10.1021/acsami.8b11974.

[215] B. Zhang, H. Wang, S. Shen, X. She, W. Shi, J. Chen, Q. Zhang, Y. Hu, Z. Pang, X. Jiang, Fibrin-targeting peptide creka-conjugated multi-walled carbon nanotubes for self-amplified photothermal therapy of tumor, Biomaterials 79 (2016) 46–55. doi:10.1016/j.biomaterials.2015.11.061.

[216] M. Pramanik, M. Swierczewska, D. Green, B. Sitharaman, L. V. Wang, Single-walled carbon nanotubes as a multimodal-thermoacoustic and photoacoustic-contrast agent, J Biomed Opt 14 (2009) 034018. doi:10.1117/1.3147407.

[217] X. Dong, Z. Sun, X. Wang, X. Leng, An innovative mwcnts/dox/tc nanosystem for chemo-photothermal combination therapy of cancer, Nanomedicine 13 (2017) 2271–2280. doi:10.1016/j.nano.2017.07.002.

[218] Y. Yan, R. Wang, Y. Hu, R. Sun, T. Song, X. Shi, S. Yin, Stacking of doxorubicin on folic acid-targeted multiwalled carbon nanotubes for in vivo chemotherapy of tumors, Drug Deliv 25 (2018) 1607–1616. doi:10.1080/10717544.2018.1501120.

[219] W. He, K. Ai, C. Jiang, Y. Li, X. Song, L. Lu, Plasmonic titanium nitride nanoparticles for in vivo photoacoustic tomography imaging and photothermal cancer therapy, Biomaterials 132 (2017) 37–47. doi:10.1016/j.biomaterials.2017.04.007.

[220] A. Lalisse, G. Tessier, J. Plain, G. Baffou, Quantifying the efficiency of plasmonic materials for near-field enhancement and photothermal conversion, The Journal of Physical Chemistry C 119 (2015) 25518–25528. doi:10.1021/acs.jpcc.5b09294.

[221] A. A. Popov, G. Tselikov, N. Dumas, C. Berard, K. Metwally, N. Jones, A. Al-Kattan, B. Larrat, D. Braguer, S. Mensah, A. Da Silva, M. A. Esteve, A. V. Kabashin, Laser- synthesized tin nanoparticles as promising plasmonic alternative for biomedical applications, Sci Rep 9 (2019) 1194. doi:10.1038/s41598-018-37519-1.

[222] C. Wang, C. Dai, Z. Hu, H. Li, L. Yu, H. Lin, J. Bai, Y. Chen, Photonic cancer nanomedicine using the near infrared-ii biowindow enabled by biocompatible titanium nitride nanoplatforms, Nanoscale Horiz 4 (2019) 415–425. doi:10.1039/c8nh00299a.

[223] C. D. Brites, P. P. Lima, N. J. Silva, A. Millan, V. S. Amaral, F. Palacio, L. D. Carlos, Thermometry at the nanoscale, Nanoscale 4 (2012) 4799–829. doi:10.1039/c2nr30663h.

[224] M. Suzuki, T. Plakhotnik, The challenge of intracellular temperature, Biophys Rev 12 (2020) 593–600. doi:10.1007/s12551-020-00683-8.

[225] S. Xu, A. Fan, H. Wang, X. Zhang, X. Wang, Raman-based nanoscale thermal transport characterization: A critical review, International Journal of Heat and Mass Transfer 154 (2020). doi:10.1016/j.ijheatmasstransfer.2020.119751.

[226] K. Nakanishi, A. Kogure, R. Kuwana, H. Takamatsu, K. Ito, Development of a novel scanning thermal microscopy (sthm) method to measure the thermal conductivity of biological cells, Biocontrol Sci 22 (2017) 175–180. doi:10.4265/bio.22.175.

[227] G. Baffou, P. Bon, J. Savatier, J. Polleux, M. Zhu, M. Merlin, H. Rigneault, S. Monneret, Thermal imaging of nanostructures by quantitative optical phase analysis, ACS Nano 6 (2012) 2452–8. doi:10.1021/nn2047586.

[228] H. Odeen, D. L. Parker, Magnetic resonance thermometry and its biological applications - physical principles and practical considerations, Prog Nucl Magn Reson Spectrosc 110 (2019) 34–61. doi:10.1016/j.pnmrs.2019.01.003.

[229] C. Bu, L. Mu, X. Cao, M. Chen, G. She, W. Shi, Silver nanowire-based fluorescence thermometer for a single cell, ACS Appl Mater Interfaces 10 (2018) 33416–33422. doi:https://doi.org/10.1021/acsami.8b09696.

[230] D. Chrétien, P. Bénit, C. Leroy, R. El-Khoury, S. Park, J. Y. Lee, Y.-T. Chang, G. Lenaers, P. Rustin, M. Rak, Pitfalls in monitoring mitochondrial temperature using charged thermosensitive fluorophores, Chemosensors 8 (2020). doi:10.3390/chemosensors8040124.

[231] K. Okabe, N. Inada, C. Gota, Y. Harada, T. Funatsu, S. Uchiyama, Intracellular temperature mapping with a fluorescent polymeric thermometer and fluorescence lifetime imaging microscopy, Nat Commun 3 (2012) 705. doi:10.1038/ncomms1714.

[232] T. Yamazaki, X. Liu, Y.-T. Chang, S. Arai, Applicability and limitations of fluorescence intensity-based thermometry using a palette of organelle thermometers, Chemosensors 11 (2023). doi:10.3390/chemosensors11070375.

[233] H. J. Butler, L. Ashton, B. Bird, G. Cinque, K. Curtis, J. Dorney, K. Esmonde-White, N. J. Fullwood, B. Gardner, P. L. Martin-Hirsch, M. J. Walsh, M. R. McAinsh, N. Stone, F. L. Martin, Using raman spectroscopy to characterize biological materials, Nat Protoc 11 (2016) 664–87. doi:10.1038/nprot.2016.036.

[234] C. C. Hsu, J. Xu, B. Brinkhof, H. Wang, Z. Cui, W. E. Huang, H. Ye, A single-cell raman-based platform to identify developmental stages of human pluripotent stem cell-derived neurons, Proc Natl Acad Sci U S A 117 (2020) 18412–18423. doi:10.1073/pnas.2001906117.

[235] R. L. McCreery, Raman Spectroscopy for Chemical Analysis, 2000. doi:10.1002/0471721646.

[236] G. W. Auner, S. K. Koya, C. Huang, B. Broadbent, M. Trexler, Z. Auner, A. Elias, K. C. Mehne, M. A. Brusatori, Applications of raman spectroscopy in cancer diagnosis, Cancer Metastasis Rev 37 (2018) 691–717. doi:10.1007/s10555-018-9770-9.

[237] S. Cui, S. Zhang, S. Yue, Raman spectroscopy and imaging for cancer diagnosis, J Healthc Eng 2018 (2018) 8619342. doi:10.1155/2018/8619342.

[238] C. A. Parra-Murillo, M. F. Santos, C. H. Monken, A. Jorio, Stokes–anti-stokes correlation in the inelastic scattering of light by matter and generalization of the bose-einstein population function, Physical Review B 93 (2016). doi:10.1103/PhysRevB.93.125141.

[239] S. D. McGrane, D. S. Moore, P. M. Goodwin, D. M. Dattelbaum, Quantitative tradeoffs between spatial, temporal, and thermometric resolution of nonresonant raman thermometry for dynamic experiments, Appl Spectrosc 68 (2014) 1279–88. doi:10.1366/14-07503.

[240] I. Calizo, A. A. Balandin, W. Bao, F. Miao, C. N. Lau, Temperature dependence of the raman spectra of graphene and graphene multilayers, Nano Lett 7 (2007) 2645–9. doi:10.1021/nl071033g.

[241] M. S. Dresselhaus, G. Dresselhaus, R. Saito, A. Jorio, Raman spectroscopy of carbon nanotubes, Physics Reports 409 (2005) 47–99. doi:10.1016/j.physrep.2004.10.006.

[242] C. Li, S. Xu, Y. Yue, B. Yang, X. Wang, Thermal characterization of carbon nanotube fiber by time-domain differential raman, Carbon 103 (2016) 101–108. doi:10.1016/j.carbon.2016.03.003.

[243] R. C. Maher, L. F. Cohen, J. C. Gallop, E. C. Le Ru, P. G. Etchegoin, Temperature-dependent anti-stokes/stokes ratios under surface-enhanced raman scattering conditions, J Phys Chem B 110 (2006) 6797–803. doi:10.1021/jp056466r.

[244] C. Boerigter, U. Aslam, S. Linic, Mechanism of charge transfer from plasmonic nanostructures to chemically attached materials, ACS Nano 10 (2016) 6108–15. doi:10.1021/acsnano.6b01846.

[245] C. D. Tschannen, M. Frimmer, G. Gordeev, T. L. Vasconcelos, L. Shi, T. Pichler, S. Reich, S. Heeg, L. Novotny, Anti-stokes raman scattering of single carbyne chains, ACS Nano (2021). doi:10.1021/acsnano.1c03893.

[246] V. Zani, D. Pedron, R. Pilot, R. Signorini, Contactless temperature sensing at the microscale based on titanium dioxide raman thermometry, Biosensors (Basel) 11 (2021). doi:10.3390/bios11040102.

[247] S. Jones, D. Andrén, P. Karpinski, M. Käll, Photothermal heating of plasmonic nanoantennas: Influence on trapped particle dynamics and colloid distribution, ACS Photonics 5 (2018) 2878–2887. doi:10.1021/acsphotonics.8b00231.

[248] Y. F. Kang, B. Zheng, C. Y. Li, Z. L. Zhang, H. W. Tang, Q. S. Wu, D. W. Pang, Real-time monitoring of temperature variations around a gold nanobipyramid targeted cancer cell under photothermal heating by actively manipulating an optically trapped

luminescent upconversion microparticle, Anal Chem 92 (2020) 1292–1300. doi:10.1021/acs.analchem.9b04470.

[249] M. A. Pleitez, A. A. Khan, A. Solda, A. Chmyrov, J. Reber, F. Gasparin, M. R. Seeger, B. Schatz, S. Herzig, M. Scheideler, V. Ntziachristos, Label-free metabolic imaging by mid-infrared optoacoustic microscopy in living cells, Nat Biotechnol 38 (2020) 293–296. doi:10.1038/s41587-019-0359-9.

[250] E. L. Keller, R. R. Frontiera, Ultrafast nanoscale raman thermometry proves heating is not a primary mechanism for plasmon-driven photocatalysis, ACS Nano 12 (2018) 5848–5855. doi:10.1021/acsnano.8b01809.

[251] A. Lombardi, M. K. Schmidt, L. Weller, W. M. Deacon, F. Benz, B. de Nijs, J. Aizpurua, J. J. Baumberg, Pulsed molecular optomechanics in plasmonic nanocavities: From nonlinear vibrational instabilities to bond-breaking, Physical Review X 8 (2018). doi:10.1103/PhysRevX.8.011016.

[252] T. Jollans, M. Caldarola, Y. Sivan, M. Orrit, Effective electron temperature measurement using time-resolved anti-stokes photoluminescence, J Phys Chem A 124 (2020) 6968–6976. doi:10.1021/acs.jpca.0c06671.

[253] P. B. Johnson, R. W. Christy, Optical constants of the noble metals, Physical Review B 6 (1972) 4370–4379. doi:10.1103/PhysRevB.6.4370.

[254] A. B. Djurišić, E. H. Li, Optical properties of graphite, Journal of Applied Physics 85 (1999) 7404–7410. doi:10.1063/1.369370.

[255] C. Wei, X. Jin, C. Wu, A. Brozovic, W. Zhang, Carbon spheres with high photothermal conversion efficiency for photothermal therapy of tumor, Diamond and Related Materials 126 (2022). doi:10.1016/j.diamond.2022.109048.